CENTRO DE INVESTIGACIÓN Y DE ESTUDIOS AVANZADOS DEL INSTITUTO POLITÉCNICO NACIONAL

UNIDAD ZACATENCO
DEPARTAMENTO DE INGENIERÍA ELÉCTRICA
SECCIÓN ELECTRÓNICA DEL ESTADO SÓLIDO

"Synthesis and characterization of chemical sensors based on ceramic pellets tin oxide nanoparticles activated by Cu, Pd and Pt"

Tesis que presenta:
VENKATA KRISHNA KARTHIK TANGIRALA

Para obtener el grado de:
Doctorado en Ciencias

En la especialidad de
Ingeniería Eléctrica

Directores de la Tesis
Dra. María de la Luz Olvera Amador
Dr. Arturo Maldonado Álvarez

México, Distrito Federal. Octubre, 2015

ACKNOWLEDGEMENTS

Firstly, I would like to thank sincerely, Consejo Nacional de Ciencia y Tecnología (CONACYT), for giving me scholarship for my entire PhD time.

I would like to express my special appreciation and thanks to my advisor Professor Dr. Maria de la Luz Olvera Amador, you have been a tremendous mentor for me. I would like to thank you for encouraging my research and for allowing me to grow as a research scientist. Your advice on both research as well as on my career have been invaluable. Also I would like to thank Dr. Arturo Maldonado Álvarez for his precious suggestions and motivating me to complete my PhD work successfully.

I would also like to thank my committee members, Dr. Mauricio Ortega López, Dr. Velumani Subramanian, Dr. Dwight Roberto Acosta Najarro and Dr. Ramón Peña Sierra for serving as my committee members even at hardship. I also want to thank you for letting my defense be an enjoyable moment, and for your brilliant comments and suggestions, thanks to you.

I would especially like to thank Miguel Angel Luna Arias for his help in getting familiarity with all the major equipment's I used in my PhD work. Also I would like to thank all other technicians and co-workers of my department for being patient with me in characterization of my samples.

A special thanks to my parents for their unconditional love. I would also like to thank to my beloved wife for her love, care, continual source of support and encouragement all the time.

T.V.K.KARTHIK

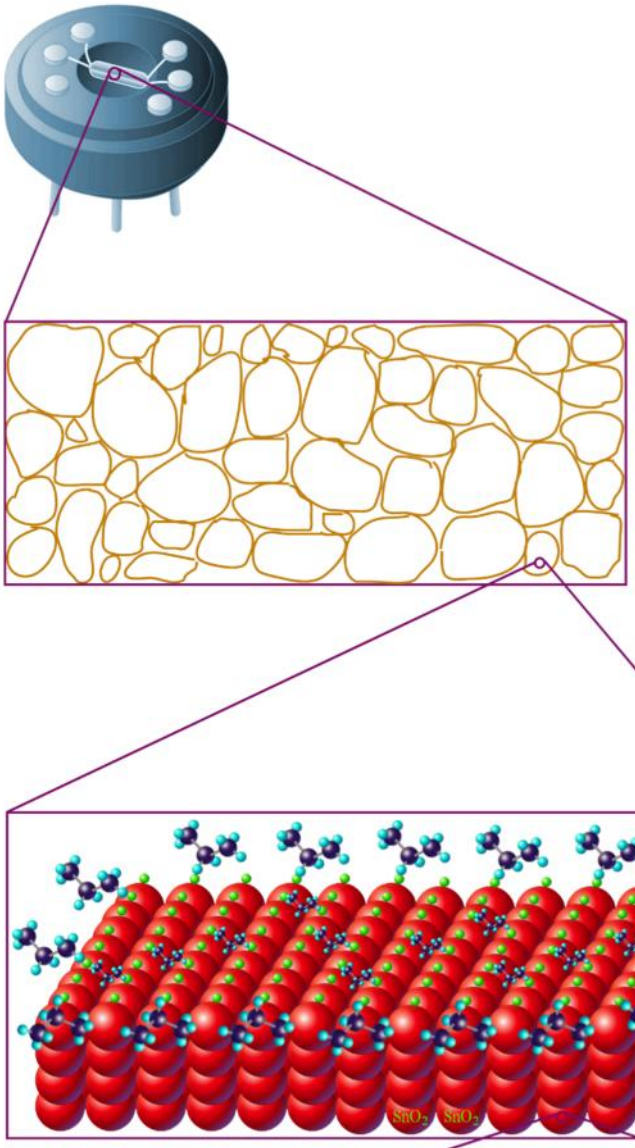

As
Sensor
go Nano

World
gets
Smarter

ABSTRACT

In our work, we have utilized a novel method by combining chemical and physical synthesis methods for obtaining tin oxide (SnO_2) nanoparticles. In this method, primarily we used chemical homogeneous precipitation to obtain SnO_2 particles with uniform particles size and then secondly we ball milled the powders to decrease the size of the particles and also the agglomeration. Compared to other methods, our synthesis route offers SnO_2 particles with very less agglomeration, and the particles size was around 20 -30nm range, with homogeneous size distribution of the particles. We have utilized urea (R1) and ammonia (R2) as two precipitation agents to synthesize the SnO_2 powders. The resultant SnO_2 powders were doped with transition metal, Cu, and noble metals like Pt and Pd via two doping methods D1 and D2. In D1, the powders were bulk doped and then ball milled, whereas in D2, the powders were ball milled and then surface doped.

All the undoped and doped powders obtained were later pressed using manual pressing machine to manufacture the SnO_2 pellets. Pellets with a thickness of 0.5 mm and diameter of 9mm were prepared; they were mechanically pressed for a time period of 90 min and with a pressure of 16 tons. The effect of synthesis routes, doping methods and dopants, on the structural, morphological and also on CO sensing were studied by different characterization techniques and analyzed with their detailed explanations.

Interestingly, the Cu-SnO_2 pellets manufactured from the powders obtained by method D1R1, showed highest sensitivity around 1782, when measured at 300 ^{0}C, compared to Pt and Pd doped pellets, which is very high compared to the literature, to the best of our knowledge. This high sensitivity is due to various reasons like uniform and small particle size, necks formation, inter-particle conductance and high oxygen adsorption due to stacking faults. All the reasons mentioned above were demonstrated by comparing the established sensor theory with our different experimental results.

Additionally, the ball milled powders were mixed with Al_2O_3 powders (particle size 1µm) to save the SnO_2 powders and also to increase the porosity of the pellet. Sensitivity didn't increase compared to previous (pellets after ball milled). Maximum sensitivity value obtained was around 48 and the tendency of increasing the sensitivity with respect to temperature and the gas concentration was achieved successfully.

Also, a viscous paste was made out of the SnO_2 powders and thick films were deposited by using Doctor - Blade technique. SnO_2 thick films prepared were tested with both silver and gold contacts in order to compare with the pellets. The maximum sensitivity achieved for the thick films with silver and gold contacts were around 30 and 100, respectively, when measured at 300 ^{0}C. Thick films with gold contacts presented sensitives at low measuring temperature around 100 ^{0}C.

RESUMEN

En nuestro trabajo hemos utilizado un nuevo método que utiliza la combinación de métodos de síntesis químicos y físicos para la obtención de nano-partículas de SnO_2. En este método, se utilizó principalmente precipitación homogénea química para obtener como primer paso, SnO_2 con tamaño de partícula uniforme y en segundo lugar, los polvos obtenidos fueron tratados mediante la técnica de "ball milling" para disminuir la aglomeración de las partículas y su tamaño. En comparación con otros métodos nuestra ruta de síntesis ofrece partículas de SnO_2 con mucha menor aglomeración. El tamaño de partículas obtenido fue de alrededor de 20-30 nm, con distribución de tamaño homogénea de las partículas. Se empleó urea (R1) y amoníaco (R2) como dos agentes de precipitación para sintetizar los polvos de SnO_2. Los polvos resultantes de SnO_2 fueron dopados utilizando metales de transición: Cu y metales nobles como Pt y Pd a través de dos métodos de dopaje D1 y D2. En D1, los polvos fueron dopados en el volumen y posteriormente molidos, mientras que en D2 fueron molidos y después dopados en la superficie.

Todos los polvos obtenidos, dopados y sin dopar fueron utilizados para fabricar pastillas de SnO_2 utilizando una máquina de prensado manual. Se prepararon pastillas con un espesor de 0.5 mm y 9 mm de diámetro; las cuales fueron presionadas mecánicamente durante un período de tiempo de 90 min utilizando una presión de 16 toneladas. Los efectos de las rutas de síntesis, métodos de dopaje y dopantes utilizados, así como las características estructurales, morfológicas y la sensibilidad a CO, fueron estudiados mediante diferentes técnicas de caracterización y analizados con sus explicaciones detalladas.

Curiosamente, las pastillas de Cu-SnO_2 fabricadas a partir de los polvos obtenidos por el método D1R1, mostraron mayor sensibilidad alrededor de 1782, cuando se mide a 300^0C, en comparación con las pastillas dopadas con Pt y Pd. Después de una búsqueda minuciosa en la literatura especializada, se encontró reportes de valores muy altos de sensibilidad para estos dos metales. Esta alta sensibilidad para las pastillas dopadas con Cu se debe a varias razones tales como a un uniforme y pequeño tamaño de partícula, la formación de cuellos, la conductancia entre partículas y alta absorción de oxígeno debido a fallas de apilamiento. Todas las razones mencionadas anteriormente fueron demostradas al comparar la teoría de sensores establecida con nuestros diversos resultados experimentales.

Adicionalmente, los polvos molidos mediante "ball milling" fueron mezclados con polvos de Al_2O_3 (tamaño de partícula 1μm) para ahorrar los polvos de SnO_2 y también para aumentar la porosidad de la pastilla. La sensibilidad no aumentó en comparación con los resultados anteriores (pastillas después del molido). El valor de sensibilidad máximo obtenido fue de alrededor de 48 y la tendencia al aumento de la sensibilidad con respecto a la temperatura y a la concentración del gas se logró satisfactoriamente.

También se fabricó una pasta viscosa a partir de los polvos de SnO_2 para el depósito de películas gruesas utilizando la técnica “Doctor – Blade”. Las películas gruesas de SnO_2 preparadas fueron probadas utilizando contactos de oro y plata con el fin de comparar sus propiedades con las de las pastillas. La sensibilidad máxima alcanzada para películas gruesas con contactos de plata y oro fue alrededor de 30 y 100, respectivamente, cuando se mide a 300 ^{0}C. Las películas gruesas de SnO_2 con contactos de oro presentan sensibilidad para una temperatura de medición baja, de alrededor de 100 ^{0}C.

PREFACE

The first decade of the 21 century has been labeled by some as the “Sensor Decade.” With a dramatic increase in sensor R&D and applications over the past 15 years, sensors are certainly poised on the brink of a revolution. Just in automobiles alone, sensing needs are growing by leaps and bounds, and the sensing technologies used are as varied as the applications. Understanding sensor design and operation typically requires a cross-disciplinary background, as it draws from electrical engineering, physics, chemistry, and sometimes biology, etc. This reference pulls together the most crucial information needed by those who design sensor systems and work with sensors of all types, written by experts from industry and academia. Tin oxide (SnO_2) material as a solid state gas sensor material has been studied from many years. From the past many years, many synthesis methods were employed to synthesize SnO_2 nanoparticles and we are still far away from the wish to obtain particles with no agglomeration and with similar particle size distribution all over the surface. In this present work, we have studied in detail sensing properties of tin oxide powders, pellets, and thick films. All the possible factors that affect the sensitivity were discussed with our hypothesis and also with the established sensor theory. In this thesis, we attempted to balance breadth and depth in a single, practical and up-to-date resource.

The developed work regarding the tin oxide pellets and thick films is explained in five chapters. Chapter 1 gives introduction to all the theoretical aspects about the sensors and sensing mechanism. While it would be impossible to cover each and every sensor in use today, we attempted to provide as broad a range of sensor types and their applications as possible. In addition, the differences between thin/ thick films and pellet sensors are also presented.

Chapter 2 resumes the different types of materials used in our work and their criteria to choose with corresponding properties. Also in this chapter, we have gave information about the methods employed for manufacturing the pellets and their advantages were explained. A brief literature review about the tin oxide sensors is presented in this chapter. Chapter 3 presents all the experimental procedures and their corresponding equipment details are given.

Chapter 4, the essence of this thesis, presents the detailed analysis of the structural, morphological, optical and sensing properties of the undoped and doped tin oxide pellets, as well as pure tin oxide thick films too. All the results and their analysis are well organized and optimized. A comparison of all the sensitivities with corresponding probable reasons to obtain higher or lower sensitivities in each case are tabulated.

Finally, the conclusions and future work were also remarked. The additional information about some calculations and technical data are provided in Appendixes A, B and C. The other contributors and I have attempted to provide a useful thesis with technical explanations that are clear, simple and thorough. We attempted to keep it modernize with the present technology.

OBJECTIVES

- To synthesize the pure and Cu, Pt and Pd SnO_2 nanoparticles for manufacturing SnO_2 pellets and study their gas sensing properties in a controlled carbon monoxide (CO) and propane (C_3H_8) atmospheres.
- To verify the sensitivity of alumina mixed SnO_2 pellets.
- To obtain the SnO_2 thick films with silver and gold contacts and subsequently study their CO sensing properties.

Particular objectives

- Structural and morphological properties of the synthesized SnO_2 nanoparticles were studied with respect to the effect of
    - Precursor Solvents
    - Precipitant agent type (urea, U, or ammonia, A),
    - Solution molarity,
    - Solution temperature and calcination temperature, T_C
- To optimize the ball milling conditions in order to have a size distribution of nanoparticles narrow.
- To study the effect of doping method, dopant type and synthesis routes on the structural, morphological, optical and gas sensing properties of the SnO_2 pellets.
- To study the effect of alumina mixing ratio on the CO gas sensitivity.
- Effect of annealing temperature on the structural, morphological and gas sensing properties of thick films with silver contacts.
- To study the effect of fabricated transducer with gold contacts on the thick films gas sensor response.

Novelty

- The novelty in our work is the mixture of physical and chemical methods to synthesize the doped and undoped tin oxide nano particles. Also we obtained narrow particle size distribution of the prepared tin oxide nano particles. Additionally we also obtained Cu doped SnO_2 pellets showed higher sensitivity than Pt and Pd doped pellets.

CHAPTER -1

INTRODUCTION

Theoretical aspects of sensors

In this chapter, we present a conceptual resume of different types of sensors and sensing mechanisms, which includes, the importance of Metal Oxide Semiconductor (MOS) gas sensors, gas leakages, factors affecting the gas sensing. Differences between thin films and pellet sensors are also presented.

1.1. Origination of sensor

Fundamentally, the word "Sensor" was originated in 12th century from old French word "*sens"* which means "one of the five senses" and also directly from a Latin words "*sensus*" which means perception and feeling [1]. The primary point that separates a living being from a nonliving being is sensing, which means, only living beings can respond to their surroundings. Built-in sensors within the living beings cause to receive and respond to the environmental changes.

The intention of manufaturing sensors is for improving the daily life and make it easier by inventing new skill full devices which will decrease the human effort to perform the same tasks quickly. In wholly, it became more important to understand about our body functionality and the environmental nature to live longer life and happier than our ancestors which has leaded to the discovery of the five human sense organs: sight, smell, taste, touch, and hearing by Aristotle (384 BC - 322 BC). Beyond these five senses, humans also have awareness of balance (equilibrioception), pressure, temperature (thermoception), pain (nociception), and motion all of which may involve the coordinated use of multiple sensory organs [2].

With the improvement in the technology and electronics, with the base of human sense organs a distinguishable branch of science and technology was originated, namely, the field of sensors and actuators. This branch is interdisciplinary in nature involving physics, chemistry, mathematics, electronics and also sometimes biology.

1.2. Definition of sensor

In general, a *sensor* is a device that converts a physical phenomenon into an electrical signal. Intrinsically, sensors are the interface between the physical world and the world of electrical devices. The other part of this interface is represented by *actuators*, which convert electrical signals into physical phenomena. Sensors and actuators act as extensions of human senses and are quite indispensable in day-to-day life. Sensors act as primary units in information perception. According to the International Electro-technical Committee (IEC), "The sensor is the primary part of a measuring chain which converts the input variable" [3].

The words 'sensor' and 'transducer' are both widely used in the description of measurement systems. As the word 'sensor' is derived from entire meaning 'to perceive' and 'transducer' is from transducer meaning 'to leads cross'. A dictionary definition 'transducer' is 'a device that transfers power from one system to another in the same or in the different form'.

A sensible distinction is to use 'sensor' for the sensing element itself, and 'transducer' for the sensing element plus any associated circuitry. All transducers would thus contain a sensor and most (though not all) sensors would also be transducers as shown in Fig.1.1.

Fig. 1.1. The sensing process.

1.3. Importance of Gas leakages

Gas leak detection is a way of nondestructive testing of dangerous combustible gases from sealed components or systems. Leaks can easily result from poor seals and connections, as well as from inadequate welds. Slow gas leaks from small defects or vibrations can be dangerous, expensive, frustrating, time consuming, and a potential for sickness, death or explosions. For years, contractors and other persons used the old soap and water method which has been proved to be ineffective in detecting the precise location of particularly small gas leaks and is unsafe in laboratory purposes. Recently, gas leak detectors and gas sniffers have become more popular and useful.

Gases are the key measuring elements in many industrial or domestic activities. From past 20 years, the specific demand for gas detection and monitoring has emerged particularly as the awareness of the need to protect the environment. Gas sensors find applications in numerous fields [4, 5]. Individual gases and odor discrimination are the two important groups of applications. Fire detectors, leakage detectors, controllers of ventilation in cars and planes, and alarm devices are individual gas devices. The detection of volatile organic compounds (VOCs), or smells, generated from food or household products has also become increasingly important in food industry and in indoor air quality, and multi-sensor systems (often referred to as *electronic noses*) are the modern gas sensing devices designed to analyze such complex environmental mixtures [6, 7]. Different types of toxic gases and their corresponding problems were discussed in detail in chapter 2.

The Most Common Reasons for Gas Leak Detection are

1. Protect personnel and property: Gas leaks can potentially create serious personnel hazards as well as destroy material and property.

2. Contamination and safety: With stricter OSHA and environmental regulations, the reasons for gas leak detectors are growing.

3. Reliability: Equipment reliability has always been a major reason for gas leak detectors and gas sniffers.

4. Energy loss: With the high cost of energy, losses are increasingly important. By gas leak detection, energy can be saved by conserving the amount of fuel used in a system such as natural gas or propane from leaking out.

Considering it is now 2015, commercial and industrial companies are under more rules and regulations than ever before. When it comes to safety in the workplace, there are numerous governing bodies regulating the way jobs are performed, ensuring that best practices are enforced, and promoting the completion of jobs and tasks in the safest possible way. Gas sensors are required by industry best practices and regulations and are the only way that workplaces can identify gas leaks and potential threats within the workplace. They are extremely important and are a critical piece of safety equipment that can be used to detect explosive atmospheres, oxygen deficiency, and toxic gases that may have leaked into the air. Without gas detectors being used to detect threats, workers are exposed to potentially damaging gases that can cause harm to their minds and bodies, or even result in death.

Gas detectors are great for detecting gases that would not otherwise be smelled by humans in the workplace. However, due to the harsh and rigorous conditions of some job sites and workplaces, gas detectors can be affected and could suffer damages too. Damage to the sensors can be caused by poisons in the air or concentrations of poisons that exceed the gas detector's detectable limit. Dirt and debris can also obstruct the sensor ports of gas detectors, which would prevent the movement of gas into the detector [8].

1.4. Classification of sensors

Main objective for classifying sensors is for bringing an agreement regarding standards for the principles of description and also to systemize the sensor systems. In general, there are a broad range of classification of sensors based on stimulus, application, conversion phenomenon, sensor material, and detection means used in sensor [9]. Some other classifications articulates that the sensor types are, contact and non-contact, active and passive, absolute and relative [10].

In addition to the above sensor classifications, in 1969, Lion innovated a classification of principles based on the "form of energy" in which sensor signals were received and generated, which yielded a *matrix of effects*. Table. 1.1 shows the six energy forms or signal domains generally encountered with examples of typical properties that are measured using those energy forms. By enjoining Fig. 1.1 which shows the sensing process in terms of energy conversion by a transducer and Table. 1.1, which explains the sensor energy forms, sensors can also be classified based on the input and output energies of a transducer. Table. 1.2 (Göpel et al., 1989 [11]), shows the classification of the sensors based on input energy as a primary signal and the output energy as an output signal. This classification is also one method of visualizing the

transduction principles involved in sensing. A rigorous attempt at classifying sensors was undertaken by Middlehoek and Noorlag (1982), in which they represented the input and output energy. From the Table. 1.2, we can articulate that the chemical gas sensors are the sensors with input energy as chemical form and the output energy as electrical form.

Energy Forms	Example measuring parameters
Mechanical	Length, area, volume, all time derivatives such as linear/angular velocity, linear/angular acceleration, mass flow, force, torque, pressure, acoustic wavelength and acoustic intensity
Thermal	Temperature, specific heat, entropy, heat flow, state of matter
Electrical	Voltage, current, charge, resistance, inductance, capacitance, dielectric constant, polarization, electric field, frequency, dipole moment
Magnetic	Field intensity, flux density, magnetic moment, permeability
Radiant	Intensity, phase, wavelength, polarization, reflectance, transmittance, refractive index
Chemical	Composition, concentration, reaction rate, pH, oxidation/reduction potential

Table. 1.1. Sensor Energy Forms

Input Energy	Output Energy					
	Mechanical	Thermal	Electrical	Magnetic	Radiant	Chemical
Mechanical	Mechanical and Acoustic effects; e.g., gravity balance, echo sounder	Friction and cooling effects; e.g., friction calorimeter, thermal flow meter	Piezo-electricity. Piezo-resistivity. Resistive. Capacitive. Induced effect.	Magneto-mechanical effects; e.g., piezo-magnetic effect	Photo-elastic systems; e.g., Interferometer. Sagnac and Doppler effect.	--
Thermal	Thermal expansion and Resonant frequency. Radiometer effect; e.g., bimetallic strip, light mill.		Seebeck effect and Pyroelectricity. Thermo-resistance. Thermal (Johnson) noise.		Thermo-optical effects; e.g., liquid crystals. Radiant emission	Reaction activation; e.g., thermal dissociation.

Electrical	Electro-kinetic and electro-mechanical effects; e.g., piezoelectricity and Ampere's Law.	Joule (resistive) heating. Peltier effect.	Charge collectors. Langmuir probe.	Biot-Savart's Law.	Electro-optical, Kerr and Pockels effects; e.g., Electro-luminescence.	Electrolysis e.g., Electro-migration.
Magnetic	Magneto-mechanical effects; e.g., magnetostriction, and magnetometer.	Thermo-magnetic effects; e.g., Righi-Leduc effect.	Ettingshausen-Nernst effect. Galvano-magnetic effects; e.g., Hall effect.	Magneto-optical effects; e.g., Faraday effect, and Cotton-Mouton effect.	--	--
Radiant	Radiation pressure.	Bolometer. Thermopile.	Photo-electric effects; e.g., photovoltaic effect photo-conductive effect.	Photo-refractive effects. Optical bi stability.	--	Photo-synthesis; e.g., dissociation.
Chemical	Hygrometer. Electro-deposition cell. Photo-acoustic effect.	Calorimeter. Thermal conductivity cell.	Potentiometry Conductometry and Amperometry.Flame ionization. Volta effect. Gas sensitive field effect.	Nuclear magnetic resonance	Emission and absorption Spectroscopy. Chemi-luminescence. Photo-chemical effects.	--

Table. 1.2. Physical and chemical transduction principles.

1.5. Chemical Sensors

A chemical sensor is a self-contained probe that provides in real time information about the chemical composition of its surroundings. The ideal chemical sensor is an inexpensive, portable, foolproof device that responds with perfect and instantaneous selectivity to a particular target chemical substance (analyte) present in any desired medium in order to produce a measurable signal output at any required analyte concentration. Such ideal chemical sensors, however, are far from reality in spite of enormous advances over the past decades. Chemical sensors in actuality are complex devices, generally optimized for a particular application.

Main advantages of chemical sensors are as follows [12]:

- Substitution of standard analytical procedures by fast detection and analysis using dedicated sensors.
- Automation of the analysis and monitoring of chemical quantities.
- Field analysis by means of portable instruments.

Chemical sensors can also be defined as devices or instruments that determine the detectable presence, concentration, or quantity of a given analyte. Chemical sensing is recognition of molecular structure or associated reactivity among a huge number (>10^6) of known molecular substances; this recognition aspect is called selectivity.

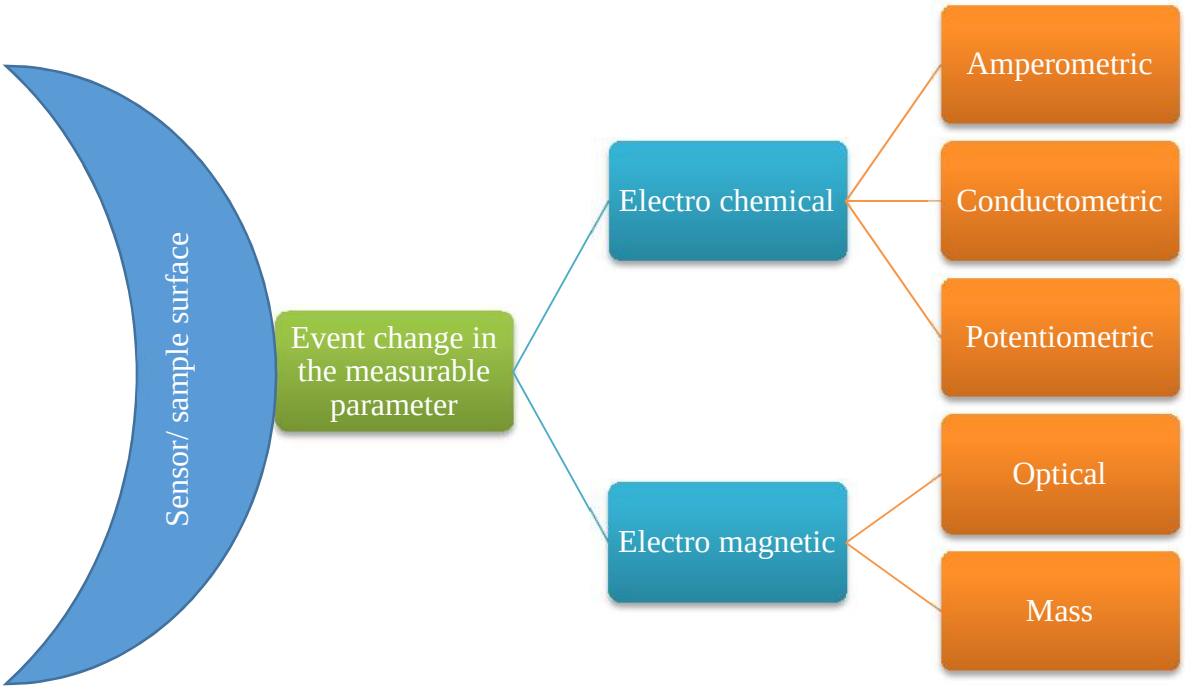

Fig. 1.2. Chemical sensors direct-reading.

Sensitivity and limit of detection relate to the quantity or concentration of the element or molecule to be analyzed (the analyte). The challenge of attaining the needed sensitivity in chemical sensing is comparable to that of achieving the needed selectivity. The sensitivity and selectivity aspects of chemical sensing are affected by the structure type, dimensional, and temporal aspects of the desired determination. The analyte can be present in a gas, liquid, or solid phase on various dimensional scales ranging from bulk volumes of liters to pico-liters, or surface layers from nano scale to mono molecular scale [13]. Chemical sensor directly reads the existence of a selective recognition event that results in a change in a measurable parameter. Selected transduction parameters and generic device types are summarized schematically in Fig. 1.2.

1.6. Importance of Metal Oxide Semiconductor (MOS) Gas sensors

For portable field instrument development there are three major classes of chemical sensor technologies. These sensors, by no means, represent all available sensor technologies; rather, they serve as promising, representative technologies for miniaturization into portable instruments. Primarily, *the chemiresistors*, are the simplest of the chemical sensor technologies available for miniaturization into field instruments. Chemiresistors possess advantages of compact size, simple fabrication, low cost, and simple measurement electronics but are hampered by limitations in signal-to-noise ratio [14].

Secondarily, the potentiometric *CHEmical Field-Effect Transistor* (CHEMFETs), are more complex solid-state sensors. The CHEMFETs, in general, are capable of higher signal-to-noise ratios than the chemiresistors but are inherently more complex to fabricate and require more extensive control and measurement electronics. These characteristics increase their cost and limit the number of CHEMFETs that can be placed inside a single device [15, 16].

Finally several other major classes of solid-state chemical sensor technologies are practical for field portable instruments, such as the mass sensors (surface acoustic wave, bulk acoustic wave, etc.). All three classes of sensors have in common successful products on the macro scale, which make them likely candidates for successful miniaturization in commercial products. Each method has its particular disadvantages and advantages and these are tabulated in Table. 1.3 [17].

First semiconductor oxide gas sensor was proposed in 1962 [18] and have been subjected to extensive research and development and have now grown to be important devices for detecting the leakage of several inflammable gases like town gas and some toxic gases like CO [19-22]. In recent years, much research effort has been directed to the detection of low concentrations of gases such as odorous components [23, 24], O_3 [25], and NO [26]. To meet such low-level gases, the sensors should be highly upgraded in sensitivity, selectivity and stability.

Technology	Sensitivity	Selectivity	Robustness	Power	Size	Overhead
Chemiresistor: MOS	Moderate	Moderate	Moderate	High	Small	Low
Chemiresistor: conducting polymer	Moderate	Poor	Moderate	Low	Small	Low
CHEMFET: Basic	High	Moderate	High	Moderate	Medium	Moderate
CHEMFET: ISFET	High	Moderate	Moderate	Moderate	Large	Moderate
Optical: Surface-plasmonic resonance (SPR)	High	High	Moderate	Moderate	Moderate	High

Table. 1.3. **C**omparison of three types of chemical sensor technologies [17].

Although semiconductor gas sensors have so far been developed mostly by empirical research, further development and innovation seem to be impossible without a fundamental understanding of the gas-sensing mechanisms and sensor design principles involved, which have largely been ignored.

General requirements put forward to all types of operational elements of MOS sensors are the following: semiconductors should have substantial chemical durability, they should not form stable chemical compounds with the particles absorbed (Adsorption mechanism is discussed in detail in section 1.7). Moreover, they should possess sufficient thermal and mechanical strength. Metal-oxide semiconductors, such as ZnO, SnO_2, TiO_2, and others suit above requirements the best. Apart from that such broad band gap semiconductors, they exhibit a high surface oxygen adsorption (if contrasted to elementary ones), which is explained by small free charge carriers concentration. Therefore exceptionally high sensitivity because of their numerous electro-physical properties for any dopant used**.**

1.7. Gas Sensing Mechanism

An oxide semiconductor gas sensor detects an inflammable gas from a change in electric resistance of a polycrystalline element. As Wagner and Hauffe [27] discovered in 1938, adsorbed atoms and molecules on the surface of a semiconductor influence its properties, such as conductivity and surface potential. Later, many researchers [28-30] studied these effects on semiconductor electric conductance. The first applications of these discoveries arrived soon after the production of the first chemo-resistive-semiconductor-gas sensors. Since that moment,

technology development and the problem of toxic and pollutant gas monitoring encouraged improvements in the production and in the performances of different kind of gas sensors. A large part of commercial gas sensors [31] are built with SnO_2, while TiO_2 and ZrO_2 are often employed for devices aimed towards combustion monitoring. It is unanimously agreed that the resistance change on exposure to the gas arises through a surface phenomenon of the oxide semiconductor used [32-34], but this is only a part of the whole gas-sensing processes taking place in the sensor element.

1.7.1. Adsorption-desorption mechanism

Adoption of energy values is possible by the electrons which stay inside certain ranges or more specifically bands of energy in a crystal. Energy bands where no electronic states exist, called *band gap* (E_g). In a semiconductor the highest energy band occupied by fundamental state electrons is called *valence band*, whereas the upper band, in which electrons can be promoted, is called *conduction band*. Conduction band would be completely empty in a perfect crystal at 0 K. However, we remark that solids have an imperfect structure, as a consequence electrons are present in the conduction band or miss in the valence band. Therefore, semiconductors applied on gas sensing are based on the fact that the surface electrons could be transferred or removed from the conduction band, in order to induce consistent variations in the conductivity of the material. Semiconductor band model is shown in Fig. 1.3(a), where electron energy is on the x-axis, while the distance inside the crystal is on the y-axis. The energy gap E_g represents the demanded energy for valence electron excitation (promotion to conduction band).

For example in case of SnO_2, whose E_g is around 3.6eV, the n-type conductivity is due to the oxygen vacancies derived from the typical stoichiometric defects of the material. These vacancies can be singly or doubly ionized and they act as donor states with energy levels positioned at 0.03 and 0.015eV under the bottom of the conduction band [34]. Therefore, in an n-type semiconductor as shown in Fig. 1.3(b), donor states give electrons to the conduction band and enhance the conductance of the material. As a consequence of this overpopulation of electrons in the conduction band, the Fermi level is raised. Once an external oxidizing gas molecule adsorbs on the surface of the crystal then, on the surface of the crystal, an abrupt perturbation in the periodicity of the crystal lattice takes place. Thus, surface atoms or ions have an incomplete coordination number (number of first neighbors), which causes a rearrangement and a greater reactivity in comparison to that of bulk atoms or ions. The interruption of lattice periodicity is enough to create *intrinsic localized electronic states* at surface level [35]. These intrinsic localized electronic states present on the surface of the crystal acts as acceptor and donor energy levels. As one can observe, all surface states are not at the same energy level. Fig. 1.3(c) below shows the band model with the crystals surface and the presence of surface states [36].

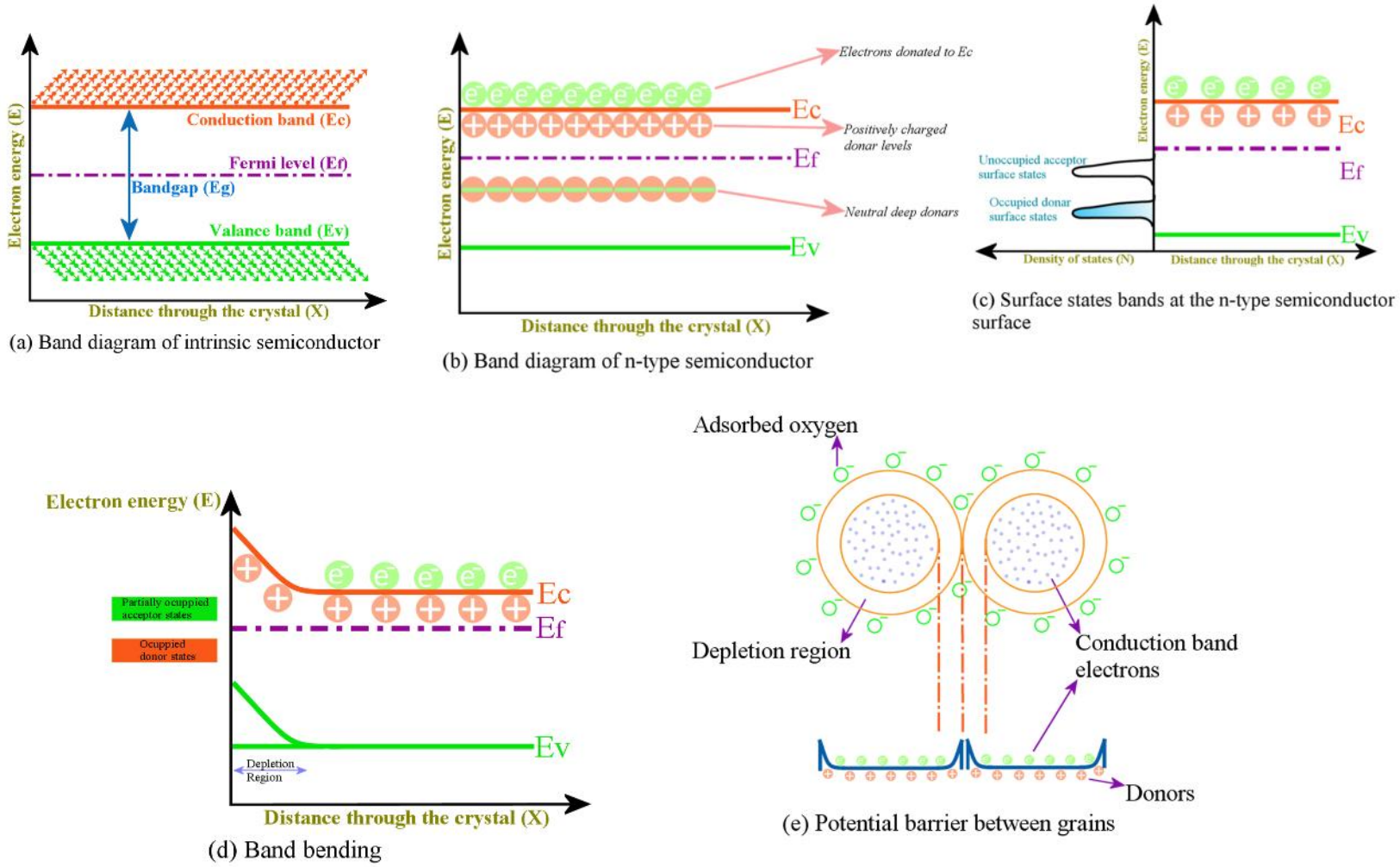

Fig. 1.3. Fermi function and band diagram for semiconductors; (a) intrinsic semiconductor; (b) n-type semiconductor with deep and shallow donors.

The case when there is no net charge is used for simplicity. This is the so-called *flat-band case*. But the flat-band case is an unstable situation. The electrons in the conduction band are at a much higher energy level than the energy level of the acceptor surface states. Thus, they will move from the conduction band to those lower-energy states, forced by this new energetically more favorable configuration. When such transitions occur, a charge builds up at the surface and a countercharge in the bulk (the countercharge being that of the donor ions). This charge and counter charges creates and electric field and further a depletion region is formed on at the surface. Fig. 1.3(d) shows an n-type semiconductor after the charge has moved from the donor ions to the surface states and depletion region.

A scheme of two grains of metal-oxide powder is depicted in Fig. 1.3(e), where the space-charge region around the surface and at the contact point is shown. The oxygen species adsorbed will create the surface-charge layer, which acts as an inter-granular potential barrier, and is called as *Schottky barrier*. The conduction electrons have to overcome this Schottky barrier, in order to go from a grain to another.

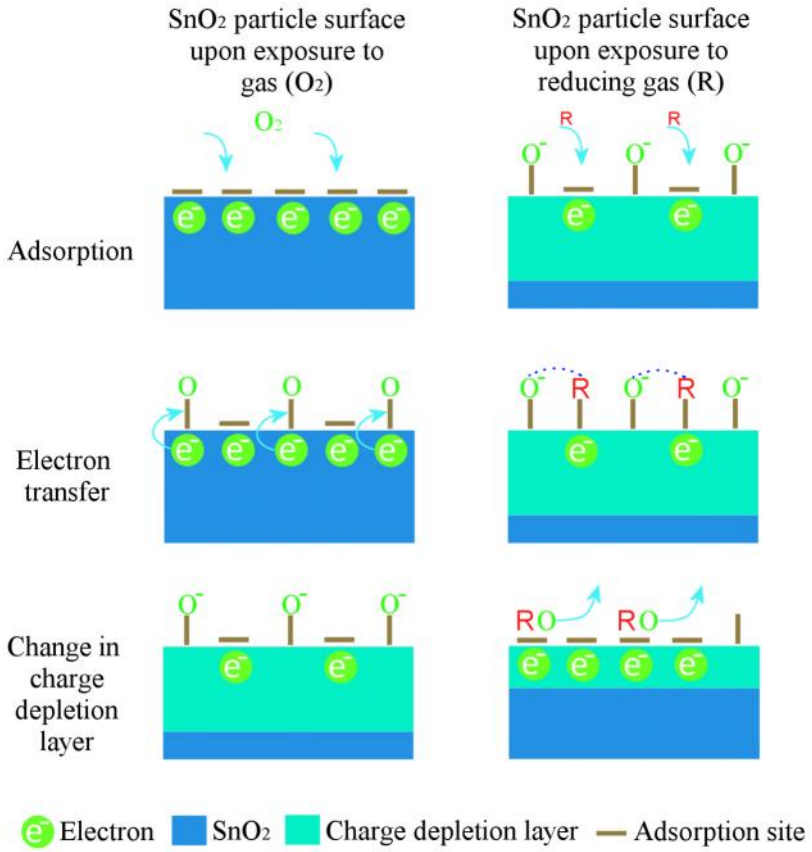

Fig. 1.4. Schematics indicating the sensing mechanism on the SnO_2 surface. Left column indicates reaction with oxygen, whereas right column shows the interaction with reducing gas like CO.

To summarize the general steps involved in sensor response upon exposure to air and to a reducing gas, *R*, are shown in Fig. 1.4. In our case, where tin oxide (SnO_2) is the semiconductor material used, as shown in the left column of Fig. 1.4. Oxygen from the air is adsorbed onto the surface of the SnO_2. Electrons from the surface region of the SnO_2 are transferred to the adsorbed oxygen, leading to the formation of an electron-depleted region near the surface of the SnO_2 particle. The electron depleted region, also called the space-charge layer, is an area of high resistance and the core region of the particle, where electron densities are high, is an area of relatively low resistance [37]. The form of the adsorbed oxygen (either molecular or atomic) depends on the temperature of the sensor (refer section 1.8 Temperature effect on sensing). As shown in the right column of Fig. 1.4, when exposed to a reducing gas like CO, surface reactions shown in equations 1.1 and 1.2, which release electrons back to the SnO_2 and lead to a decrease in the resistance of the space charge layer.

$$CO + O^-_{ads} \rightarrow CO_2 + e^- \quad (1.1)$$

$$2CO + O^-_{2,\,ads} \rightarrow 2CO_2 + e^- \quad (1.2)$$

1.7.2. Physisorption and Chemisorption mechanism

When a gas or vapor comes in contact with a clean solid surface, some of it will adhere to the surface in the form of an adsorbed layer. The solid is generally referred to as the ***adsorbent*** and the adsorbed gas or vapor as the *adsorbate*. Reason for adsorption is for reducing the imbalance of attractive forces which exists at a surface, and, hence, the surface free energy of a heterogeneous system. Adsorption occurs when an attractive interaction between a gaseous particle and a solid surface is strong enough to overcome the disordering effect of thermal motion.

Physical adsorption or physisorption takes place, if weak Van der Waals forces are involved in the interaction. Indeed, physisorptive bonds are characterized by dissociation energies below approximately 50 kJ/mol. Strong forces are responsible for chemisorption and cause the formation of short chemical bonds with dissociation energies typically exceeding 50 kJ/mol. Since an activation barrier needs often to be overcome, chemisorption is considered an activated process [38, 39].

The equilibrium condition in physisorption is attained rapidly, since there is no activation energy involved and the process is readily reversible. On the other hand, chemisorption may require an activation energy, as already written, and may, therefore, be relatively slow and not readily reversible. Fig. 1.5 illustrates a schematic potential diagram for the adsorption of a diatomic molecule of gas, X_2, on a surface, M.

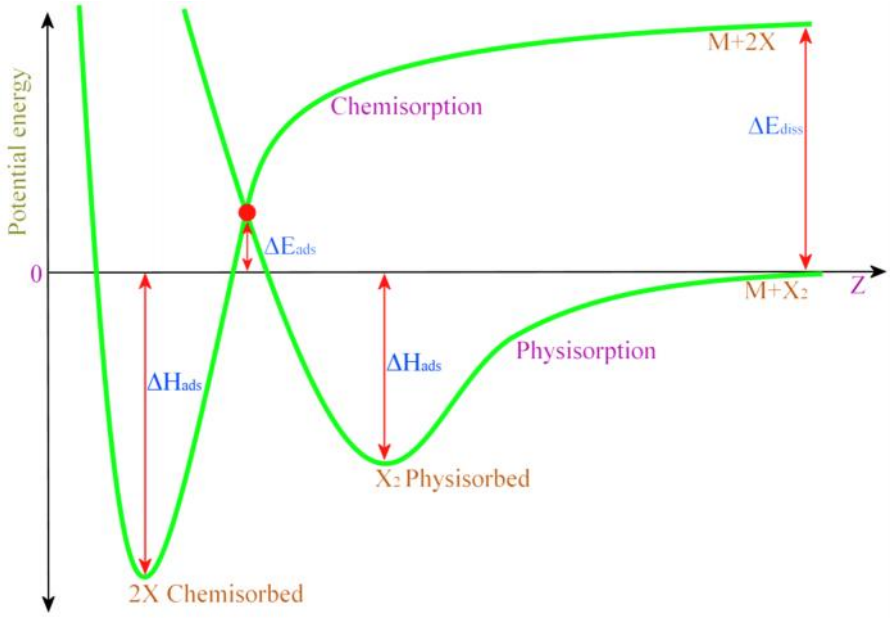

Fig. 1.5. Potential energy curves for physisorption and chemisorption of a molecule X_2 that approaches a surface along the trajectory z.

The physical interaction energy includes a short-range negative (attractive) contribution arising from London-Van der Waals dispersion forces [39] and an even shorter-range positive contribution (Born repulsion) due to an overlapping of electron clouds. In chemisorption, the adsorbate, X_2, dissociates to 2X. The dissociation energy of X_2 (ΔE_{diss}) is represented at large distances. Both potential curves are characterized by the presence of a minimum, which corresponds to the heat of the process (ΔH_{ads}). The heat of chemisorption is at a shorter distance from the solid surface than the heat of physisorption. Chemisorption causes band bending, which changes the surface resistance of the material. In Chemisorption, the adsorption of an electron acceptor on the surface creates acceptor surface level (E_{SS}), where the electrons of the conduction band are trapped creating a depletion region. The accumulation of the negative charge at the surface makes further transfer more difficult as shown in Fig. 1.3.

1.7.3. Gas sensing mechanism for doped sensors

Decreasing the semiconductor material crystallite size can dramatically improve sensor sensitivity; however, the small dimensions required are difficult to achieve in a practical sensor. For example, sensors composed of nanosized SnO_2 crystallites with particle size < 10 nm can have poor mechanical strength [40], and heat treatment processes tend to increase the characteristic SnO_2 crystallite size (which is discussed further in Chapter 4).

In many gas sensors, the conductivity response is determined by the efficiency of catalytic reactions with detected gas participation taking place at the surface of gas-sensing material. Therefore, control of catalytic activity of gas sensor material is one of the most commonly used means to enhance the performance of a gas sensor. However, in practice, the widely used gas sensing metal oxide materials such as TiO_2, ZnO, SnO_2, Cu_2O, Ga_2O_3, Fe_2O_3, among others, are the least active from the catalytic point of view [41]. The pure SnO_2 without any catalyst exhibits a very poor sensitivity (~3), confirming this statement [42, 43].

In order to modify or control the surface properties, introduction of noble metal additives is usually performed. The most important effects of noble metal addition are the increase of the maximum sensitivity and the rate of response, as well as the lowering of the temperature of maximum sensitivity and selectivity to certain gases. All these effects arise as a consequence of the promoting catalytic activity when loading with noble metals like Pt and Pd.

Noble metals are high-effective oxidation catalysts, and this ability can be used to enhance the reactions on sensor surfaces. A wide diversity of methods, including impregnation, sol-gel, sputtering and thermal evaporation, has been used for introducing noble metal additives into semiconductor oxides. Different doping states can be obtained by different methods. Two different mechanisms have become widely accepted for describing the chemical and physical processes with additives: the electronic and the catalytic mechanisms. Fig. 1.6 shows the general steps involved with the two mechanisms.

1.7.3.1. Chemical sensitization: In this, the action of the additive is in general two-fold [44]: a) the metallic cluster presents a higher sticking coefficient to gases than the semiconductor, and b) on the cluster, nearly all the gas molecules are dissociated, being the dissociation products, they spilt over the semiconductor support. Thus, it generally consists in the adsorption on the catalyst followed by diffusion from the catalyst to the support. Because the activation energy for desorbing is much higher than for diffusing, the support can act as source of reactant supply, although the opposite case or both can also occur. Moreover, normally the support is assumed to be catalytically inactive, but not always it is true.

1.7.3.2. Electronic sensitization: In this, there is an electronic interaction between the catalysts and the semiconductor through the space charge created in the semiconductor by the presence of the surface clusters. Additives at the surface of the semiconductor act as receptors while the semiconductor acts as a transducer of the changes taking place at the surface under gas adsorption. The oxidation state of the particles changes in contact with a gas, inducing the corresponding change in the electronic state of the semiconductor.

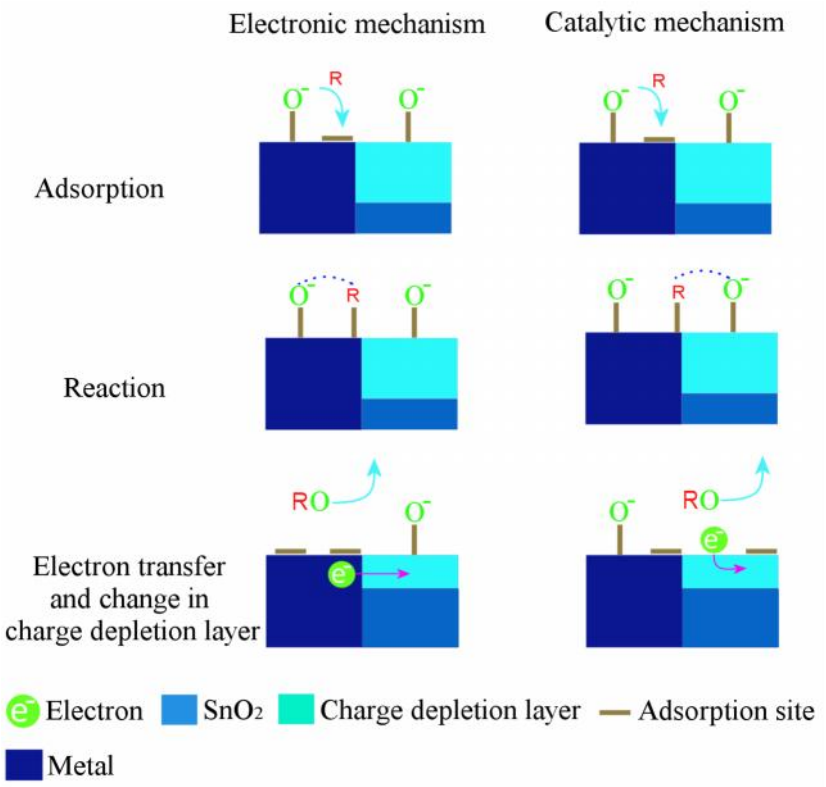

Fig. 1.6. Schematic indicating the general steps involved in the electronic (left column) and catalytic (right column) mechanisms active in SnO_2 sensors with metal additives. *R* represents a reducing gas.

1.8. Sensor parameters and factors influencing Gas Sensing

In order to characterize sensor performance a set of parameters are used [45]. The most important parameters and their definitions are listed below.

- **Sensitivity:** It is a change of measured signal per analyte concentration unit, i.e., the slope of a calibration graph. This parameter is sometimes confused with the detection limit.
- **Selectivity:** It refers to characteristics that determine whether a sensor can respond selectively to a group of analytes or even specifically to a single analyte.
- **Stability:** It is the ability of a sensor to provide reproducible results for a certain period of time. This includes retaining the sensitivity, selectivity, response, and recovery time.
- **Detection limit:** It is the lowest concentration of the analyte that can be detected by the sensor under given conditions, particularly at a given temperature.
- **Dynamic range:** It is the analyte concentration range between the detection limit and the highest limiting concentration.
- **Linearity:** It is the relative deviation of an experimentally determined calibration graph from an ideal straight line.

- **Resolution:** It is the lowest concentration difference that can be distinguished by sensor.
- **Response time:** It is the time required for sensor to respond to a step concentration change from zero to a certain concentration value.
- **Recovery time:** It is the time it takes for the sensor signal to return to its initial value after a step concentration change from a certain value to zero.
- **Working temperature:** It is usually the temperature that corresponds to maximum sensitivity.
- **Hysteresis:** It is the maximum difference in output when the value is approached with an increasing and a decreasing analyte concentration range.
- **Life cycle:** It is the period of time over which the sensor will continuously operate.

All of these parameters are used to characterize the properties of a particular material or device. An ideal chemical sensor would possess high sensitivity, dynamic range, selectivity and stability, low detection limit, good linearity, small hysteresis and response time, and long life cycle. Investigators usually make efforts to approach only some of these ideal characteristics, disregarding the others. On one hand, this is because the task of creating an ideal sensor for some gases is extremely difficult, if at all possible. On the other hand, real applications usually do not require sensors with all perfect characteristics at once.

There are several parameters that have to be considered affecting the sensitivity, starting from operation temperature, humidity, thickness of samples, microstructure, catalysts, gas concentrations, chemical composition, etc.... According to our experience in this work, we can assume that, the two major factors are microstructure and temperature, which are discussed in the following sections.

1.8.1. Microstructure

The operating characteristics of solid state gas sensors are determined by both receptor and transducer functions. The last function is very important, because it determines the efficiency of chemical interactions conversion into electrical signal. Therefore, it is very important to synthesize metal oxides with optimal morphological and structural properties.

Important factors in the transduction process include the microstructure of the sensing surface, the chemical interactions occurring on the surface and the operating temperature. The microstructure of a sensor material is important for two reasons [45]:

- Microstructure affects the distribution of adsorption sites.
- Microstructure will affect electrical transport properties.

If it is possible to decrease the crystallite size of SnO_2 particles to a sufficiently small value, the gas sensitivity would be increased, as it was observed that the gas sensitivity of tin oxide-based elements was inversely proportional to the crystallite size. This behavior can be extended

to other materials as well. Moreover, since SnO_2 sensors are usually operated at temperatures above 200^0C in the presence of oxygen, their long term stability requires thermodynamically or kinetically stabilized interface structures.

Chemical reactions occurring on the surface are transduced to electric signals by means of the electrodes in contact with the sensitive material. Reactions may occur at different points of the sensors, depending on its morphology. Two cases may be distinguished:

- Compact and structurally homogeneous sensitive layer, in which the electron flow is parallel to the solid-gas interface, or even to the space charge layer; thus, the interaction with the gases occurs just on the top of the surface (see Fig. 1.7, such layer is obtained by most of the techniques used for thin film deposition);
- Porous and not thin sensitive layer, made of partially sintered grains, where electrons are forced to overcome the inter-granular barrier; therefore, in this case, a certain thickness of material is available for reactions, because of the porosity, and the active surface is higher in comparison with the first case (see Fig. 1.8, such layer is typically a thick film or a pellet).

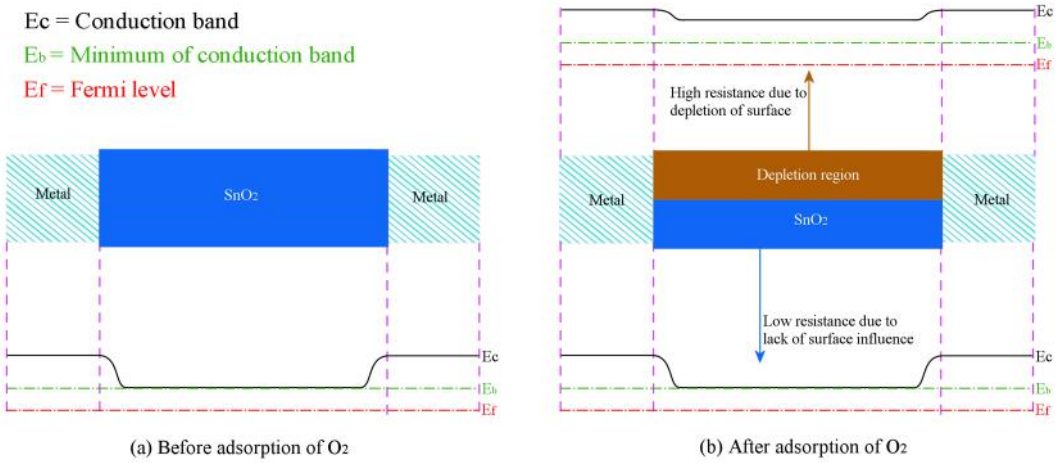

Fig. 1.7. Gas detection in a densely packed thin film. Energy band diagram, both in the absence of gases (left); and in an oxygen rich atmosphere (right) [46].

In a densely packed thin film (Fig. 1.7), under gas adsorption a depletion region near the surface appears. In this case, the behavior of the conductance is that of a bulk trap limited conductance in a layer of variable width (film thickness-width of the surface charge region), in which the activation energy for conductance would be the donor energy [47]. Depending on the coverage by chemisorbed species and film thickness, the whole film can be depleted of electrons. In this case, conductance is surface trap limited, i.e., the conductance is determined by the equilibrium between conduction band states and surface states. The activation energy for the conductance would be the surface state energy [47]. In this case, conductance is directly affected by surface reactions.

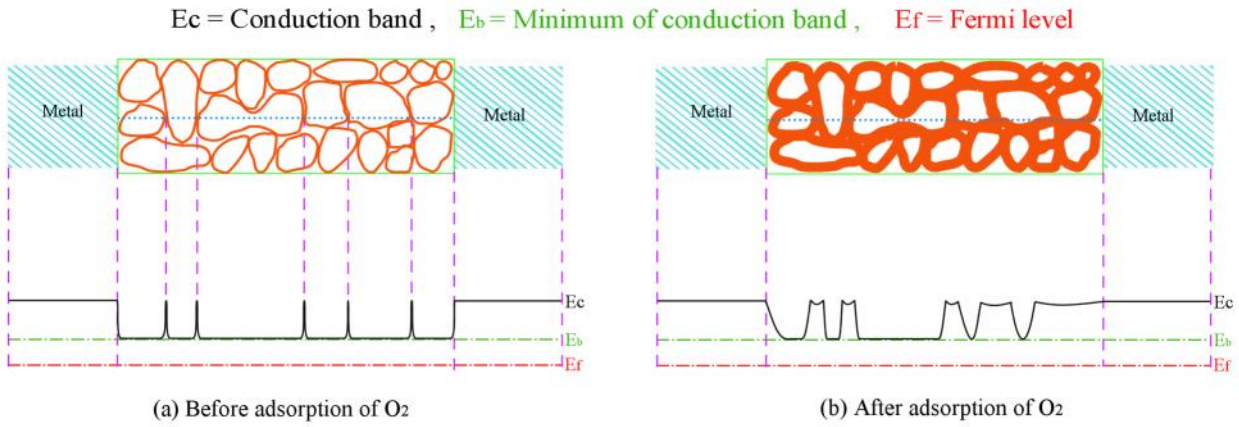

Fig. 1.8. General scheme of a porous sensor containing both grain boundaries and necks in the absence of gases (left); and in the presence of oxygen (right) [46].

The case of a porous body (thick film) is qualitatively different (Fig. 1.8). The porous body is formed by low-resistance paths through the bulk of the crystallites, alternating with higher resistance constrictions at the points of contact. Several cases may be considered, depending on the microstructure of the film or pellet [47], being formed by grains interconnected by grain boundaries, the typical situation described in thick films or pellets.

In this situation, the bulk of each grain can be considered neutral such that, an ohmic behavior is expected. At grain boundaries charge is trapped from the ambient and depletion regions develop. The conductivity would be limited by charge transport across Schottky barriers by thermionic emission, or usually, by tunneling less. The activation energy for conductance would be the barrier height and would be directly affected by the charge and fractional coverage of the surface species. A schematic representation of the pellet and thin films situations is depicted in Fig. 1.9 [48].

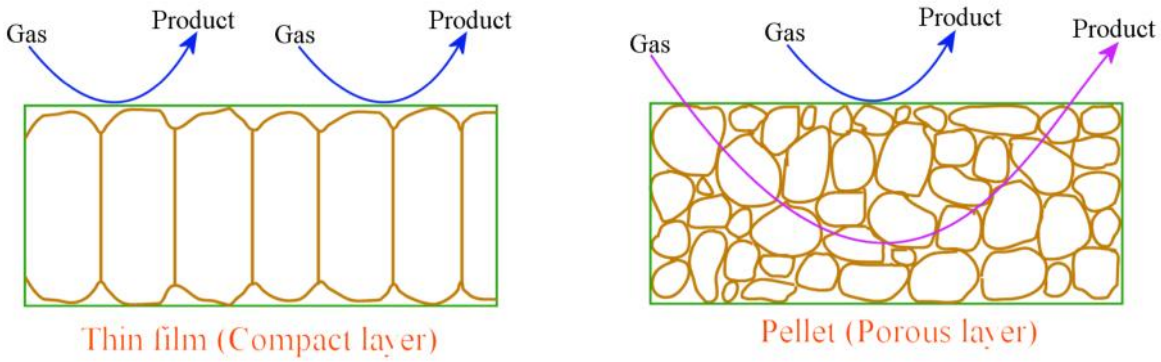

Fig. 1.9. Schematic layout of a typical resistive gas sensor.

The other situation in thick films, less common, is when the film is formed by grains interconnected by necks; in this case, surface states corresponding to the gas species adsorbed cause a depletion zone extending to a certain depth. Fig. 1.10, shows the various regimes that are of interest in sensors based on the relative values of the neck width and the Debye length. Park and Akbar [49] proposed that, the inter-granular contacts between particles can be classified into three categories: open neck, closed neck and Schottky contact-type connections. Specific conductance models are associated with each category of inter particle connection. Fig. 1.10 includes the inter particle models of Park and Akbar, as well as the regimes based on characteristic grain and particle sizes proposed by Shimizu [50].

The dramatic dependence of sensor sensitivity on particle size can be understood by considering the size regimes outlined in Fig. 1.10. As the crystallite dimension decreases relative to the Debye length of the electrons in the material, the sensor conductance becomes dominated by the high resistance of the inter particle necks. Under these conditions, the sensor sensitivity is a very strong function of the necks size between particles.

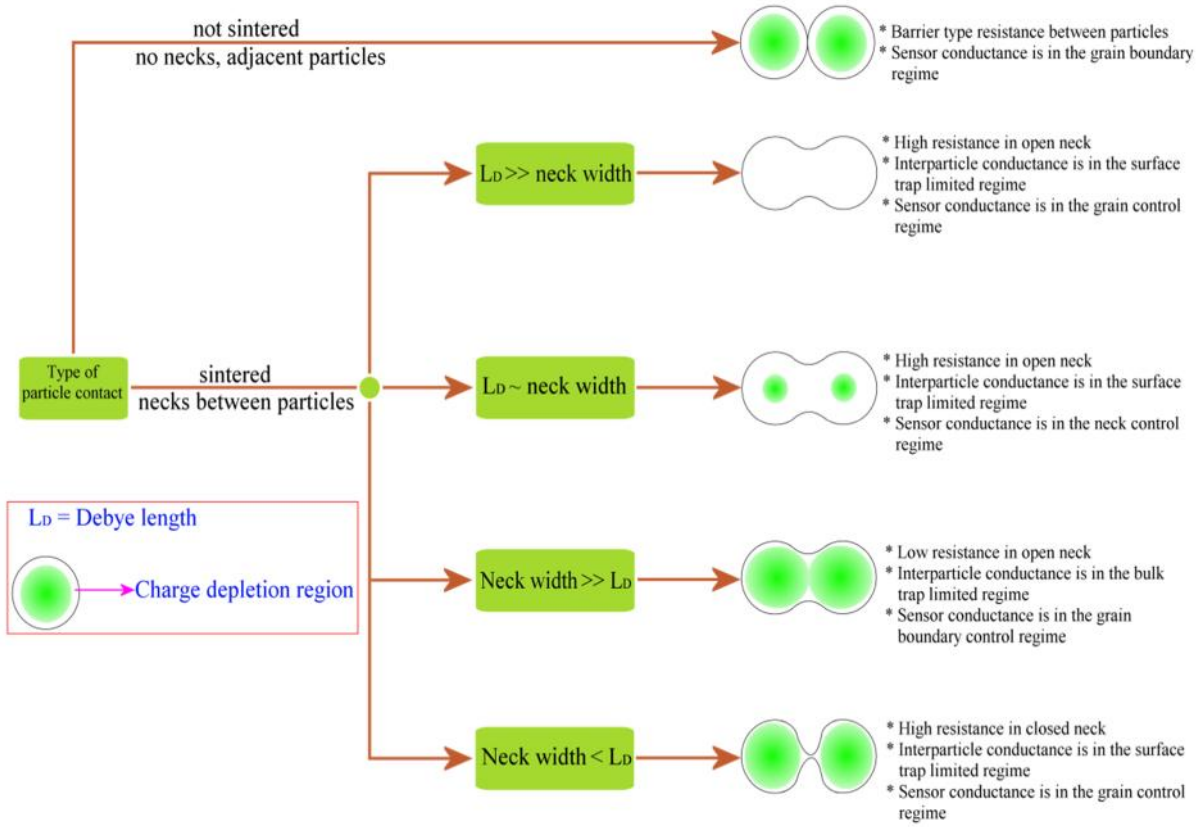

Fig. 1.10. Schematic indicating the conductance mechanisms important in the various SnO_2 crystallite size regimes, relative to the SnO_2 electron Debye length, *L*D

Additionally, high surface to volume ratio is also crucial parameter. However, high surface to volume ratio can be obtained not only by reducing grain size, but also by highly-ordered pore structure such as mesoporous structure or nano tube arrays. The very high surface/ volume ratio of mesoporous materials has attracted much attention in the application of gas sensors [51, 52]. However, the most of such mesoporous structured metal oxides are not stable after the removal of surfactant and pore structure would collapse at high temperature [52]. High surface areas make them excellent supporting materials, which can obtain well-dispersed gas sensor materials or catalysts.

Some general aspects were assigned for the functioning and employing of these materials in their different shapes, being single crystals, homogeneous thin films, porous thick films or partially synthesized grain layers [53]:

- The presence of oxygen is even necessary, in order to detect burner gases;
- As the temperature becomes higher, the sensitivity to a particular gas increases until it reaches a maximum value, afterward it decreases, approaching to zero for higher temperatures;
- The response in function of temperature is a logarithmic curve in a wide range of concentration, therefore low gas concentrations give an high differentiation, while this does not occur with greater concentrations;
- The response time to a rapid variation of concentration depends on both the nature of the gas and the working temperature; a quick starting response is often followed by a slower approach to the equilibrium (several hours in some cases);
- The response to burner gases is generally non selective;
- The presence of water vapor ponderously affects the response.

1.8.2. Temperature

Temperature has pronounced effects on the sensitivity of SnO_2 gas sensors, as it influences the physical properties of semiconductors (change of the free carrier concentration, Debye length,…), but also because every reaction taking place at the surface, as well as the most probable species adsorbed and, hence, the reaction sites, are temperature dependent. In the case of gas sensing application, we are concerned about the temperature effect on the properties related to the processes occurring at the surface of the sensor. For example, Adsorption and desorption processes are temperature activated processes, as well as surface coverage by molecular and ionic species, chemical decomposition, reactive sites.

In this way, dynamic properties of the sensors such as response and recovery time and the static characteristics of the sensor depend on the operation temperature. Every sensor presents an optimum operation temperature because, the electrical conductivity of metal oxides

is dependent on gas adsorption which changes with change in the temperature. However, the interpretation of adsorption mechanism depending on the temperature is still controversial [54]. Two models have been proposed until now: the first one is based on oxygen ionosorption, while the second one on oxygen vacancies. Gas sensor response can be interpreted by both these mechanisms, which can be applicable at the same time [55].

At temperatures within 100 ^{0}C and 500 ^{0}C, the interaction between the surface of an n-type semiconductor, e.g. SnO_2, and atmospheric oxygen leads to its adsorption in the form of molecular (O^-_2) and atomic (O^- and O^{2-}) ions. Ionosorption does not envisage chemical bond: the adsorbate is electro statically stabilized in the vicinity of the surface and acts as surface state, trapping electrons from the conduction band [56-59]. Oxygen adsorption can be described in the equations 1.3 and 1.4.

$$O_2 \text{ (gas)} + e^- \Longrightarrow O^-_2 \text{ (ads)} \qquad (1.3)$$

$$O^-_2 \text{ (ads)} + e^- \Longrightarrow O^{2-}_2 \text{ (ads)} \Longrightarrow 2O^- \text{ (ads)} \qquad (1.4)$$

The molecular form is supposed to be dominant below 150 ^{0}C, while above this temperature the atomic forms dominate [38]. However, we usually do not consider O^{2-}, because such a high charge on the ion can give instability, and O^- is reckoned to be as the most reactive species in presence of reducing gases [37].

The presence of adsorbed oxygen ions leads to the formation of a depletion layer at the surface of tin oxide and to a high resistance. When reducing gases, such as CO, approach the surface of the sensor, they react with the oxygen ions and release electrons, which return to the conduction band. The final effect will be a decrease of resistance and thus increase of sensor conductivity. Temperature effect on the sensitivity of the doped semiconductors with their corresponding possible explanations were tabulated in Table. 1.4.

Thus, in general, for a given additive, its distribution through the support and loading will have important effects on the device response in addition to that arising from the nature of the catalytic material itself. Indeed, it has been observed that the maximum gas sensitivity depends, for a given metal additive, even on the loading method (fixation, impregnation, metal evaporation…) [60] and the general response is influenced not only by the chemical state of the catalyst but also by its crystalline structure [61, 62].

On the other hand, the operation temperature of the sensor can also determine the real function of the additive as, for example, spill- over can only occur at certain temperatures, which may depend on the gas.

Temperature(^{0}C)	Possible explanations with doping for sensing
<100	• The rate of CO and oxygen adsorption is high • The magnitude and growth rate of the conductivity under CO are maximum. • The response time is minimum.
100-300	• Desorption rate increases, and the superficial migration of the oxygen and the reactants at the tin oxide surface becomes possible, corresponding to a chemical sensitization by spillover effect. • The response time grows and the conductivity curve does not reach the saturation
>300	• The oxidation of CO becomes possible on all the surface of tin oxide. • The area of the working surface increases and the saturation value is quickly reached. • Quantity of adsorbed CO in this temperature range is smaller, leading to a diminution of the conductance

Table. 1.4. Effect of temperature on the sensitivity of the doped semiconductor

Finally, the fundamental principles underlying how the additives lead to the enhancements of sensor performance are still not well understood. Advances are also complicated by the fact that the additives probably play multiple roles in augmenting the sensor performance. Consequently, the methods for how to select an additive and design the combined sensor/additive morphology remain a challenge.

1.9. Differences between thin films and pellets

In this section will tabulate the differences between the films and pellets which resumes out the advantages and disadvantages of both films and pellets. Table. 1.5 below shows the differences between the films and pellets.

Films	Pellets
Formed by finely dispersed particles of very small size very densely packed, forming a quasi-continuous layer (see Fig 1.7)	Composed of poorly bounded grains of variable sizes (see **Fig 1.8**)
Presents a lesser effective surface area for gas adsorption compared to pellets	Presents a higher effective surface area for gas adsorption
Will have a higher speed of response	Will have lower speed of response due to the gas diffusion into the bulk

The steady state positions achieved faster which avoids the impartation of the absorbed molecules from the surface.	The adsorbed molecules can leave back in the gas phase if overcome some potential barrier determined usually as the heat of adsorption (temperature effect)
Low power consumption	higher power consumption
Substantially contaminated	Less susceptible to contamination
Less sensitive	More sensitive
Robust	Fragile
Less productivity due to the cost	High productivity and automation
Prepared by sputtering or electron beam evaporation to deposit a thin film onto an electrically and thermally insulating substrate	Prepared by pressing and sintering pellets
Different densification of the film can be obtained by using different deposition techniques	These are always porous bodies or layers
Substrate effects are possible after 450^0C	No substrate effects
Highly expensive	Less expensive

Table. 1.5. Differences between films and pellets.

1.10. Reasons for sensing carbon monoxide (CO) and propane (C_3H_8)

Tin dioxide (SnO_2) *is* the commonly used gas sensing material. It is an n-type granular material whose electrical conductivity is dependent on the density of pre-adsorbed oxygen ions on its surface. The resistance of tin dioxide changes according to the variation of gas concentration (e.g., liquefied petroleum gas (LPG), methane (CH_4), carbon monoxide (CO) and other reducing gases [63, 64], while the relationship between resistance and target gas concentration is nonlinear [65]) Other Metal Oxide Semiconductors (MOS) (e.g., tungsten trioxide (WO_3)) are also widely used for gas sensing. Anodic tungsten oxide applying electrochemical etching of tungsten shows excellent responses towards hydrogen (H_2) and nitrogen oxide (NO) [66] [121]. However, the response of pure WO_3 to NH_3 is rather poor, and because of the interference from NO_x, the selectivity of WO_3 sensors for NH_3 is low. In order to implement WO_3 in gas sensing, WO_3 should be decorated with copper and vanadium as catalytic additives to improve the response, and the abnormal behavior of sensors should be eliminated [67] [122]. Others like titanium dioxide (TiO_2) are also used as sensitive layers for their sensitivity in terms of dielectric permittivity to gas adsorption [68] [123].

1.10.1 CO

CO is a poisonous, colorless, odorless, and tasteless gas. It is a common industrial hazard gas produced from the incomplete burning of gasoline, wood, coal, propane, natural gas or any other system that are powered by carbon-based fuels. Gas leak detection is a manner of constructive testing of dangerous combustible gases. Leaks can easily result from poor seals and connections, as well as from inadequate welds. The Immediate Danger to Life and Health

Concentration (IDLHC) concentration for CO, 1200 ppm, is much higher than for most other toxic gases, making it relatively safe to handle [69].

CO is also one of the main gases of interest in the field of gas sensor applications. It is a target gas in case of fire detection, incomplete burning, etc as well as an interfering gas because of its high reactivity with semiconductor gas sensors. Because of this, it is mostly chosen besides H_2 to characterize sensor performance. In addition, the physical and chemical properties of CO facilitate investigations monitoring CO and its typical reaction product CO_2. A person suffering from carbon monoxide (CO) intoxication may first experience euphoria (similar to the effect of a martini or two), then headache, followed by nausea and possibly vomiting as the concentration of carboxy hemoglobin in the blood increases.

1.10.2 C_3H_8

Propane is a naturally occurring gas composed of three carbon atoms and eight hydrogen atoms. It is created along with a variety of other hydrocarbons (such as crude oil, butane, and gasoline) by the decomposition and reaction of organic matter over long periods of time. After it is released from oil fields deep within Earth, propane is separated from other petrochemicals and refined for commercial use. Propane belongs to a class of materials known as liquefied petroleum gases (LPGs), which are known for their ability to be converted to liquid under relatively low pressures. As a liquid, propane is 270 times more compact than it is as a gas, which allows it to be easily transported and stored as a liquid until ready for use.

At air concentrations below 1000 ppm propane is virtually non-toxic. Brief exposures to 10,000 ppm cause no symptoms; 100,000 ppm can produce slight dizziness after a few minutes of exposure, but is not noticeably irritating to the nose and throat. Close range contact with liquefied propane gas may cause injury characteristic of a thermal burn with swelling, fluid accumulation and extreme redness. Tissue death and gangrene may also develop.

There are no work reported, to the best of our knowledge that deals with the sensing mechanism of C_3H_8 on semiconductor surfaces. Sensor measurements performed with C_3H_8 and other hydrocarbons showed the same dependencies on humidity as Methane (CH_4) [70]. Generally, the rate-limiting step in hydrocarbon sensing is the separation of a hydrogen atom and the subsequent adsorption of the respective alkyl rest. As the C—H binding energy of methane is the biggest among the class of hydrocarbons (443 kJ/mol compared to 413 kJ/mol for primary CH bonds of higher alkanes [71]) the reactivity of higher respectively branched hydrocarbons is higher [72].

References

[1] http://www.etymonline.com/index.php?term=sense&allowed_in_frame=0
[2] http://www.scientificpsychic.com/workbook/chapter2.htm
[3] Terms and Definitions in Industrial Process Measurement and Control (lEC Draft 65/84), International Electrotechnical Committee (1982).
[4] G. Sberveglieri (ed.), Gas Sensors - Principles, Operation and Developments, Kluwer Academic Publishers, Dordrecht (1992).
[5] J. Chou (ed.), Hazardous Gas Monitors-A Practical Guide to Selection, Operation and Applications, SciTech Publishing, (2000).
[6] J. W. Gardner, P. N. Bartlett, Electronic noses – Principles and Applications, Oxford University Press, 1999.
[7] J. W. Gardner, K. C. Persaud (eds.), Electronic Noses and Olfaction 2000: 7th Symposium on olfaction and Electronic Noses, Brighton, UK, July 2000, IOP Publishing (2001).
[8] P. Mielle, F. Marquis, C. Latrasse, Sensor and Actuators B 69, 287-294 (2000).
[9] White, R. W. A sensor classification scheme. In: Microsensors. IEEE Press, New York, 1991, pp. 3–5.
[10] Norton, H. N. Handbook of Transducers. Prentice-Hall, Englewood Cliffs, NJ, 1989.
[11] W. Gopel, W. 1. Hesse, and J. N. Zemel, Sensors: A Comprehensive Survey, Vol. I, Fundamental and GenSemiconductoreral Aspect, Weinheim Verlagsgesellschaft mbH, 3-4 (1989).
[12] KJ8056: Kjemiske og biologiske sensorer / Chemical Sensors and Biosensors.
[13] Ames, B.N., M. Profet, and L.S. Gold. 1990. Dietary pesticides (99.99-percent all natural). Proceedings of the National Academy of Sciences 87(19):7777–7781.
[14] Figaro Engineering Inc. [Online]. Available: http://www.figarosensor.com
[15] Capteur Sensors (recently acquired by First Technology). [Online]. Available: http://www.capteur.co.uk.
[16] MicroChemical Systems. [Online]. Available: http://www.microchemical.com.
[17] OsmeTech plc. [Online]. Available: http://www.aromascan.com.
[18] T. Seiyama, A. Kato, K. Fujiishi and M. Nagatani, A new detector for gaseous components using semiconductive thin films, Anal. Chem., 34 (1962) 1502-1503.
[19] P. J. Shaver, Activated tungsten oxide gas detectors, Appt. Phys. Left., 11 (1967) 255-256.
[20] S. Kanefusa, M. Nitta and M. Haradome, Thick film gas leak detector for town gas, J. Chem. Sot. Jpn., (1980) 1591-1595.
[21] N. Yamazoe, Y. Kurokawa, and T. Seiyama, Effects of additives on semiconductor gas sensors, Sensors and Actuators, 4 (1983) 283-289.
[22] G. S. V. Coles, K. J. Gallagher and J. Watson, Fabrication and preliminary tests on tin (IV) oxide based gas sensors, Sensors and Actuators, 7 (1985)89-96.
[23] T. Nakahara, K. Takahata and S. Matsuura, High sensitive SnO, gas sensor, 1. Detection of volatile sulphides, Proc. Symp. Chemical Sensors, Honolulu, HI, U.S.A., Oct. 18-23, 1987, pp. 55-64.
[24] Y. Shimizu, Y. Takao and M. Egashira, Detection of freshness of fish by a semiconductive Ru/TiO, sensor, J. Electrochem. Sot. 135 (1988) 2539-2540.
[25] T. Takada and K. Komatsu, 0s gas sensor of thin film semiconductor In,O,, Proc. 4th Znt. Conf. Solid-State Sensors'and Actuators (Transducers '87), Tokyo, Japan, June 2-5, 1987, pp. 693-696.
[26] G. Sberveglieri, S. Groppelli and G. Coccori, Radio frequency magnetron sputtering growth and characterization of indium-tin oxide (ITO) thin films for NO, gas sensors, Sensors and Actuators, 15 (1988)235-242.
[27] C. Wagner, K. Hauffe, Ztschr. Elektrochem. 33, (1938) 172.
[28] W.H. Brattain, J. Bardeen, Monograph, (Bell Telephone System Tech. Publs., 1953).
[29] G. Heiland, Z. Phys., 138, (1954) 459.
[30] T. Seiyama, A. Kato, K. Fujiishi, M. Nagatani, Anal. Chem., 34, (1962) 1502.
[31] N. Taguchi, Gas detecting device, U.S. Patent No.3631436, (1971).
[32] S. R. Morrison, Semiconductor gas sensors, Sensorsand Actuators, 2 (1982) 329-341.
[33] G. Heiland, Homogeneous semiconducting gas sensors, Sensors and Actuators, 2 (1982) 343-361.
[34] N. Yamazoe and T. Seiyama, Sensing mechanism of oxide semiconductor gas sensors, Proc. 3rd Int.Co@ Solid-State Sensors and Actuators (Transducers'85), Philadelphia, PA, U.S.A., June 7-l I, 1985,pp. 376-379.
[35] P. Ciureanu, S. Middelhoek, Thin Film Resistive Sensors, (IOP Publishing, Bristol, UK, 1992).
[36] M.J. Madou, S.R. Morrison, Chemical Sensing with Solid State Devices, (Academic Press, Inc., 1989).

[37] N. Barsan and U. Weimar, J. Electrocer. 7, 143 (2001).
[38] D.J. Shaw, S. Middelhoek, Introduction to Colloid and Surface Chemistry, (Butterworth-Heinemann, Oxford, UK, 1966).
[39] S.L.M. Schroeder, M. Gottfried, (2002) 1-22.
[40] N. Yamazoe, Sens. Actuators B 5, 7 (1991).
[41] Korotcenkov, G. Metal Oxides for Solid-State Gas Sensors: What Determines Our Choice? Mater. Sci. Eng. B 2007, 139, 1-23.
[42] Haridas, D.; Gupta, V.; Sreenivas, K. Enhanced Catalytic Activity of Nanoscale Platinum Islands
[43]Loaded onto SnO2 Thin Film for Sensitive LPG Gas Sensors. Bull. Mater. Sci. 2008, 31, 397-400.
[44] D. Kohl, Sens. Act. B 1990, 1, 158.
[45] P. Criindler, "Chemical Sensors: An Introduction for Scientists and Kngineers." Springer, Berlin, 2007.
[46] A. Diéguez, Ph. D. Thesis, Universitat de Barcelona, 1999.
[47] J.F. McAleer, P.T. Moseley, J.O.W. Norris, D.E. Williams, J. Chem. Soc. Far. Trans.1 1987, 83, 1323
[48] N. Barsan, U. Weimar, J. Electroceram., 7, (2001) 143-167.
[49] C. O. Park and S. A. Akbar, J. Mater. Sci. 38, 4611 (2003).
[50] Shimizu, Y.; Devi, G.S.; Hyodo, T.; Egashira, M.; Synthesis of Mesoporous TiO2-Based Powders and Their Gas-Sensing Properties. Sens. Actuat. B 2002, 87, 122-129.
[51] Cabot, A.; Arbiol, J.; Cornet, A.; Morante, J.R.; Chen, F.; Liu, M. Mesoporous Catalytic Filters for Semiconductor Gas Sensors. Thin Solid Films 2003, 436, 64-69.
[52] S. Gherardi, Master thesis, (2001).
[53] N. Barsan, D. Koziej, U. Weimar, Sens. Actuators, B, 121, (2007) 18.
[54] X. Du, Y. Du, S. M. George, J. Phys. Chem. A, 112, (2008) 9211-9219.
[55] M.J. Madou, S.R. Morrison, Chemical Sensing with Solid State Devices, (Academic Press, Inc., 1989).
[56] N. Barsan, U. Weimar, J. Electroceram., 7, (2001) 143-167.
[57] A. Gurlo, R. Riedel, Angew. Chem. Int. Ed., 46, (2007) 3826.
[58] G.S. Henshaw, R. Ridley, D.E. Williams, J. Chem. Soc. Far. Trans. 1996, 92(18), 3411.
[59] R. Pestman, R.M. Koster, J.A.Z. Pieterse, V. Ponec, J. Catal. 1997, 168, 255.
[60] I. Kocemba, T. Paryjczak, Thin Solid Films 1996, 272, 15.
[61] J.N. Carstens, S.C. Su, A.T. Bell, J. Catal. 1998, 176, 136.
[62] E. Garbowski, C. Feumi-Jantou, N. Mouaddib, M. Primet, Appl. Catal. A 1994, 109, 277.
[63] Endres, H.E.; Göttler, W.; Hartinger, R.; Drost, S.; Hellmich, W.; Müller, G.; Braunmühl, C.B.; Krenkow, A.; Perego, C.; Sberveglieri, G. A thin-film SnO2 sensor system for simultaneous detection of CO and NO2 with neural signal evaluation. Sens. Actuators B 1996, 36, 353–357.
[64] Hoefer, U.; Böttner, H.; Felske, A.; Kühner, G.; Steiner, K.; Sulz, G. Thin-film SnO2 sensor arrays controlled by variation of contact potential-A suitable tool for chemometric gas mixture analysis in the TLV range. Sens. Actuators B 1997, 44, 429–433.
[65] Fraiwan, L.; Lweesy, K.; Bani-Salma, A.; Mani, N. A wireless home safety gas leakage detection system. In Proceedings of the 1st Middle East Conference on Biomedical Engineering (MECBME), Sharjah, United Arab Emirates, 21–24 February 2011; pp. 11–14.
[66] Jarmo, K.; Jani, M.; Niina, H.; Teemu, K.; Géza, T.; Maria, S.; Andrey, S.; Jyri-Pekka, M.; Heli, J.; Krisztián, K. Gas sensors based on anodic tungsten oxide. Sens. Actuators B 2011, 153, 293–300.
[67] Wisitsoraat, A.; Tuantranont, A.; Comini, E.; Sberveglieri, G. Gas sensing properties of CNT-SnO2 nanocomposite thin film prepared by E-beam evaporation. In Proceedings of 2007 IEEE Sensors, Atlanta, GA, USA, 28–31 October 2007; pp. 550–553.
[68] Hallil, H.; Chebila, F.; Menini, P.; Pons, P.; Aubert, H. Feasibility of wireless gas detection with an FMCW RADAR interrogation of passive RF gas sensor. In Proceedings of 2010 IEEE Sensors, Kona, HI, USA, 1–4 November 2010; pp. 759–762.
[69] Gas Detector: Analog Dialogue: Analog Devices, 2015.
[70] Influence of Water Vapour on Nanocrystalline SnO_2 to Monitor CO and CH_4, J. Kappler, N. Bârsan, U. Weimar and W. Göpel, Conf.Proc.Eurosensors XI, 1997, 1177-1180, Warschau (P), 83-908335-0-6.
[71] Robert T. Morrison, Robert N. Boyd, Lehrbuch der organischen Chemie, 3, Auflage, VCH, Weinheim 1986, 129.
[72] Jae Chang Kim, Hee Kwon Jun, Jeung-Soo Huh, Duk Dong Lee, Sensors and Actuators B: Chemical, Volume 45, Issue 3, 15 December 1997, Pages 271–277.

CHAPTER -2

BACKGROUND

Material properties and state of art

In this chapter, we present a resume of physical properties of SnO_2 and the different dopants used in our work and the criteria for choosing these dopants. Also we will discuss about the sensing reactions of the carbon monoxide and propane with the SnO_2 surface. The advantages of the synthesis techniques and the doping methods utilized are also presented. Finally, a survey about the SnO_2 material in gas sensing applications is demonstrated.

2.1. Material properties of SnO_2

Tin oxide (SnO_2) is a multifaceted material having diverse uses in optoelectronic technology [1], consequently leading to almost inexhaustible literature [2]. SnO_2 have also been proposed as an alternative anode material with high energy densities and stable capacity relation in lithium-ion batteries [3-6]. Tin oxide is a native n- type wide band gap semiconductor (Eg = 3.6 eV) and its electrical properties strongly depend on its stoichiometry (Sn: O), on the nature and amount of impurities or dopants present, and on its size as well as shape of nanostructures [7-9]. SnO_2 is invariably anion (oxygen) deficient; and oxygen vacancies are mainly responsible for making available free electrons for the conduction process [10], which makes SnO_2 adequate for gas sensing applications.

Tin oxide has also been one of the first considered and still has shown very high sensitivities towards many different reducing gases, such as H_2, CO, C_3H_8, H_2S, other hydrocarbons, and alcohols [11, 12]. As we mentioned in section 1.9, thin or thick film gas sensors produce compact structures, which can limit the sensor sensitivity [13, 14]. Its sensitivity can be further improved by increasing the surface area. Therefore, we have utilized SnO_2 pellets in our work, which are comprised of porous nano structured SnO_2 powders with a high surface/volume ratio, and a small crystallite size. Pellets with these characteristics will lead to easy gas transport and interesting electrical properties [15-21].

2.1.1. Crystalline structure of SnO_2

The structure of tin oxide is shown in Fig. 2.1. Tin oxide is formed in the structure of rutile, the spatial group being P4/*mnm*. The unit cell is tetragonal, it consists of six atoms – two tin and four oxygen atoms. The lattice parameters a, c and intrinsic parameter *u*. The atoms of Sn are located in the bcc-positions (0, 0, 0) and (1/2, 1/2, 1/2) and are surrounded by oxygen atoms being in the positions ± (*u*, *u*, 0) and ± (1/2+*u*, 1/2–*u*, 1/2) to form a distorted tetrahedron. The optimized cell parameters reported are as follows: $a=b= 4.738$Å, $c= 3.188$Å and $u = 0.30756$ [22-24]. In the bulk all Sn atoms are six fold coordinated to threefold coordinate oxygen atoms. SnO_2 is an anisotropic polar crystal, [25, 26] whose unit cell contain 6 atoms, 2 tins and 4 oxygen. Each tin atom is at the center of six oxygen atoms placed approximately at the corners of a regular slightly deformed octahedron, and three tin atoms approximately at the corners of an equilateral triangle surround every oxygen atom [27, 28]. If tin oxide was completely stoichiometric, it would be an insulator. However, in practice, prepared tin oxide powders

contain a significant number of oxygen vacancies, making electrons available for conduction [29]. The mobility of the conduction electrons reported for pure SnO_2 is around 160 cm^2/Vs [30].

Tin oxide single crystals expose mainly {110} and {101} faces [31]. The (110) and (101) SnO_2 planes are the most favorable planes for gas sensing applications, because of the presence of dangling bonds at the surfaces. Consequently, these two faces are the most studied single crystal surfaces and we address their properties in the following.

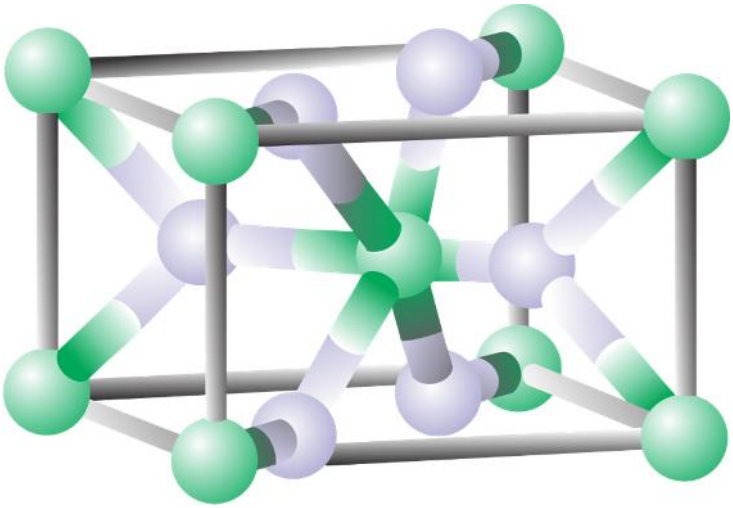

Fig. 2.1. Unit cell of SnO_2, green atoms corresponds to Sn atoms and the white atoms corresponds to oxygen.

2.1.2. The (110) surface

This ideal surface is nonpolar and exposes five-coordinate Sn^{4+} cations in the second atomic layer (one coordination vacancy) [32]. Heating the stoichiometric SnO_2 surface in vacuum to temperatures up to 450 ^0C removes only the top-layer, bridging oxygen anions. The coordination of the newly exposed tin cations associated with the "bridging oxygen vacancies" drops from six to four, with an apparent change in oxidation state from Sn^{4+} to Sn^{2+} [33-35]. Further heating to temperatures above 450 ^0C removes some lattice or in-plane oxygen anions from what was initially the second atomic layer. Oxidation process prior to the high-temperature (e.g., 676 ^0C) annealing produces a less-defective surface with an estimated 20% in-plane oxygen vacancies [36, 37].

Fig. 2.2 shows a ball-and-stick model of the SnO_2 crystal structure in (110) plane. Complex surface reconstructions are being observed on this surface. The (110) surface is likely to behave in a similar fashion and easily loose surface oxygen, however, the different atomic coordination of the (101) surface allows for an adaptation of a reduced surface composition

without restructuring of the surface atoms. The easy loss of surface oxygen can be understood by the dual valency of Sn that allows the transformation of surface tin from Sn^{4+} to a Sn^{2+} valence state if oxygen is removed. As long no reliable structural model exists any further surface science studies on this structure seem futile.

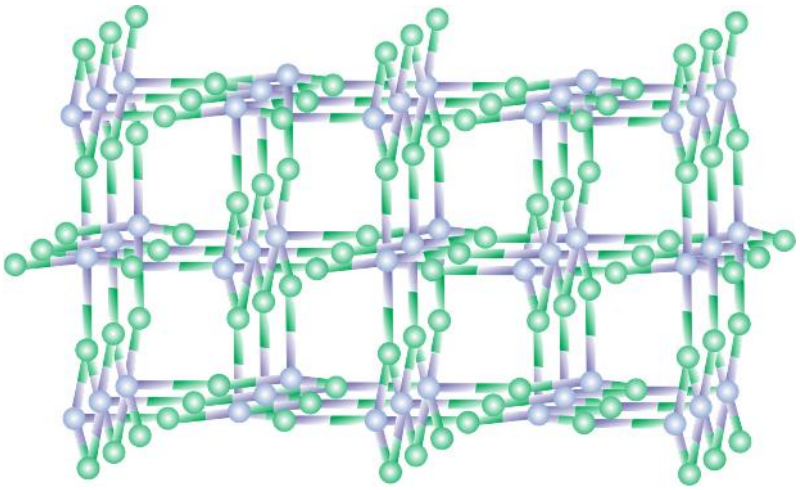

Fig. 2.2. Ball-and-stick model of a cross-sectional view through a SnO_2 crystal with a (101) orientation. The (110) surface is at the top. Green atoms corresponds to Sn atoms and the white atoms corresponds to oxygen.

2.1.3. The (101) surface

Apart from single crystal termination in an equilibrium crystal shape, it is also the dominant termination for SnO_2 nano-belts [38], and is the face that grows epitaxially on r-cut alumina substrates [39, 40]. In many applications such as low-emissive coatings and solar cells, the tin oxide layers are chemically doped, for example, by fluorine or antimony, to further enhance the conductivity [41]. The dual valence of tin allows the formation of surfaces with a Sn^{2+} or a Sn^{4+} termination. The conversion from one Sn-charge state to the other is particularly easily accomplished on the (101) surface because of the atomic stacking in this crystallographic direction.

Fig. 2.3 shows a ball-and stick model of the SnO_2 crystal structure in (101) orientation. It can be seen that the atomic stacking along the (101) direction can be described as O-Sn-O tri-layer. A stoichiometric sample will terminate in an oxygen layer and thus the surface Sn will retain its Sn^{4+} bulk valency. However, it can be seen from Fig. 2.3 (b) that removal of the surface oxygen layer results in a Sn-O surface, where the surface Sn needs to adopt a Sn^{2+} charge state. Thus by simple addition or removal of the surface oxygen layer the surface Sn can convert from Sn^{4+} to Sn^{2+} and vice versa. For the (110) surface the sample cannot easily convert from one Sn valency to another and this may be one reason for the complex surface reconstructions observed [42]. On the (101) surface no reconstructions are necessary to go from a Sn^{4+} to a Sn^{2+} surface.

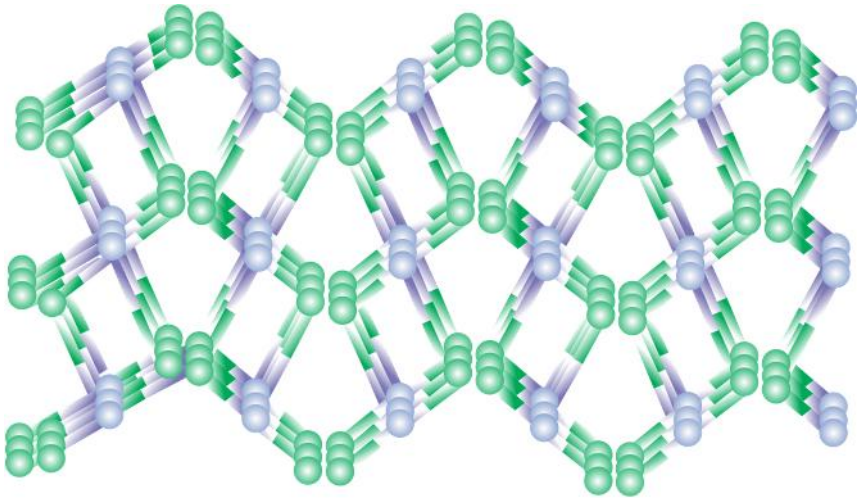

Fig. 2.3. Ball-and-stick model of a cross-sectional view through a SnO_2 crystal with a (101) orientation. Green atoms corresponds to Sn atoms and the white atoms corresponds to oxygen.

2.1.4. Advantages of tin oxide as gas sensor

One of the main advantage of tin oxide is the ease with which stoichiometry can be created in the material. A fine control over the defects gives rise to the desired chemical and physical properties, which can be used for gas sensing purposes. Moreover, sensitivity and cross selectivity profiles can also be tailored to the desired need of application using innovative techniques. In addition, sensor arrays of tin oxide can also be patterned; similarly, the flexibility of synthesizing tin oxide through various precursors can also be used for making automated sensor arrays by combinatorial method [43].

Apart from this, it is easy to synthesize tin oxide powders with ultra-fine grain size. As the sensor performance depends upon the micro-structure of sensing material and by consequence of the technology used to produce the material, the performance can be improved dramatically [44]. Tin oxide sensors are known to be highly sensitive to several reducing gases in their trace levels as compared to the other semiconductor materials, further, these sensors can be easily miniaturized with good mechanical strength [45]. In addition, due to SnO_2 presents a direct band gap, transitions are faster, which couple with the high mobility of electrons, resulting in fast response to small concentrations of gas.

2.2. Interaction of gases with SnO_2 pellet surface

This section explains the interaction of pellet with CO and C_3H_8 gases in detail. The importance and the reasons for the general gas leaks and utilization of CO and C_3H_8 were

discussed previously in section 1.3. The production and risk factors were also mentioned previously in section 1.10.

2.2.1. Carbon monoxide (CO)

Carbon monoxide is considered to react with pre-adsorbed or surface lattice oxygen [47]. IR studies identified that CO-related species i.e. unidentate and bidentate carbonate are produced between 150 ^{0}C and 400 ^{0}C and carboxylate between 250 ^{0}C and 400 ^{0}C [48]. Also the formation of CO_2 as a reaction product between 200 ^{0}C and 400 ^{0}C was identified by FTIR [49]. When CO reacts with the pre-adsorbed oxygen, it releases electrons into the conduction band (Fig. 2.4 a) as shown in equation 2.1. CO can adsorb on the tin oxide surface (without consumption and reaction to CO_2) and cause an electrical effect. The adsorption of CO on the lattice oxygen is shown in Fig. 2.4b.

$$CO + O^- \Longrightarrow CO_2 + e^- \qquad (2.1)$$

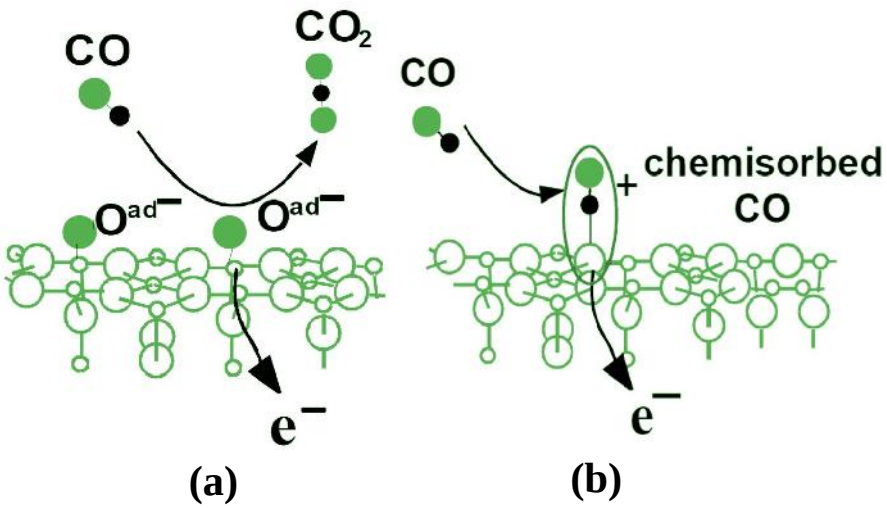

Fig. 2.4. CO interaction (a) with pre-adsorbed oxygen and (b) with surface lattice oxygen.

The reaction of the CO with the tin oxide surface for different cases is shown in Fig. 2.5. In the absence of oxygen and water (and also in the presence of very small amounts thereof), CO can adsorb at the surface of the sensitive layer and act as an electron donor (Fig. 2.5). The release of an electron does not result in a localized charge, but the electron is rather inserted into the conduction band of the material, thus increasing the conductivity of the material [50]. The molecular configuration of the adsorption, i.e. bonding of the carbon or the oxygen atom to a tin or oxygen of the surface could not be clarified up to now, but is subject to investigation.

When small amounts of oxygen are added (Fig. 2.5), the CO can either be directly chemisorbed or it can react with ionosorbed oxygen, also resulting in an electrical effect (i.e.

sensor signal) through the insertion of electrons (originating from the ionosorbed oxygen) into the conduction band. With larger amounts of oxygen available, this direct chemisorption seems to be hindered. Thus, at ambient oxygen concentration, the reaction with ionosorbed oxygen is the only possible reaction.

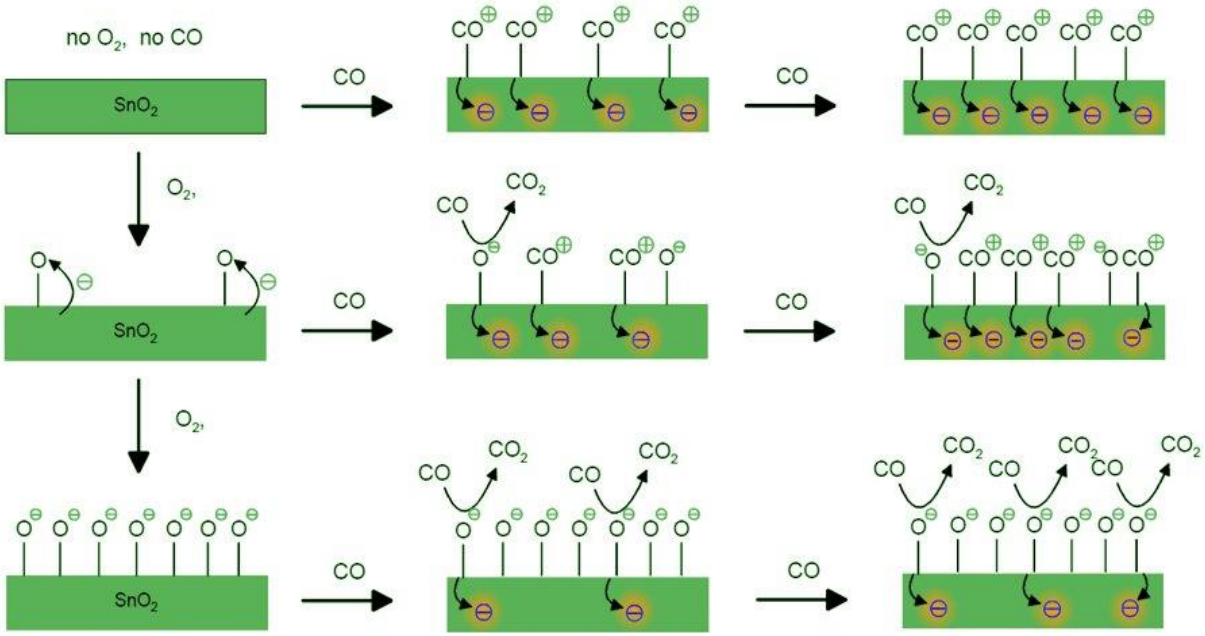

Fig. 2.5. Mechanism for the interaction of CO with SnO_2 layer.

2.2.2. Propane (C_3H_8)

For propane also the gas sensing explanation is similar as in the case of CO. In the absence of oxygen and water (or presence of very small amounts), propane can adsorb on the tin oxide surface (without consumption and reaction to CO_2) and cause an electrical effect [51]. As SnO_2 is known to be a weak basic oxide [52] it is assumed that C_3H_8 dissociates to a propyl group and a hydrogen atom on the SnO_2 surface as shown in equation 2.2.

$$C_3H_{8,\,gas} \Longrightarrow C_3H_{7,\,ads} + H_{\,ads} \qquad (2.2)$$

$H_{\,ads}$ acts as a donor, in combination with lattice oxygen or it is possible that a removal of lattice oxygen takes place at higher temperatures leaving behind an oxygen vacancy [53]. The adsorption of Propane on the lattice oxygen is shown in Fig. 2.6. Fig. 2.7 shows a proposed mechanism for the detection of propane. Without oxygen, propane is only dissociatively adsorbed on the surface. When small amounts of oxygen are added, propane can alternatively be adsorbed or can be oxidized by adsorbed oxygen ions, thus resulting in a higher electrical

effect. When large amounts of oxygen are added, propane can only react with adsorbed oxygen, the adsorption is hindered, possibly through blocking of adsorption sites. This results in an electrical effect, which is smaller than for small amounts of oxygen.

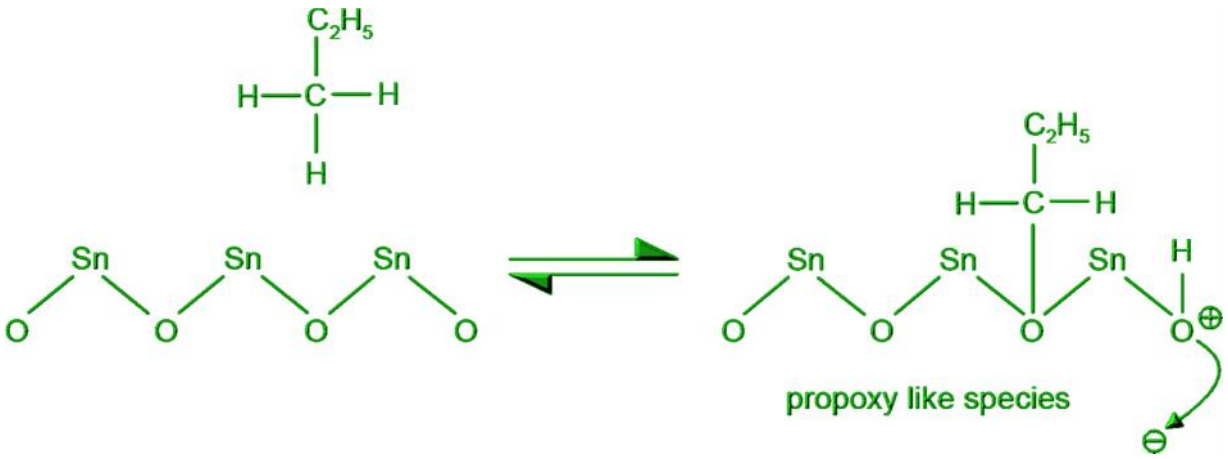

Fig. 2.6. Proposed adsorption reaction in the absence of pre-adsorbed oxygen.

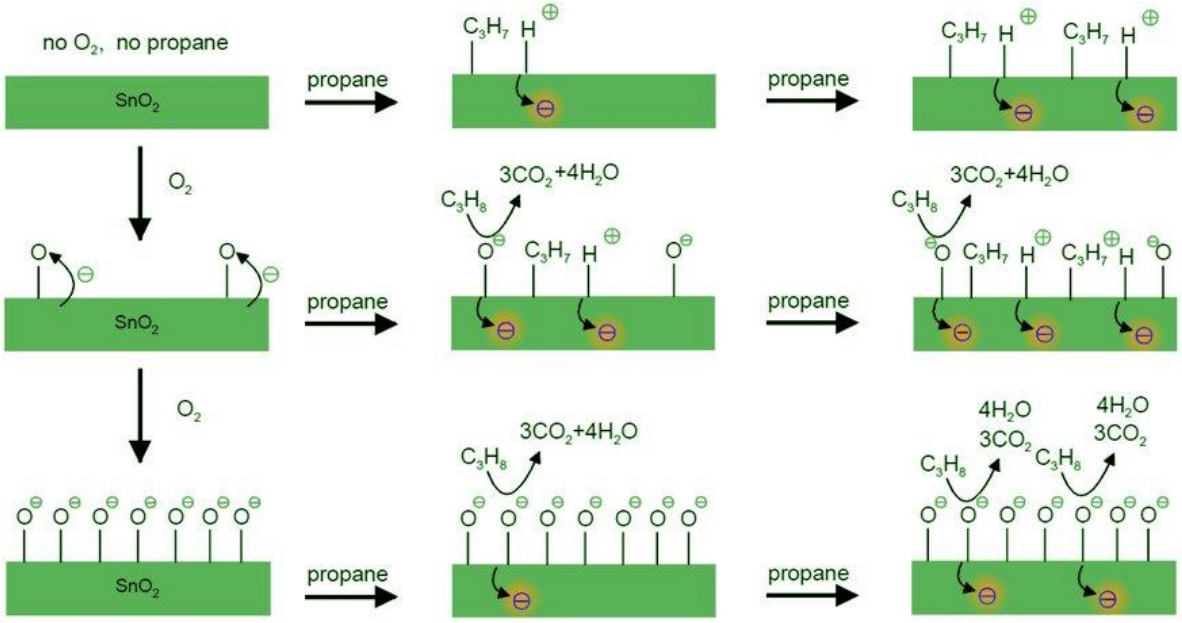

Fig. 2.7. Mechanism for the interaction of C_3H_8 with SnO_2 layer.

2.3. Homogeneous precipitation

Commercially available SnO_2 gas sensors mainly are in the form of thick films, thin films, or pellets. Apart from problems like power consumption, response time and fragility, pellets are more viable for gas sensors than films. High sensitivity, porosity, surface area, less contamination and no substrate effects are some of the major advantages of the pellets over films. The advantages of pellets over thin films and the Metal oxide chemical sensors were discussed in chapter 1. Also the advantages of choosing SnO_2 as gas sensor were explained in section 2.1.4.

Different synthesis methods are reported for the preparation of SnO_2 powders, for example, flame spray [54], sol-gel [55], micro wave radiation [56], and conventional homogenous precipitation [57], among others. Homogenous precipitation employing urea as precipitant agent and conventional precipitation using ammonia as a precipitation agent have gained more importance in synthesizing novel phases and fine particulate materials.

Precipitation, formation of a separable solid substance from a solution, either by converting the substance into an insoluble form or by changing the composition of the solvent to diminish the solubility of the substance in it. The distinction between precipitation and crystallization lies largely in whether emphasis is placed on the process by which the solubility is reduced or on that by which the structure of the solid substance becomes organized. All precipitation analysis share two important attributes. First, the precipitate must be of low solubility, of high purity, and of known composition if its mass is to accurately reflect the analyte's mass. Second, the precipitate must be easy to separate from the reaction mixture.

Size matters when it comes to forming a precipitate. Larger particles are easier to filter, and, as noted earlier, a smaller surface area means there is less opportunity for surface adsorbates (After precipitation is complete the surface continues to attract ions from solution, these are called as surface adsorbates) to form. By carefully controlling the reaction conditions we can significantly increase a precipitate's average particle size. Precipitation consists of two distinct events: nucleation, the initial formation of smaller stable particles of precipitate, and particle growth. Larger particles form when the rate of particle growth exceeds the rate of nucleation. Understanding the conditions favoring particle growth is important when designing a precipitation method of analysis [58].

Supersaturation is a state of a solution that contains more of the dissolved material than could be dissolved by the solvent under normal circumstances. We define a solute's relative supersaturation, *RSS*, RSS= (Q-S)/S, whereas Q is the solute's actual concentration and *S* is the solute's concentration at equilibrium [59]. A solution with a large *RSS*, has a high rate of nucleation, producing a precipitate with many small particles. When the *RSS* is small, precipitation is more likely to occur by particle growth than by nucleation.

For gas sensing applications, it is favorable to obtain small particle size. But to form small particles, the solution RSS will increase, which in turn consumes lot of time. Also as the precipitate forms the solution RSS becomes less which increases the particle size in general or conventional precipitation. One solution above problem is to generate the precipitant in situ as the product of a slow chemical reaction. This maintains the *RSS* at an effectively constant level. Because the precipitate forms under conditions of low *RSS*, initial nucleation produces a small number of particles. As additional precipitant forms, particle growth supersedes nucleation, resulting in precipitate particles. This process is called homogeneous precipitation [60].The particle size obtained in this process is lower compared to the particle size formed in conventional precipitation.

In homogeneous precipitation, we mix the analyte and the precipitant under conditions where precipitation does not occur, and then increase or decrease the pH by chemically generating OH^- or H_3O^+. For example, the hydrolysis of urea is a source of OH^-.

Hydrolysis of urea is temperature dependent (Urea decomposes around 80-90^{0}C). We can use temperature to control the rate of hydrolysis and the rate of precipitate formation. Precipitates of SnO_2, for example, have been produced by this method. After dissolving the sample containing Sn^{+2}, is added with solution containing urea. Because the solution is acidic, a precipitate does not form. The solution is heated to approximately 80-90^{0}C and urea starts decomposing. After several minutes, a precipitate of SnO_2 begins to form. The time taken for precipitation with respect to different molarities was all mentioned in experimental section (chapter 3).

In case of conventional precipitation, the precipitant is generated by a chemical reaction. For example, the same Sn^{2+} is precipitated conventionally as SnO_2 by using Ammonia, NH_3, by forming ammonium, NH_4^+ and Cl^-. The direct addition of Ammonia leads to rapid precipitation and the formation of larger particles, the precipitate remains less settled than the precipitate prepared homogeneously.

A homogeneous precipitation produces smaller particles of precipitate that are relatively free from impurities. These advantages, however, are offset by requiring more time to produce the precipitate and a tendency for the precipitate to deposit as a thin film on the container's walls. The latter problem is particularly severe for hydroxide precipitates generated using urea. As reported by Xu et.al. , [61], the average particle size obtained by a conventional homogeneous precipitation are around 150 and 100 nm respectively. For gas sensing applications it is essential to reduce the particle size at least to around 20-30 nm. Therefore in our work we have utilized physical technique, ball milling, to reduce the particle size.

2.4. Ball milling

Ball milling is a commonly used method of producing fine powder in many industries. The tumbling mill with centrifugal and planetary action has recently been used to prepare fine powder from a variety of materials such as minerals, ores, alloys, chemicals, glass, ceramics, and plant materials. More noticeably, the planetary ball milling can reduce particles to fine powders based on a mechanical energy transfer, or impact and friction forces through high hardness ball media [62, 63]. However, its energy efficiency is low, and the power cost is high. Advantages and disadvantages of ball milling are as follows:

2.4.1. Advantages

- Powerful and quick grinding down to nano range
- Reproducible results due to energy and speed control
- Suitable for long-term trials
- High production capacity and crushing ratio
- Uniform particle size
- Simple structure and easy to operate

2.4.2. Disadvantages

- Main advantage of ball milling in synthesis of nano powders is agglomeration of the particles due to the heat produced in the jar.
- Bulky size, running a strong vibration and noise and there must be a solid foundation
- Low efficiency and energy consumption is relatively large

In this research, the improvement of gas sensing properties of SnO_2, due to ball milling of the precipitated powders is investigated. The main reasons for using ball milling are, easy to reduce the particle size and also to obtain narrow and homogeneous distribution of particle size. Experimental conditions and the mechanics of ball milling equipment used are mentioned in chapter 3. Also, the effect of ball milling parameters on the particle size and also on the gas sensing applications are discussed in chapter 4.

2.5. Doping methods

Catalysts/ additives provide another promising direction in the development of gas sensors due to the possibility of processing materials with unique physical–chemical properties [64, 65]. The doping of semiconductor by various additives is one of the main methods for improving gas sensitivity and selectivity, reducing the operating temperature, enhancing the response rate, etc. Surface-related factors, such as optical, electronic, catalytic, mechanical, and chemical properties, are the most important and easily influenced by doping in gas sensor

applications. Doping can be made by using different impurities such as metals, nonmetals and metalloids. Consequences of semiconductor doping for their parameters are shown in Fig. 2.8.

Methods of catalyst preparation are very diverse and each catalyst may be produced via different routes. Preparation usually involves several successive steps. Many supported metal and oxide catalysts (surface doping) are prepared by the succession of impregnation, drying, calcination and activation; other catalysts (bulk doping) are prepared by precipitation, crystallization, washing, ion exchange, and drying.

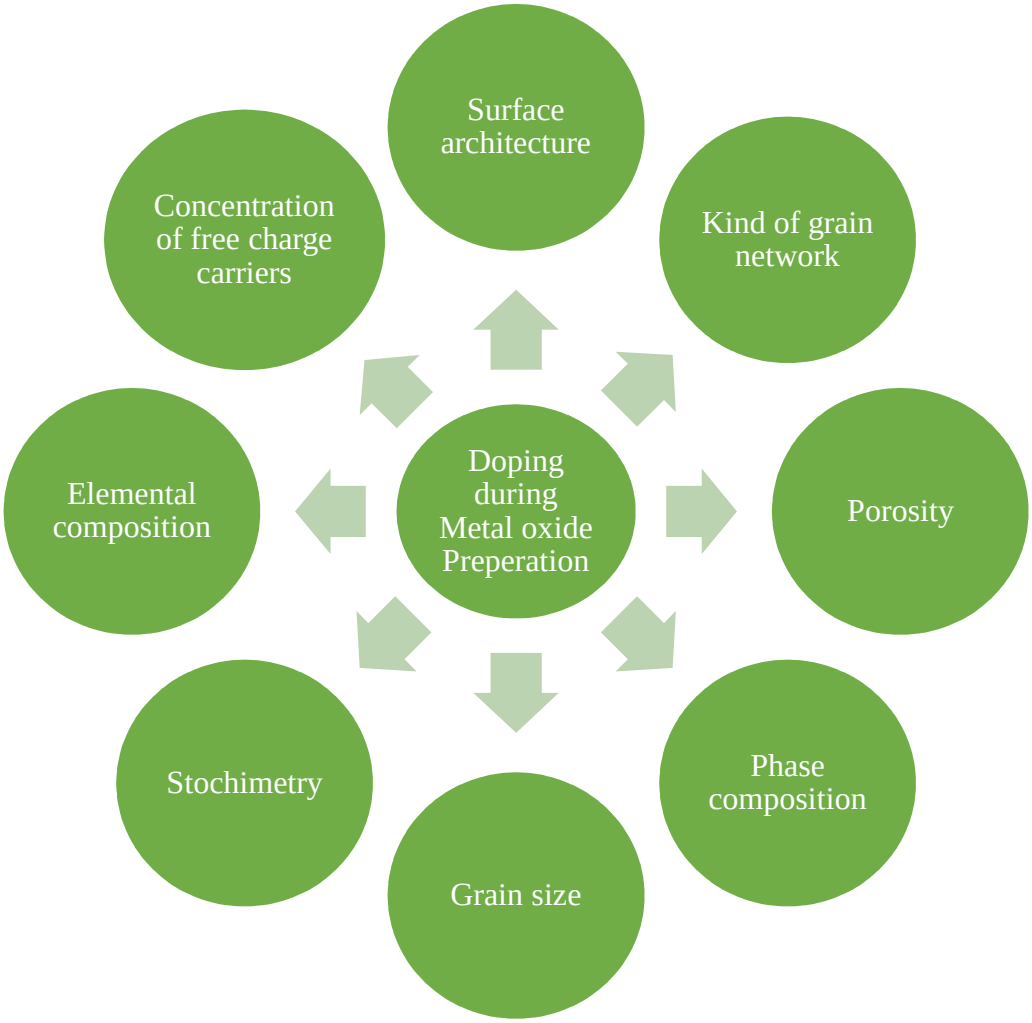

Fig. 2.8. Parameters subject to modification as a result of semiconductor doping.

Three fundamental stages of catalyst preparation may be distinguished:

1. Preparation of the primary solid (or first precursory solid) associating all the useful components (e.g., impregnation or precipitation and crystallization).

2. Processing of that primary solid to obtain the catalyst precursor, for example by heat treatment.
3. Activation of the precursor to give the active catalyst: reduction to metal. Activation may take place spontaneously at the beginning of the catalytic reaction too.

One method which causes bulk doping (D_b) is precipitation method. In section 2.3, the conventional and homogeneous precipitation process were explained. In all precipitations with catalysts, it is essential to carefully control all the details of the process including:

1. The order and rate of addition of catalyst into the solution.
2. The mixing procedure
3. The pH variation due to the catalysts addition.

Active catalytic forms can be obtained conventionally by cation-exchange. Care should be taken to avoid chemical modifications induced by a too low or too high pH of the exchange solution, which can lead to the formation of lattice defects. Protonic sites are generated by ammonium-exchange (preferably at buffered and slightly basic pH, 7-9) followed by calcination at 300 – 500 ^{0}C. Metals can be introduced via ion-exchange and subsequent reduction or via adsorption of neutral soluble or volatile species (for example carbonyls).

When a semiconductor is doped either with noble metals or with transition metals, depending on the method of doping, the metals will be located either in the bulk or surface. In case of bulk doping (D_b), irrespective of transition or noble metals, the dopants are added during the synthesis of the MOS, in which, the dopants are considered to be located in the substitutional or interstitial positions of the semiconductor. The stress and strain produced due to the structural changes will increase the oxygen adsorption, which in turn increases the gas sensitivity [64].

A method which causes surface doping (D_s) is impregnation method. Impregnation consists in contacting a solid with a liquid containing the components to be deposited on the surface. During impregnation many different processes take place with different rates. The type of product obtained depends on (i) the nature of both reactants (the liquid and the solid surface), and (ii) the reaction conditions. In impregnation process the following important facts should be noted:

1. Selective adsorption of species (charged or not) by Coulomb force, van der Waals forces or H-bonds.
2. Ion exchange between the charged surface and the electrolyte
3. Polymerization / de-polymerization of the species (molecules, ions) attached to the surface
4. Partial dissolution of the surface of the solid.
5. The properties of the liquid in the pores are different from those measured in the bulk
6. Equilibrium between liquid and solid is slow to establish and even distribution of attached species inside the pores is not easy to attain

In case of surface doping (Ds), (i) for noble metals, the metal oxide acts as a gas sensing matrix and the noble metals acts as a catalyst by residing on the surface of the metal oxide, in the form of dispersed clusters, and (ii) for transition metals, metal oxide acts as a gas sensing matrix and the transition metal may reside in the form of cluster or act as structure modifier. In both the cases, an increase of the surface reactivity is possible [65].

In a precipitation process, surface adsorption of excess lattice ions takes place. This adsorption makes the precipitate's particles with a net positive or a net negative surface charge. Electrostatic repulsion between the particles prevents them from coagulating into larger particles. We can induce coagulation in three ways: by decreasing the number of chemically adsorbed ions, by increasing the concentration of inert ions, or by heating the solution.

In case of conventional precipitation, if the amount ammonia added is increased then there is a possibility of increase in the adsorbed ions on the surface which makes the particles to coagulate. In case of homogeneous precipitation, a temperature around 80 ^{0}C is used to decompose urea, which may also coagulate the particles. Also mixing of dopant solution during the precipitation (in case of bulk doping), the increase the concentration of the inert ions, which also makes the particles obtained to coagulate. The methods of coagulation of SnO_2 particles is shown in Fig. 2.9. This formation of necks is because, the temperature, the catalyst, or the ammonia makes the particles electrically neutral which makes particles to coagulate during precipitation.

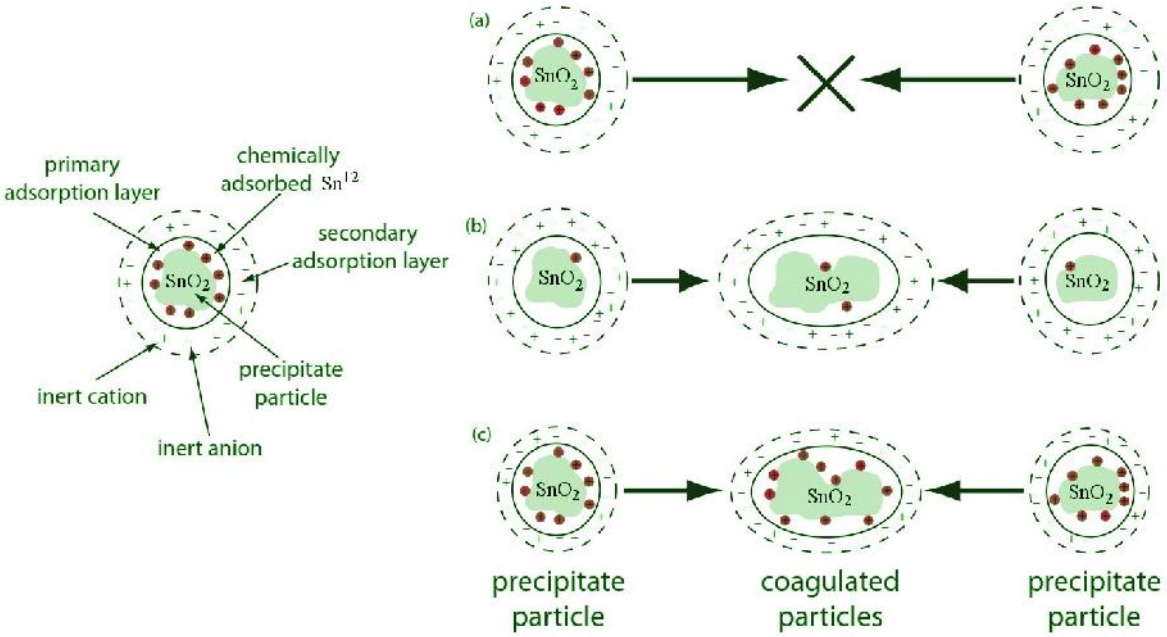

Fig. 2.9. Parameters subject to modification as a result of semiconductor doping.

In our work we have utilized chemical doping by mixing dopants during precipitation and also impregnation by wetting the powders, to observe the effect of dopants on the gas sensing properties. The detailed doping procedure with the all conditions are mentioned in chapter 3 and the corresponding structural, morphological and sensing characteristics were discussed in detail in chapter 4.

2.5.1. Criteria for choosing dopants Cu, Pt and Pd

The major catalytically active doping additives are noble metals (Pd, Pt, Au, Ag, Rh, etc.), and transition metals (Fe, Co, Cu, etc.). In general noble metals serve as "catalysts" while transition metals serve as "accelerators" of various processes [66-68]. Among all the noble metals additives, Pt and Pd are the most used due to their work function values (~5.8 and ~5.4eV, respectively), and chemical inertness [69-72].

The most important effects of the noble metal addition are the increase of the maximum sensitivity and lowering the temperature of maximum sensitivity. In this respect, Cu is the most used transition metal for doping due to two main reasons, primarily, in case of bulk doping, copper has the comparable radius as tin, radii of Sn^{4+} and Cu^{2+} are around 0.71 and 0.72 A°, respectively [73], then, it is easier to replace the tin with copper and secondarily, in case of surface doping, during the gas sensing process, Cu changes its phase to Cu_2O, this phase transformation or two phase system increases the gas response [74]. It should be noted that the effect of each doping material is complex and is not well studied. A surface catalyst may increase the concentration of reactants at the semiconductor surface or lower the activation energy for the reaction, or it may affect both parameters.

2.6. State of art of SnO_2 sensors

So far there are many different methods employed by various authors to synthesis SnO_2 powders for gas sensing applications [3, 4, 7, 14, and 20]. Also many reviews have been published about tin oxide sensors, for example, T.A. Miller [75] has resumed in his review numerous methods used to prepare pure and doped SnO_2 powders, with their corresponding particles sizes and sensitivities obtained. The important characteristics of SnO_2 powders synthesized by different authors most recently, including the reactant precursor materials used, the average SnO_2 crystallite size, and their corresponding sensitivities are provided in Table. 2.1. All the parameters mentioned in the Table. 2.1, were published very recently in 2014-15.

As we have explained so far in various sections in chapters 1 and 2 regarding sensitivity and their influencing parameters, it is important to obtain higher sensitivities while controlling other parameters like cost of the equipment and sensor operation temperature, which should be low. Also the having smaller crystallite size is necessary in order increase the surface to volume

ratio, which subsequently increases the sensitivity. From the Table 2.1 we can observe that, the minimum crystallite size obtained was around 3.5nm by utilizing chemical synthesis methods. Also the maximum sensitivity obtained for CO was around 100 and H_2S was around 357. The minimum operation temperature obtained was around 100^0C.

SnO_2 synthesis method	**SnO_2 precursor**	**Crystallite size (nm)**	**Sensitivity (Resistance ration Ra/ Rg at specified operating temperature and mole fraction of target gas)**	**Reference**
Vapor−liquid−solid	Sn Powder	~75-90	~ 80 at 300 ^{0}C and at 10 ppm of CO	[76]
Hydrothermal process	$SnCl_2 \cdot 2H_2O$	~10	~ 78 at 220 ^{0}C and at 100 ppm of acetone	[77]
Hydrolysis and Precipitation	$SnCl_4.5H_2O$	~15	~80 at 350 ^{0}C and at 600 ppm of CO	[78]
Chemical spray pyrolysis	$SnCl_4.5H_2O$	~10	~132 at 225 ^{0}C and at 400 ppm of NO_2	[79]
Precipitation	$SnCl_4.5H_2O$	~14	~100 at 350 ^{0}C and at 600 ppm of CO	[80]
One-step Solvothermal route	$SnCl_4.5H_2O$	~10	~22.69 at 260 ^{0}C and at 50 ppm of ethanol gas	[81]
Sol-Gel	$SnCl_4.5H_2O$	~8-20	~1.95 at 100 ^{0}C and at 5 ppm of CO	[82]
Hydrothermal synthesis	$SnCl_4.5H_2O$	~ 3.4 ± 0.8 nm	~357 at 100 ^{0}C and at 5 ppm of H_2S	[83]

Table. 2.1. Representative synthesis methods, material characteristics, and corresponding sensor sensitivity for SnO_2 systems.

In our work, we have utilized pellets and thick films manufactured with SnO_2 nano particles as gas sensors. Therefore we have traced our work by linking and relating our objectives with the state-of-art. We have employed chemical precipitation method and subsequent ball milling method for preparing anno particles in order to reduce the cost of the preparation process and also for obtaining smaller particle size. Also the precursor utilized is tin chloride pentahydrate ($SnCl_4.5H_2O$), which is also frequently used Sn source. We have introduced different dopants by using different methods for reducing the sensors operation temperature. The range of temperatures reported for gas sensors were around 100-350^{0}C, therefore we have also tested our sensors in the same temperature range. Another important factor we observe from literature is selectivity of the sensor, different operation temperatures results high sensitivities to different gases. Therefore we also employed CO and C_3H_8 in order to observe the selectivity. Finally, we aimed to obtain minimum particle size by utilizing chemical synthesis routes and obtain higher sensitivities as well as selectivity for CO and C_3H_8. The detailed experimental procedure and conditions were reported in the upcoming Chapter 3.

References

[1] J.Isidorsson, C.G.Granqvist, Solar Energy Mater.Solar Cells 44 (1996) 375.
[2] S.Samson, C.G.Fonstad, J.Appl.Phys.44 (1973) 4618.
[3] Y. S. He, J. C. Campbell, R. C. Murphy, M. F.Arendt and J. S. Swinnea, J. Mater. Res. 8, pp. 3131-3134, 1993.
[4] Y. Idota, T. Kubota, A. Matsufuji, Y. Maekawa, T. Miyasaka, "Structural Investigation of Tin Oxide Glasses C. Gejke, A. Matic, and ..." Science. 276, pp. 1395-1397, 1997.
[5] J. O. Besenhard, J. Yang, M. Winter, "Improvement in electrochemical properties of nano-tin-polyaniline ..." J. Power Sources. 90, pp. 70-72, 2000.
[6] I. A. Courtney, J. R. Dahn, "Optical Reflectance of Pure and Doped Tin Oxide: From Thin Films ....." J Elertcochem. Soc. 144, pp. 2045-2048, 1997.
[7] C.A. Ibarguen, A. Mosquera, R. Parra, M.S. Castro, "Synthesis of Tin Oxide (SnO2) by the Oxalate Route: Effects of ..." J.E. Rodriguez-Paez, Mater. Chem. Phys. 101, pp. 433-440, 2007.
[8] J. S. Lee, S. K. Sim, B. M., K. Cho, S. W. Kim, and S. Kim, "Surface characterization and functionalization of carbon nanofibers" J. Cryst. Growth. 267, pp. 145-147, 2004.
[9] G. Ansari, P. Boroojerdian, S. R. Sainkar, R. N. Karekar, R. C. Alyar, and S.K. Kulkarni, "High-performance temperature-selective SnO2:Cu-based sensor" Thin Solid Films. 295, pp. 271-276, 1997.
[10] Arijit Chowdhuri, P. Sharma, Vinay Gupta, K. Sreenivas and K.V. Rao "H2S gas sensing mechanism of SnO2 films with ultrathin CuO dotted islands," J. Appl. Phys., Vol. 92, No. 4 2002, pp. 2172 - 2180
[11] N. Yamazoe, G. Sakai, K. Shimanoe, Oxide semiconductor gas sensors, Catalysis Surveys from Asia, vol. 7, No. 1, 2003, 63-75.
[12] B. Esfandyarpour, S. Mohajerzadeh, A.A. Khodadadi, M.D. Robertson, Ultrahigh-Sensitive Tin-Oxide Microsensors for H2S Detection, IEEE Sensors Journal, August 2004, vol. 4, No. 4.
[13] Th. Becker, S. Ahlers, Chr. Bosch-v.Braunmuhl, G. Muller, O. Kiesewetter, Gas sensing properties of thin- and thick-film tin-oxide materials, Sensors and Actuators B, 77, 2001, 55-61.
[14] A. Tiburcio-Silver, A. Sánchez-Juárez, SnO_2: Ga thin films as oxygen gas sensor, Materials Science andEngineering B, 110, 2004, 268–271.
[15] M. Kojima, H. Kato, M. GAtto, "Studies on the structural and electrical properties of spray deposited ..." Philos.Mag. B.68, pp. 215-218, 1993.
[16] G.X. Wang, M.S. Park, D. Wexler, J. Chen, H.K. Liu, "Synthesis and characterization of one-di" Appl. Phys.Lett.19, pp. 88-90, 2006.
[17] M.S. Park, G.X. Wang, Y.M.Kang, D. Wexler, S.X. Dou, H.K. Liu, "Maximum Li storage in Si nanowires for the high capacity three ..." Angew. Chem. Int. Ed., 46, pp.750-752, 2007.
[18] G.X. Wang, J.S. Park, D. Wexler, M.S. Park, J.H. Ahn, "Preparation of SnO2/Carbon Composite Hollow Spheres and their ..." Inorg.Chem.46, pp.4778-4780, 2007.
[19] C.J.Brinker, G.W. Sherer, "Preparation and characterization of ultra-thin sol–gel films" Sol-Gel Science. Academic Press, San Diego, 1990.
[20] M.S. Park, Y.M. Kang, J.H. Kim, G.X. Wang, S.X. Dou, H.K. Liu, "SnO2 nanosheets grown on graphene sheets with enhanced lithium ..." Carbon. 46, pp.35-38, 2008.
[21] M.S. Park, Y.M. Kang, G.X. Wang, S.X. Dou, H.K. Liu, "Structural and electrochemical properties of a porous ..." Adv. Funct. Mater.18, pp.455-458, 2008.
[22] G.X. Wang, J.S. Park, M.S. Park, X.L.Gou,"Nanostructured semiconducting metal oxides for use in gas sensors" Sensor and Actuators B: Chemical, 8, pp. 265-270, 2008.
[23] M.S. Park, G.X. Wang, S.Y. Kim, Y.M. Kang, H.K. Liu, S.X. Dou, "Synthesis of Tin Dioxide Octahedral Nanoparticles with Exposed ..." Electrochem. Commun.9, pp.71-75, 2007.
[24] Z.W. Pan, Z.R .Dai, Z.L .Wang, "Nano engineering of structural, functional, and smart materials" Science. 291, pp.1947-1950, 2001.
[25] G .Spezia, "The growth and properties of large crystals of synthetic quartz." Atti. Accad. Sci. Torino. 44, pp. 9599, 1909.
[26] R.I .Walton, "General synthesis of metal sulfides nanocrystallines via a simple ..." Chem. Soc. Rev. 31, pp.230-232, 2002.
[27] K.F .Zhang, S.J. Bao, X.Liu, J .Shi, "Vanadium dioxide nanobelts: Hydrothermal synthesis and magnetic ..."Materials Research Bulletin. 41, pp.1985-1988, 2006.

[28] H.T.Feng, R.F.Zhuo, J.T.Chen, D.Yan, J.J.Feng, H.J.Li, S.Cheng,P.X.Yan, “Synthesis, Characterization, and Microwave Absorption Property of ...” Physica E. 41, pp.1640-1642, 2009.
[29] Hyoun Woo Kim, “SnO2 microparticles by thermal evaporation and their properties ...” Seung Hyun Shim, Chongmu Lee, CeramicsInternation. 32, 943-946, 2006.
[30] Zhengtao Deng, Bo Peng, Dong Chen, Fangqiong Tang, and Anthony J. Muscat, “Orientated Attachment Assisted Self-Assembly of Sb2O3 Nanorods ...” Langmuir. 24, 11089-11095, 2008.
[31] J. Wang, D. Zhou, P. Fraundorf and J. Liu, “Synthesis and Characterization of Antimony-doped Tin Oxide ...” Microsc Microanal. 13, 2-4, 2007.
[32] Gercher V.A.; Cox D.F. Water-adsorption on stoichiometric and oxygen deficient SnO2 (110) surfaces. Surf. Sci. 1995, 322, 177-184.
[33] D.F. Cox, T.B. Fryberger and S. Semancik, Phys. Rev. B, 38(1988)2072.
[34] P.A. Cox, R.G. Egdell, C. Harding, W.R. Patterson and P.J. Tavener, Surf. Sci., 123(1982)179.
[35] J.M. Temlin, R. Sporken, J. Darville, R. Caudano, J.M. Gilles and R.L. Johnson, Phys. Rev. B, 42(1990)11914.
[36] V.A. Gercher, D.F. Cox and J.-M. Themlin, Surf. Sci., 306(1994)279.
[37] V.A. Gercher and D.F. Cox, Surf. Sci., 312(1994)106.
[38] Dai Z.R.; Pan Z.W.; Wang Z.L. Ultra-long single crystalline nanoribbons of tin oxide. Solid State Commun. 2001, 118, 351-354.
[39] Cavicchi R. E; Semancik S.; Antonik M. D.; Lad R.J. Layer-by-layer growth of epitaxial SnO2 on sapphire by reactive sputter deposition. Appl. Phys. Lett. 1992, 61, 1921-1923.
[40] Batzill M.; Burst J. M.; Diebold U. Pure and Co-doped SnO2 (101) films grown by MBE on Al2O3. Thin Solid Films 2005, 484, 132-139.
[41] Smaali Assia, Outemzabet Ratiba, Media El Mahdi and Kadi Mohamed, “Optical Reflectance of Pure and Doped Tin Oxide: From Thin Films to Poly-Crystalline Silicon/Thin Film Device”, International Journal of Chemical and Biological Engineering, Vol. 2, 2009, pp. 48-51.
[42] Batzill M.; Katsiev K.; Diebold U. Surface morphologies of SnO2 (110). Surf. Sci. 2003, 529, 295-311.
[43] O. Lupan, L.Chow ,G.Chai, H.Heinrich, S.Park, A.Schulte , “Synthesis of one-dimensional SnO_2 nanorods via a hydrothermal ...” Physica E. 41, 533-534, 2009.
[44] Liu, X.W.; Li, J.W.; Zhou, L.; Huang, D.S.; Zhou, Y.P. Adsorption of CO2, CH4 and N2 on Ordered Mesoporous Silica Molecular Sieve. Chem. Phys. Lett. 2005, 415, 198-201.
[45] Kim, J.C.; Jun, H.K.; Huh, J.-S.; Lee, D.D. Tin Oxide-Based Methane Gas Sensor Promoted by Alumina-Supported Pd Catalyst. Sens. Actuators B 1997, 45, 271-277.
[46] Gas Detector: Analog Dialogue: Analog Devices, 2015.
[47] V.A.Henrich and P.A.Cox, The surface science of metal oxides, university press Cambridge, 1994, 312-316.
[48] Influence of Water Vapour on Nanocrystalline SnO_2 to Monitor CO and CH_4, J. Kappler, N. Bârsan, U. Weimar and W. Göpel, Conf.Proc.Eurosensors XI, 1997, 1177-1180, Warschau (P), 83-908335-0-6.
[49] Robert T. Morrison, Robert N. Boyd, Lehrbuch der organischen Chemie, 3, Auflage, VCH, Weinheim 1986, 129.
[50] Jae Chang Kim, Hee Kwon Jun, Jeung-Soo Huh, Duk Dong Lee, Sensors and Actuators B: Chemical, Volume 45, Issue 3, 15 December 1997, Pages 271–277.
[51] S. Harbeck, A. Szatvanyi, N. Barsan, U. Weimar, V. Hoffmann, Thin Solid Films, Volume 436, Issue 1, 22 July 2003, Pages 76–83.
[52] S. Munnix and M. Schmeits, Electronic structure of tin dioxide surfaces, Phys. Rev. B 27, 7624-7635.
[53] W. Hinsen, W. Bytyn, M. Baerns, Oxidative dehydrogenation and coupling of methane, Proceedings of the 8th international congress of catalysis, Berlin (1984), Vol.8, Verlag chemie, Weinheim, 581-592.
[54] Mädler, L.; Sahm, T.; Gurlo, A.; Grunwaldt, J.-D.; Barsan, N.; Weimar, U.; Pratsinis, S. E. 2006, 8.
[55] Fang, G.; Liu, Z.; Zhang, Z.; Hu, Y.; Ashur, I. A.; Yao, K. L. Phys. Status solidi 1996, 156, 15–22.
[56] Cirera, A.; Vilà, A.; Diéguez, A.; Cabot, A.; Cornet, A.; Morante, J. R. Sensors Actuators B: Chem. 2000, 64, 65–69.
[57] Song, K. C.; Kang, Y. Mater. Lett. 2000, 42, 283–289.
[58] Von Weimarn, P. P. Chem. Revs. 1925, 2, 217–242.
[59] Bassett, J.; Denney, R. C.; Jeffery, G. H. Mendham. J. Vogel’s Textbook of Quantitative Inorganic Analysis, Longman: London, 4th Ed., 1981, p. 408.
[60] Gordon, L.; Salutsky, M. L.; Willard, H. H. Precipitation from Homogeneous Solution, Wiley: NY, 1959.

[61] Ruren Xu, Wenqin Pang, Qisheng Huo, Book: Modern Inorganic Synthetic Chemistry, chapter 19, Elseiver, 2011.
[62] Kano, J.; Saito, F. Correlation of powder characteristics of talc during planetary ball milling with the impact energy of the balls simulated by the particle element method. Powder Technol. 1998, 98, 166–170. 20.
[63] Choi, H.; Lee, W.; Kim, S. Effect of grinding aids on the kinetics of fine grinding energy consumed of calcite powders by a stirred ball mill. Adv. Powder Technol. 2009, 20, 350–354.
[64] Nanocomposite Films for Gas Sensing | InTechOpen, 2015.
[65] Camargo, P. H. C.; Satyanarayana, K. G.; Wypych, F. Mater. Res. 3AD, 12, 1–39.
[66] Gas'kov, A. M.; Rumyantseva, M. N. 2001, 74.
[67] Zhang, S.; Sun, D.; Fu, Y.; Du, H. Surf. Coatings Technol. 2003, 167, 113–119.
[68] Korotcenkov, G. Sensors Actuators B: Chem. 2007, 121, 664–678.
[69] Korotcenkov, G. Sensors Actuators B: Chem. 2005, 107, 209–232.
[70] Korotcenkov, G.; Cho, B. K. Sensors Actuators B: Chem. 2009, 142, 321–330.
[71] Fang, H.; Miller, T. M.; Magruder, R. H.; Weller, R. A. J. Appl. Phys. 2002, 91, 6194–6196.
[72] Vaishnav, V. S.; Patel, P. D.; Patel, N. G. Thin Solid Films 2005, 490, 94–100.
[73] Gorley, P. M.; Khomyak, V. V.; Bilichuk, S. V.; Orletsky, I. G.; Horley, P. P.; Grechko, V. O. Mater. Sci. Eng. B 2005, 118, 160–163.
[74] Yoo, K. S.; Park, S. H.; Kang, J. H. Sensors Actuators B: Chem. 2005, 108, 159–164.
[75] T. A. Miller, S. D. Bakrania, C. Perez, M. S. Wooldridge, Functional Nanomaterials, 1-24, 2006.
[76] Sun-Woo Choi, Akash Katoch, Gun-Joo Sun, Jae-Hun Kim, Soo-Hyun Kim, and Sang Sub Kim ACS Appl. Mater. Interfaces 2014, 6, 8281−8287.
[77] Xiaobing Wang, Yuanyuan Wang, Fei Tian, Huijun Liang, Kui Wang, Xiaohua Zhao, Zhansheng Lu, Kai Jiang, Lin Yang, and Xiangdong Lou, J. Phys. Chem. C 2015, 119, 15963−15976.
[78] Nan Ma, Koichi Suematsu, Masayoshi Yuasa, and Kengo Shimanoe, ACS Appl. Mater. Interfaces 2015, 7, 15618−15625.
[79] Manjeet Kumar, Akshay Kumar, and A. C. Abhyankar, ACS Appl. Mater. Interfaces 2015, 7, 3571−3580.
[80] Nan Ma, Koichi Suematsu, Masayoshi Yuasa, Tetsuya Kida, and Kengo Shimanoe, ACS Appl. Mater. Interfaces 2015, 7, 5863−5869.
[81] Qian Liu, Zhenyu Zhang, Wenyao Li, Kaibing Xu, Rujia Zou and Junqing Hu, CrystEngComm, 2015, 17, 1800–1804.
[82] Qinghua Hu, Shantang Liu, and Yongfu Lian, Phys. Status Solidi A 211, No. 12, 2729–2734 (2014).
[83] Lin Mei, Yuejiao Chen & Jianmin Ma, Nature scientific reports, 4, 6028, 2014.

CHAPTER -3

EXPERIMENTAL

Methodologies and conditions employed

As it has been discussed in the chapters 1 and 2 of this thesis, the study of SnO_2 as gas sensing material is motivated because of its intrinsic properties but also due to its low-cost when compared with actual materials. One of the most important factors affecting the sensing properties is the presence of metals at low concentrations on SnO_2. Thus, different metals promote better responses to different gases and the chemical state of the metals, together with their dispersion on the SnO_2 surface are very important for gas-sensing properties.

This chapter deals with the description of the different experimental procedures used to prepare the tin oxide powders including the metal addition methods that has been developed. Thus, at the first part of this chapter, we explain the synthesis methods of the pure/undoped SnO_2 powders. Later in the second part, we explain the different methods used for metal addition/doping methods utilized. In the third part, the preparation of SnO_2 thick films is explained. Finally in the fourth section, different characterizations techniques used to study the powders obtained including the home made sensing system are explained in detail.

3.1. Preparation of undoped SnO_2 pellets

3.1.1. Homogeneous precipitation of tin oxide powders by route R1

- Firstly, aqueous solutions of tin chloride pentahydrate, $SnCl_4 \cdot 5H_2O$ (J.T.BAKER), and urea, CH_4N_2O, (Sigma Aldrich) with different molar concentrations (0.05, 0.1, 0.2, 0.3, 0.4, 0.5, 0.6, 0.8, and 1.2 M) were prepared. The molarity calculation is given in appendix C.1.
- Then, 1:2 mixtures from solutions with equal molar concentrations (volume proportion: 30ml of tin chloride solution and 60 ml of urea solution) were prepared.
- The different mixes were stirred and heated until a temperature of 93 ± 5^0C was reached; although the precipitation starts from 80^0C.
- The resultant precipitates were filtered by using centrifuge 30mins at 4500rpm and remove the supernatant and add the water and repeat the process for further 4 times.
- Dry the washed precipitates in an oven for 24hours at 100^0C in order to eliminate the remaining solvents.
- All the powders that are precipitated by route R1 were calcined at three different temperatures 600^0, 800^0 and 1000^0C for 2h in a normal atmosphere.
- The list of synthesis conditions (with and without the aluminum foil) and the respective production yields are listed in Table. 3.1.

It is important to draw that, as the solution temperature increases the precipitation rate is increased as well; however the solution volume is decreased due to the evaporation effect. In this respect, in order to avoid the loss of solvent, the solution containers were covered with aluminum foil. Repeatability of our results was tested for 0.4 M (sample with molarity 0.4R in Table. 3.1).

	Molarity before mixing (M)		Precipitation time (min)	Formation of precipitate	Yield before calcination (gr)
	$SnCl_4$	Urea			
Without alumina Foil	0.05	0.05	90	No	-
	0.6	0.6	90	No	-
	0.8	0.8	90	No	-
	1.2	1.2	90	No	-
With alumina Foil	0.05	0.05	2	Yes	0.20
	0.1	0.1	5	Yes	0.40
	0.2	0.2	7	Yes	1.00
	0.3	0.3	9	Yes	1.75
	0.4	0.4	10	Yes	2.2
	0.4R	0.4R	10	Yes	2.1
	0.5	0.5	20	Yes	2.8
	0.6	0.6	90	No	-
	0.8	0.8	90	No	-

Table. 3.1. List of synthesis conditions of SnO_2 powders synthesized by route R1.

3.1.2. Homogeneous precipitation of tin oxide powders by route R2

- $SnCl_4 \cdot 5H_2O$ and ammonia (NH_4OH) (J.T.BAKER, 28.0-30.0%) were used as precursors.
- Feedstock solution was prepared by mixing 0.4M $SnCl_4 \cdot 5H_2O$ with deionized water. The molarity calculation is given in appendix C.1.
- The precipitation was activated by dripping of ammonia into the feedstock solution, until the pH of the solution reached a value between 11 and 12.
- The precipitates were filtered, and then treated in the same way that route R1.
- List of synthesis conditions and the corresponding production yields are listed in Table. 3.2.
- In this route the repeatability was checked for 0.7M (Sample 0.7R in Table. 3.2).

SnO_2 concentration (M)	Volume of Solvent (ml)	Volume of Ammonia (ml)	Yield before calcination (gr)
0.05	30	4	0.5
0.2	30	8	1.5
0.4	30	12	2.5
0.5	30	17	3.0
0.7	30	22	5.53
0.7R	30	17	5.55
1.0	30	25	7.9
1.3	30	27	13.6

Table. 3.2. List of synthesis conditions of SnO_2 tin oxide powders synthesized by route R2.

Fig. 3.1, shows the resume of both routes R1 and R2 synthesis procedure with the experimental conditions used. It is observed form the figure that the filtering, drying and the calcination process are similar in both the routes.

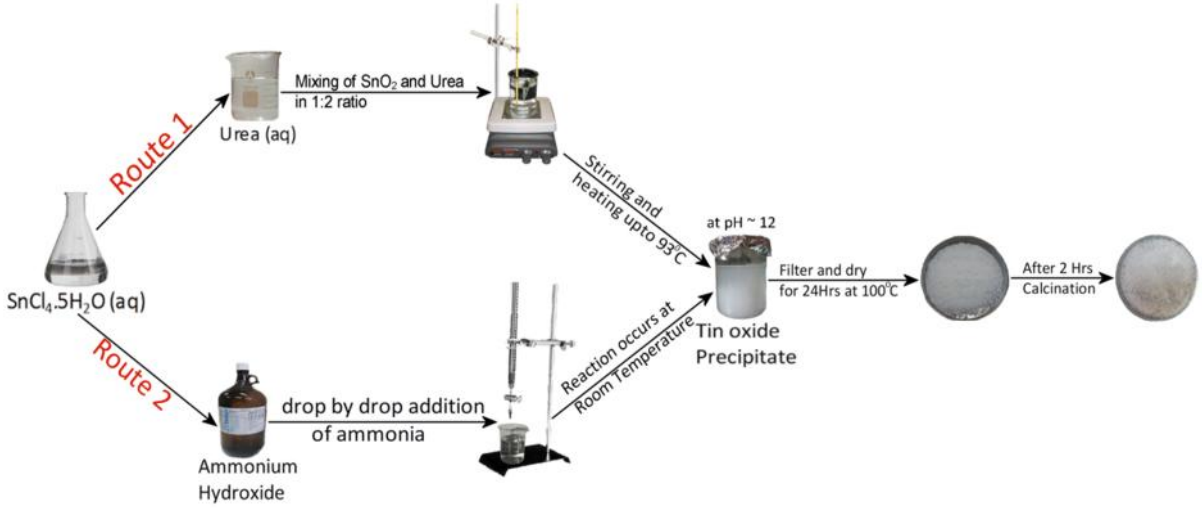

Fig. 3.1. The preparation of tin oxide powders by route R1 and R2.

3.1.3. Ball milling of SnO_2 powders

The next step consists in ball milling these powders manufactures the pellets used for gas sensing. In order to optimize ball mill and pressing conditions, approximately 100 g of SnO_2 powder were synthesized by both routes R1 and R2 each, to manufacture the pellets. The initial molar concentration and calcination temperature are optimized to 0.4 M and 800 ^{0}C in both routes R1 and R2 based on the magnitudes obtained by structural and morphological characterization of the synthesized powders. These optimized conditions are used to prepare the tin oxide powders in large scale quantities. Detailed explanation of the optimization of the synthesis parameters are given in chapter 4.

By using SEM characterization of all powders, the SnO_2 agglomerates size obtained were around 20-200nm and 15-150nm by routes R1 and R2 respectively after calcination. Therefore, to reduce the agglomerates size, ball milling was employed. The list of ball milling conditions with corresponding milling parameters were listed in Table. 3.3. The planetary ball milling PM 400 by RETSCH (Fig. 3.2) was used in our work.

Powders preparation route	Ball/powder ratio	Milling time (h)	Milling speed (rpm)
R1	5/1	4,6 and 8	300
	5/1	4,6 and 8	400
R2	5/1	4,6 and 8	300
	5/1	4,6 and 8	400

Table. 3.3. List of ball milling conditions of all synthesized SnO_2 powders.

Fig. 3.2. PM 400 Planetary Ball Milling.

3.1.3.1. Mechanics of PM 400

The grinding jars for the planetary ball mill are arranged in such a way that each moves around its own axis and, in the opposite direction, around the common axis of the sun wheel - all this at uniform speed and uniform rotation ratios. The result is that the superimposition of the centrifugal forces changes constantly (Coriolis motion). The grinding balls describe a semicircular movement, separate from the inside wall and collide with the opposite surface at high impact energy. The impact and friction forces are the reasons for the impressive size reduction [1]. There are several important variables which complicate analysis of the ball

milling process in both mills. The amount of deformation achieved for any one ball impact depends strongly on how much powder is trapped between the balls, whether the impact is between the ball and the wall of the vial or between two balls, and whether the collision is direct or glancing. In addition, collisions can cause large local heating, so the process cannot be regarded as isothermal.

There are many processing variables which can be controlled in a ball milling experiment: the material used for the vial and the balls, the size and number of balls, the amount of powder used, the ball to powder weight ratio, the volume filling fraction of the vial, processing time, average temperature, and for the planetary mills the rotation speeds of the disc and vials. Each of these variables affects the process, but only some of them affect the relevant processing intensity. The volume filling fraction, which controls the balls' mean free path and the dominant deformation mechanism. For small filling fractions, the dominant deformation mechanisms are collisions between the balls and the walls of the vials which cause fast severe plastic deformation in the processed specimens. When the filling fraction becomes large the balls are not free to move far enough to collide with each other, and the dominate deformation mechanism becomes shear deformations from balls sliding over one another. The sliding mode is less intense than the collision mode.

3.1.4. Alumina incorporation and pellet preparation

After the ball milling of the SnO_2 powders, milling time and speed were optimized (refer chapter 4) to 6h and 400rpm, respectively, from the magnitudes of particle size estimated through morphological characterization.

Later, the powders ball milled for 6 h at 400 rpm in both routes (R1 and R2) were mixed with Alumina, Al_2O_3, (Sigma Aldrich) manually in a mortar with SnO_2: Al_2O_3 ratios such as 1:0, 1:1, 2:1, and 4:1. The idea for mixing the Alumina is both to save the SnO_2 powders and for increasing the oxygen trapping. Optimization of the alumina mixing ratio was explained in chapter 4.

Subsequently, the milled powders prepared by R1 and R2, and Alumina mixed SnO_2 powders were pressed by using a manual pressing machine shown in Fig. 3.3. The optimal pressing conditions, after several trials, were 16 tons during 90 min. The schematic of the die is given in appendix C.3. The pressing machine consists of a base, a die of 12 mm diameter with two die pellets and a piston. Primarily a die pellet is placed in the die followed by the SnO_2 powder and then the other die pellet was placed which is closed by the base. Then by placing the piston on the top of the die, the required pressure is applied. The pressure should be increased in a timely manner, initially 2 tons is applied and for every increase of next 2 tons, 10 mins time gap should be maintained. Once the required pressure is reached then leave the die at that

pressure for required pressing time and the same procedure is followed while releasing the pressure too.

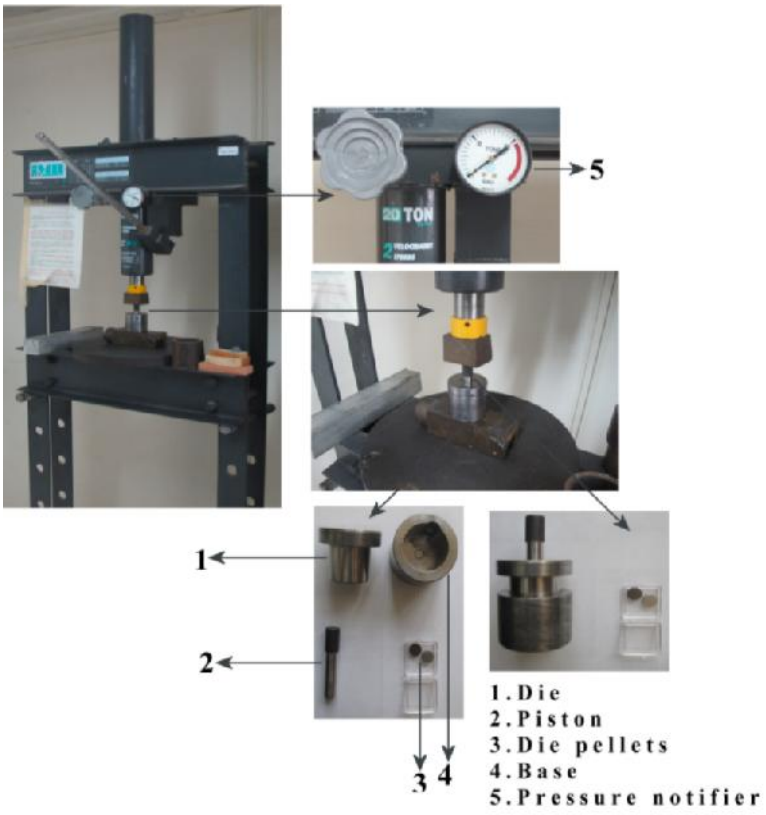

Fig. 3.3. Manual pressing machine for manufacturing the pellets.

3.2. Preparation of Cu, Pt, and Pd doped SnO_2 pellets

Doped SnO_2 powders were prepared by using two methods, one is by chemical doping (D1) and another by using impregnation method (D2). In both the routes, three different dopants were used namely, Cu, Pt and Pd. Each dopant was tested for 1 and 3 wt% in both doping routes.

3.2.1. Chemical doping (D1)

- Firstly, aqueous solution of tin chloride pentahydrate, $SnCl_4 \cdot 5H_2O$ (J.T.BAKER), with 0.4 molar concentration was prepared.
- Then, aqueous solutions of dopant chlorides, $CuCl_2$, $PtCl_2$ and $PdCl_2$ (Sigma Aldrich), with 1 wt% separately, were prepared. The doping solution calculation is given in appendix C.2.
- Feedstock solution was prepared by mixing the aqueous tin chloride pentahydrate with its corresponding aqueous dopant solution.
- Later, the feed stock solution was treated as the same way that by routes R1 and R2 to obtain the Cu, Pt and Pd doped SnO_2 powders by routes R1 and R2.
- All the doped powders obtained were also ball milled for 6 h at 400 rpm.

3.2.2. Powder impregnation (D2)

- Firstly, aqueous solutions of dopant chlorides, $CuCl_2$, $PtCl_2$ and $PdCl_2$ (Sigma Aldrich), with 1wt% separately, were prepared. The doping solution calculation is given in appendix C.2.
- Then, 1gr of ball milled SnO_2 powders prepared by route R1 and R2, were wetted with the corresponding dopant solutions prepared separately.
- All the impregnated powders were annealed at 350 ^{0}C for 2 h in air to remove the residual species.

All the doped SnO_2 powders were also pressed, similar to the undoped powders, by using a manual pressing machine (Fig. 3.3). Also silver contacts were deposited by using thermal evaporation. All the conditions of the doped tin oxide powders were tabulated below in Table. 3.4.

	Route R 1	**Route R2**
D1	Cu, Pt, Pd	Cu, Pt, Pd
D2	Cu, Pt, Pd	Cu, Pt, Pd
D1R1- powders synthesized by R1 and doped by D1		
D1R2- powders synthesized by R2 and doped by D1		
D2R1- powders synthesized by R1 and doped by D2		
D2R2- powders synthesized by R2 and doped by D2		

Table. 3.4. Doping conditions.

3.3. PREPARATION OF PURE AND Cu, Pt, and Pd DOPED SnO_2 THICK FILMS

- Firstly, solution A is prepared by mixing 0.5 g of synthesized SnO_2 powder with 7 ml of ethanol and stirred for 1 h. In parallel to this, solution B is prepared by mixing 0.25 g of ethyl cellulose, 5 ml of terpineol and 7 ml of ethanol were mixed and stirred too for 1 h.
- Feedstock solution was prepared by mixing the solutions A and B and stirred for 45 mins while heating until the solution reach for 150 ^{0}C.
- Later, the obtained SnO_2 paste was deposited at 80 ^{0}C by using doctor blade technique (refer following section 3.3.1) on a cleaned glass substrate.
- All the films deposited were annealed at 250, 350 and 450 ^{0}C, to remove the residues of carbon in the films.

3.3.1. Doctor blade technique

This technique is a chemical wetting processes in which material is applied in liquid form and then becomes solid by solvent evaporation or coating. Generic term for any steel, rubber, plastic, or other type of blade used to apply or remove a liquid substance from another surface, such as those blades used in coating paper. The term "doctor blade" is believed to be

derived from the name of a blade used in conjunction with doctor rolls on letterpress presses. The term "doctor blade" eventually mutated into the term “doctor blade” [2]. Doctor blade can be a plain rod with a gap or notch of known clearance. It is placed on the remote end of the panel to be coated and a suitable amount of paste is placed in front of it. Blade is pulled to the near end of the panel, leaving a uniform coating. The coating process is shown in Fig. 3.4 below.

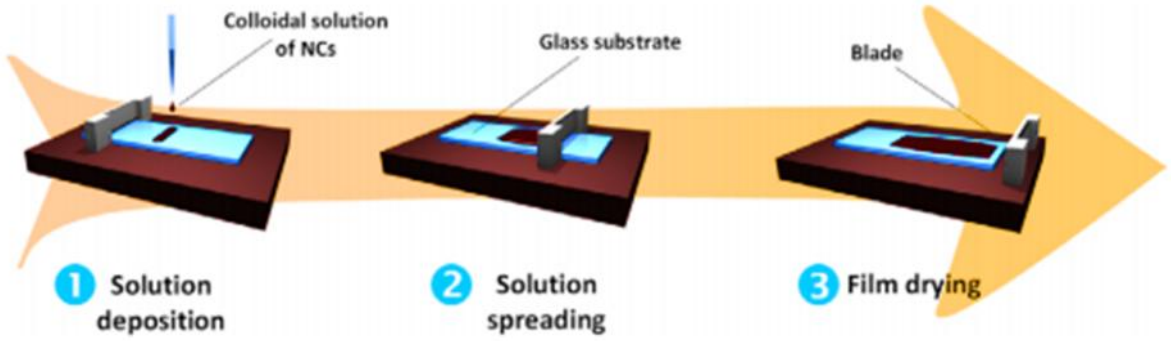

Fig. 3.4. Doctor blade coating process steps.

Some of the main parameters that can affect the deposition of the film are binder and dispersing agent, concentration of the paste, viscosity of the paste, type substrate used for deposition, the coating speed, and the angle of doctor blade. The main advantages of doctor blade technique are as follows [3]:

- Ability to deposit predetermined structures by varying experimental conditions
- Homogeneity
- Low temperature preparation
- Low production cost
- Large area production
- No material wastage compared to spin coating

3.4 CHARACTERIZATION

3.4.1 Structural characterization

X-Ray diffraction analysis using a PANalytical diffractometer with CuKα at 20 mA and 40 KV was carried out to identify the phase compound and the crystalline structure. Effect of calcination temperature was also observed by using XRD analysis. X-rays have a wavelength of the same order as the inter-atomic spacing in most crystalline substances. X-ray diffraction is thus an ideal way of probing the cell structure of a crystalline substance. About 95% of all solid materials can be described as crystalline. When x-rays interact with a crystalline substance (Phase), one gets a diffraction pattern.

In 1919 A. W. Hull gave a paper titled, “A New Method of Chemical Analysis.” Here he pointed out that “Every crystalline substance gives a pattern; the same substance always gives the same pattern; and in a mixture of substances each produces its pattern independently of the others.” The x-ray diffraction pattern of a pure substance is, therefore, like a fingerprint of the substance. The powder diffraction method is thus ideally suited for characterization and identification of polycrystalline phases [4]. Modern computer- controlled diffractometer systems use automatic routines to measure, record and interpret unique diffractograms produced by individual constituents in highly complex mixtures.

These patterns were employed to analyze the orientation as well as crystallite size of the SnO_2 samples, based on Scherer formula [5], as shown in equation 3.1.

Crystallite Size (D) = 0.89* Wavelength / (FWHM *cos (ɵ)) (3.1)

Whereas, 1.54056Å is the wavelength, ɵ is the peak position and FWHM (in radians) is the full width at half maximum (FWHM) intensity of the diffraction peaks.

3.4.2. Morphological characterization

3.4.2.1. Scanning Electron Microscopy (SEM)

SEM, by using an AURIGA equipment, was employed to examine the morphological characteristics and the particle size of the calcined particles. Also SEM was employed to analyze the surface morphological characteristics of the Undoped and Doped SnO_2 powders, and EDAX analysis was used to confirm the composition of the dopants.

The scanning electron microscope (SEM) uses a focused beam of high-energy electrons to generate a variety of signals at the surface of solid specimens. The signals that derive from electron-sample interactions reveal information about the sample including external morphology (texture), chemical composition, and crystalline structure and orientation of materials making up the sample. The SEM is also capable of performing analyses of selected point locations on the sample; this approach is especially useful in qualitatively or semi quantitatively determining chemical compositions (using EDS). SEM analysis is considered to be "non-destructive"; that is, X-rays generated by electron interactions do not lead to volume loss of the sample, so it is possible to analyze the same materials repeatedly [6].

3.4.2.2. High Resolution Transmission Electron Microscope (HRTEM)

All ball milled undoped and doped SnO_2 powders were analyzed with a HRTEM (JEM-ARF 200 F) to estimate the shape and particle size, conformation of crystal planes, and the lattice spacing.

The basic principle of HRTEM is easy to grasp [7]:

- Consider a very thin slice of crystal that has been tilted so that a low-index direction is exactly perpendicular to the electron beam. All lattice planes about parallel to the electron beam will be close enough to the Bragg position and will diffract the primary beam.
- The diffraction pattern is the Fourier transform of the periodic potential for the electrons in two dimensions. In the objective lens all diffracted beams and the primary beam are brought together again; their interference provides a back-transformation and leads to an enlarged picture of the periodic potential.
- This picture is magnified by the following electro-optical system and finally seen on the screen at magnifications of typically 10^6. This is how HRTEM is able to provide both image and diffraction information from a single sample.

The scattering processes experienced by electrons during their passage through the specimen determine the kind of information obtained. Elastic scattering involves no energy loss and gives rise to diffraction patterns. Inelastic interactions between primary electrons and sample electrons at heterogeneities such as grain boundaries, dislocations, second phase particles, defects, density variations, etc., cause complex absorption and scattering effects, leading to a spatial variation in the intensity of the transmitted electrons.

In HRTEM one can switch between imaging the sample and viewing its diffraction pattern by changing the strength of the intermediate lens. One short coming of HRTEM is its limited depth resolution. Electron scattering information in a TEM image originates from a three-dimensional sample, but is projected onto a two dimensional detector. Therefore, structure information along the electron beam direction is superimposed at the image plane. Also, the most difficult aspect of the HRTEM technique is the preparation of samples.

3.4.3. Thickness characterization

The thickness of the prepared thick films are measured using the KLA Tencor P15 profilometer instrument, which is shown in Fig. 3.6. In order to measure the thickness, it is necessary to create a step in the film. The procedure for creating step in the film is as follows:

- Mix Hydrochloric acid and water in 1:1 ratio in a beaker.
- Dip the thick film in the above mixture around 30 s in order to etch the film leaving a step on the glass substrate.
- Finally, dry the film using nitrogen to remove the residual solvent from the surface.

3.4.3.1. Working Principle A diamond stylus which moves vertically in contact with a sample and then moved laterally across the sample for a specified distance and specified contact force.

A profilometer can measure small surface variations in vertical stylus displacement as a function of position. A typical profilometer can measure small vertical features ranging in height from 10 nanometers to 1 millimeter. The height position of the diamond stylus generates an analog signal which is converted into a digital signal stored, analyzed and displayed in the system [8].

Fig. 3.8. P15 profilometer

3.4.4. Electrical characterization

For measuring the electrical response in CO and C_3H_8, pure silver ohmic contacts, by using a steel mask, were deposited on all the pure, doped and alumina mixed pellets (pellet holder was used), and also for thick films surface by utilizing thermal evaporation technique.

The measurements were made at three different operating temperatures, namely, 100, 200, and 300 °C. Lower operation temperatures do not lead to conductance changes. The conductance changes were registered by using a Keithley 2001 multi-meter. For controlling the partial pressure in the chamber a TM20 Leybold gauge detector was used. The experimental set up used for measuring resistance of the Pellets and thick films is shown in Fig. 3.5. The sensitivity of the pellets, *S*, was obtained by calculating the electrical conductance ratio from the measured resistance in vacuum (0.23 torr), G_{vac}, and in the presence of different concentrations of CO and C_3H_8, 1, 5, 50, 100, 200, 300, and 500 ppm, G_{gas}, as shown in equation 3.2.

$$S = G_{gas} / G_{vac} \qquad (3.2)$$

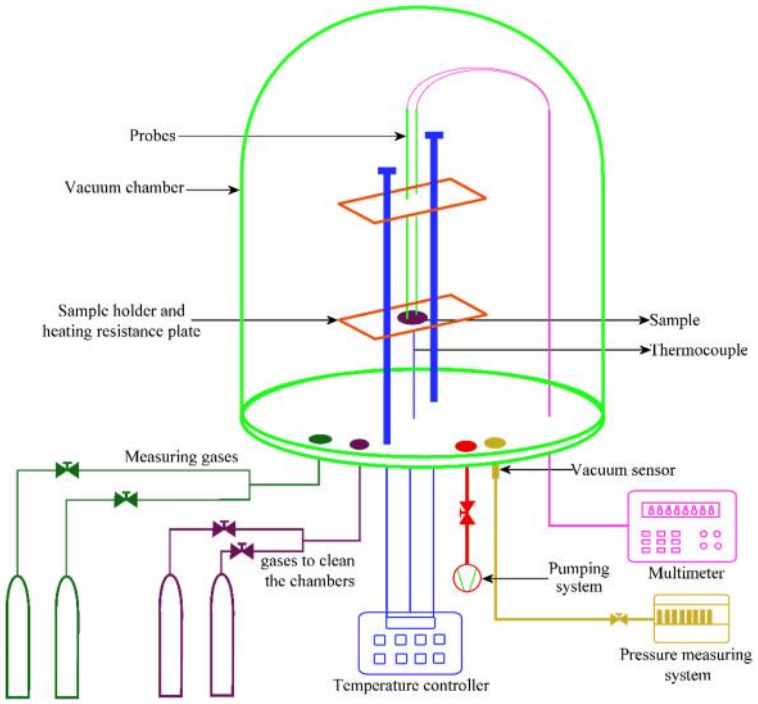

Fig. 3.5. Experimental setup for measuring the sensing response.

After receiving signals from a sensor characterization system, these signals need to be processed. The acceptable and accurate process of these signals requires: (a) full knowledge regarding the operation of the sensors and nature of signals, (b) posterior knowledge regarding the received signals, and (c) information about the dynamic and static characteristics of the sensing systems. The characteristics of a sensor can be classified into two: static and dynamic groups [8].

A significant difference between the static (***the sensor temperature should be held constant with a D.C. heater***) and dynamic (***the sensor temperature modulated through oscillation of healer voltage***) measurements [10]. In general, the information obtained from static measurements by chemical sensors is one-dimensional. For example, the change in the resistance of a semiconductor gas sensor or response and recovery time. The reaction at low temperatures is mainly surface reactions, while bulk reactions between point defects in the SnO_2 lattice and gaseous oxygen molecules become important at high temperatures. In both cases, the first step is the adsorption at active sites (intrinsic point defects like oxygen vacancies, and/or extrinsic point defects like segregated metal atoms), followed by some surface catalytic reactions. Similar reactions also occur at grain boundaries or at three-phase boundaries (e.g., at metallic contacts on surface metallic clusters). All of these reactions involve negatively charged oxygen adsorbates, either molecular (O_2^-) or atomic (O^-), as well as hydroxyl groups (OH) at different surface sites. But, it is known that static measurements are not selective to detect a

single chemical species in a gaseous mixture. Moreover, the response of the sensor in most cases is influenced by the variations of ambient humidity and temperature [10].

Other way to improve the selectivity is based on the collection and processing of signals from arrays of partially selective sensors [11, 12]. The selectivity and sensitivity of a sensor array can be greatly enhanced by developing various pattern recognition methods [13-15].

In a dynamic system, we determine how to obtain much more information from molecular recognition by a single sensor which contains abundant information. The key point in this system is the use of nonlinear dynamics in the chemical sensor, which depends on the wave shape of the frequency, the duty ratio and the applied voltage [16-20]. We can obtain many useful items of information about the sensing reaction included amplitude and frequency; it is beneficial to analyze the sensing mechanism for the gases to be tested and to enhance the selectivity. This can lead both to concentration determination and to compound discrimination [21-23].

The gas measurement system utilized in this work gives only the static characteristics of the measured samples. In our system since the temperature is controlled by a D.C. heater, and also it is not possible to obtain a multidimensional information as we explained above, we categorize our system as a static sensor and all the characteristics were obtained by considering only the superficial reactions of the semiconductor surface with the gas, irrespective of the pellets and films thickness.

3.4.4.1. Steps to follow for sensing the C_3H_8 and CO gases

- Switch on the multi-meter, vacuum pump and then the temperature controller.
- Place the sample having contacts with Ag in contact with the probes inside the chamber.
- Switch/Connect the source to the power supply.
- Close the chamber and start the Vacuum bye opening the Vacuum Valve, Let the Vacuum reach the value less than $5.0*10^{-1}$ Mbar in case of Propane sensing and $7*10^{-1}$ in Carbon Monoxide sensing then close the Vacuum Valve.
- Meanwhile set the temperature to room temperature and once the temperature is decreased and also if the Vacuum is created in the chamber close the Vacuum Valve.
- Now open the gas valve to release the gas (either propane or Carbon Monoxide) into the chamber that has to be sensed.
- Vary the gas pressure from 1 ppm to 500 ppm and the corresponding resistance in the multi-meter is noted.
- The resistance is noted for each and every gas concentration separately when the change in resistance (ΔR) saturates. ΔR depends on the type of measuring sample.
- In case of thin/ thick films, ΔR saturates after in a time interval of 15 - 45s, whereas, for pellets, the ΔR saturates around 30s to 1min.

- Therefore depending on the sample utilizing, the resistance need to be noted for each concentration, after the corresponding time intervals.
- Now close the gas valve and open the vacuum value and increase the temperature to 100 ^{0}C by using temperature controller.
- After reaching temperature and desired vacuum repeat the step 6 and step7. Similarly note the values of resistance at 200 ^{0}C and 300 ^{0}C.
- After noting all the values open the vacuum and the value of vacuum should be less than $4.0*10^{-1}$ Mbar.
- Reduce the Temperature slowly from 300 ^{0}C to 0 ^{0}C. After decreasing the temperature and vacuum remove the source plug and clean the chamber with inert gas N_2.
- List of values for C_3H_8 and CO pressures in mbar are tabulated in Table. 3.5.

Pressure (ppm)	Propane pressure (mbar)	Carbon monoxide pressure (mbar)
0	5.3*10-^{1}	7.0*10-^{1}
1	$2.7*10^0$	$8.6*10^0$
50	$2.7*10^1$	$4.3*10^1$
100	$5.5*10^1$	$8.6*10^1$
200	$1.1*10^2$	$1.7*10^2$
300	$1.6*10^2$	$2.6*10^2$
400	$2.2*10^2$	$3.5*10^2$
500	$2.7*10^2$	$4.3*10^2$

Table. 3.5. Pressure conversion table from ppm to millibar for CO and Propane.

3.4.4.2. Incommodes confronted during gas sensing measurements

During the electrical characterization, some difficulties has been faced with the characterization system, which we are projecting to resolve in future with some minor changes in the sensing system set up.

The primary difficulty confronted was regarding the response and recovery times of the sensor. One disadvantage of pellets is the quantity of the material used is more compared to thick or thin films. Therefore the time consumed fore responding also increases compared to thick or thin films. Additionally, pellet surfaces are more porous compared to thick and thin films. Therefore as the detecting gas goes into the pores existing on the surface during the sensing measurements. Since this is an electron exchange process, the recovery time taken for the gas entered into the pores will be more compared that of the gas reacted on the surface. Therefore, theoretically, the recovery time of pellets is more compared to thin or thick films. The pellets response and recovery times can be decreased by using *cylindrical tube type sensors*.

In this work we have not reported response and recovery times. In future by interfacing the multimeter with a coded program in the computer could resolve this.

The second trouble is regarding the precision of the gas concentration. The volume of the chamber utilized is around 10L. Therefore, the amount of gas entered into the chamber is not same as the amount of gas reacted with the samples surface. This can be resolved by *primarily reducing the chamber size and secondarily, employing a horizontal chamber where the gas flow is parallel to the sample surface.* All the characterizations results and their corresponding mechanisms with discussions were described in upcoming Chapter 4.

References

[1] Murty BS; Ranganathan, S. International Materials Reviews Vol. 43(3) p.101-141. 1998.

[2] Berni, M. Mennig, H. Schmidt, "Doctor Blade", Sol-Gel Technologies for glass producers and users 2004, pp 89-92.

[3] Mann, George (1952), Print: A Manual for Librarians and Students Describing in Detail the History, Methods, and Applications of Printing and Paper Making, London: Grafton, p. 62.

[4] John M. Cowley (1975) Diffraction physics (North-Holland, Amsterdam) ISBN 0-444-10791-6.

[5] Elements of Modern X-ray Physics, by Jens Als-Nielsen and Des McMorrow, John Wiley & Sons, Ltd., 2001 (Modern x-ray physics & new developments).

[6] McMullan, D. (2006). "Scanning electron microscopy 1928–1965". Scanning 17 (3): 175–185.

[7] Geuens, P; van Dyck, D (Dec 2002). "The S-state model: a work horse for HRTEM." Ultramicroscopy 3–4: 179–98.

[8] Jean M. Bennett, Lars Mattsson, Introduction to Surface Roughness and Scattering, Optical Society of America, Washington, D.C.

[9] Andmson. M.: Holm~. M.; Luudstrem, I.; Llcyd-Sperz, A.; Maru,uson. P.; Paetesse, R.: Falc:oni, C.: Proieui, E.; Sens. and Actuat. B, 2001, 71, 561-571

[10] Dinesh K. Aswal, Shiv K. Gupta, Science and Technology of Chemiresistor Gas Sensors, Chapter 4.

[11] Solis, J.L.; Soukko. S.; Ki,h, L.B.; Grnnqvi,t, C.G.: Lanno, V.; Sens. and Actuat. B, 2001, 77, 316-321.

[12] Korotcenkov, G. Sens. and Actuat. B 2005, 107, 209-232.

[13] Nanto, H.; Minami,T.: Tlli; S. *J. Appl phys* 1986, 60, 482-484.

[14] Liu, J.: Wang. X.; Peng, Q.: LIT. Sens. and Actuat. B, 2006; *115.* 481-487.

[15] Mutschall, D.: Holzner, IC; Obermeir, E. Sens. and Actuat. B, 996, *35-36,* 320-324.

[16] Frietsch, M.: Zudock. F.: Goschnick, J.; Bums, M.; Sens. and Actuat. B, 2000. 65, 379-381.

[17] Hotovy, t.: Rehecek, V.; Siciliano, P.; Cepcne, S. Spiess, L. Thin solid films, 2002, 418, 9-15.

[18] Zhao, S.; Sin. J.K.O.; Xu, B.; Zhao, M.; Peng. Z.; Chai, H., Sens. and Actuat. B 2000, 64, 83-87.

[19] Xiangfeng. C.; Xingqin. L.; Guongy M.: SetlS. Acnun. 8 1999. 55. 19·22.

[20] Holc,J.; Sluneel, J.; Hrovat, M. Sens. and Actuat. B, 1995, 26-27, 99-102.

[21] Ryzbikov. A.: Labeau, M.: Gaskov, A. Sens. and Actuat. B *2005, 109,* 91-96.

[22] Devi, G.S.; Manorama, S. V.; Rao, VJ. *J. Electrochem. Soc.* 1998, 1*45,* 1039-1044.

[23] Adamian, Z. N*;* Abovian, H.V.; Aroutioinian V .M. Sens. and Actuat. B, *1996, 35,* 241-243.

CHAPTER -4

RESULTS AND DISCCUSSION

Analysis and description

This chapter presents the results and discussion of the developed work. The first section of this chapter explains about the results and their corresponding analysis of undoped SnO_2 powders and pellets. The second section presents the results and detailed analysis of the Cu, Pt and Pd doped SnO_2. In the third section, the additional works such as, mixing of alumina with SnO_2 powders and preparation of thick films. Also their sensitivities of alumina mixed Pellets and thick films were reported. Finally, a comparison of all the sensitivities of pure, doped, alumina mixed and thick films are compared with their corresponding reasons.

4.1. Undoped SnO_2 powders by using R1 and R2 routes

In this section, the structural and morphological properties of the undoped SnO_2 powders synthesized by routes R1 (urea as precipitation agent) and R2 (ammonia as precipitation agent) are reported. Also the gas sensing in carbon monoxide, CO, and propane, C_3H_8, atmospheres were reported and analyzed for all the undoped SnO_2 pellets.

4.1.1. XRD analysis

Figs. 4.1 and 4.2 show the XRD patterns of all as-synthesized and calcined SnO_2 powders. Figs. 4.1a and 4.2a correspond to the as-synthesized SnO_2 samples prepared by R1 and R2, respectively. All the peaks showed in the XRD patterns of Figs. 4.1 and 4.2 are indexed to the tetragonal rutile structure of SnO_2 according to the reported data in the JCPDS card (77-0450), except for un-calcined samples. All spectra show a highly intense peak at $2\theta = 25.6^0$ that comes from the tape used as sample holder, and it is the reason for the double peak appearance in XRD patterns of calcined samples. The different variables used affect the synthesis of tin oxide powders synthesized by homogenous precipitation. Some of those parameters are discussed in the following section by examining the XRD and SEM characterization results.

4.1.1.1. Effect of solution temperature on the synthesis of SnO_2 powders

In R1, solution precipitation stars at a temperature around 80 ^{0}C; it is supposed that urea reacts with water, and it suffers a decomposition reaction into ammonia and carbon dioxide as shown in equation 4.1 [1].

$$(NH_2)_2CO+3H_2O \rightarrow CO_2+2NH_4^++2OH^- \qquad (4.1)$$

The preparation temperature of the solution was controlled around 93 ± 5 ^{0}C. Willard H.H. et al [2] reported that pH increases with increase in temperature, which in turn results in nucleation and growth of uniform Nano-sized particles. Then, taking into account this assertion, we consider that temperature controls the precipitation and hydrolysis rate. In R2 the precipitation it was possible at room temperature, irrespective of molar concentration of the solutions. In this case the precipitate is formed when a direct drop by drop addition of ammonia

into the tin chloride aqueous solution is carried out. Unlike in R1, the precipitation in R2 is an acid base chemical reaction, which are shown in equations 4.2 and 4.3 [3].

$$SnCl_4 + 4NH_4OH \rightarrow Sn(OH)_4\downarrow + 4NH_4^+ + 4Cl^- \quad (4.2)$$

$$Sn(OH)_4 \rightarrow SnO_2 + 2H_2O \quad (4.3)$$

Here the precipitate remains less stable than the precipitate formed by R1.

4.1.1.2. Effect of molar concentration

The different initial molar concentrations used in both routes are given in Tables 3.1 and 3.2 in chapter 3. Some facts were observed from R1, firstly, the time required for precipitation increases with the increment in the molar concentration, and the precipitation is inhibited at concentrations higher than 0.5 M. In respect of molar concentration effect, Ozge Acarbas et al. [4] reported a TGA analysis of SnO_2 powders where states that, as the initial solution concentration increases, total weight loss decreases as well. That is, in solutions more concentrated, a higher particle number is formed, and a higher production yield is obtained.

On the other hand, in our case in both routes as the initial molar concentration increased the production yield of powders before calcination was increased as well (see Tables. 3.1 and 3.2). Additionally, in both routes there was a tendency to deposit a SnO_2 thin film on the container walls, and it is more severe R1. According to X-ray results as-synthesized powders obtained from solutions with different molarities do not show significant changes (Figs. 4.1a and 4.2a), since only the (101) appears with a weak intensity. In the case of calcined powders at molar concentrations higher than 0.2M, the structural results were similar, considering that after certain molarity, depending on the precipitation agent, the formation of the powders is inhibited.

4.1.1.3. Effect of calcination temperature

All calcined powders synthesized from both routes showed a well-defined crystallinity, and no other peaks like Sn, SnO, SnO_x, Sn_2O_3, Sn_3O_4 can be identified; therefore mono-phase, pure SnO_2 powders can be synthesized. All spectra of calcined samples suggest a good crystallinity of the powders. The results show that the calcination is a compulsory process to obtain the SnO_2 phase in both routes. As was stated in the Experimental section, powders synthesized from both routes were calcined at three different calcination temperatures, namely, 600, 800, and 1000 ^{0}C. SnO_2 powders calcined at 600 ^{0}C showed good crystallinity, irrespective of synthesis route (see Figs. 4.1b and 4.2b). According to XRD spectra an increase in the calcination temperature leads to significant changes in the intensity and sharpness of the peaks and one extra peak appears as well, (111). From Figs. 4.1d and 4.2d, corresponding to powders calcined at 1000 ^{0}C, we can observe a higher intensity in the peaks compared with powders calcined at 600 ^{0}C and 800 ^{0}C from similar routes; this result can be mainly due to two facts;

firstly, an better crystallinity in the agglomerated particles at high calcination temperatures, as can be evidenced from SEM images (Figs. 4.3 and 4.4); and secondly, due to the quantity of powder on the sample holder during the X-ray analysis.

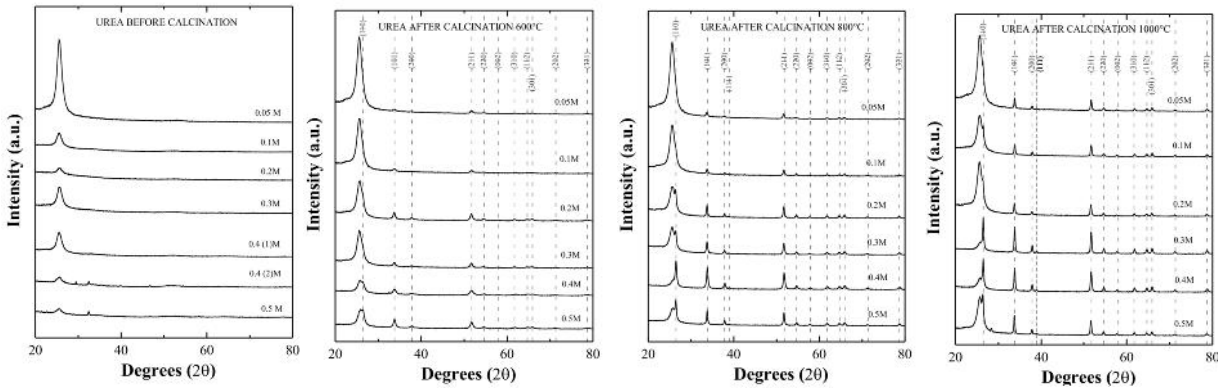

Fig. 4.1 XRD analysis of SnO_2 powders synthesized by route R1; (a) as-synthesized, and calcined at (b) 600 ^{0}C, (c) 800 ^{0}C, and (d) 1000 ^{0}C

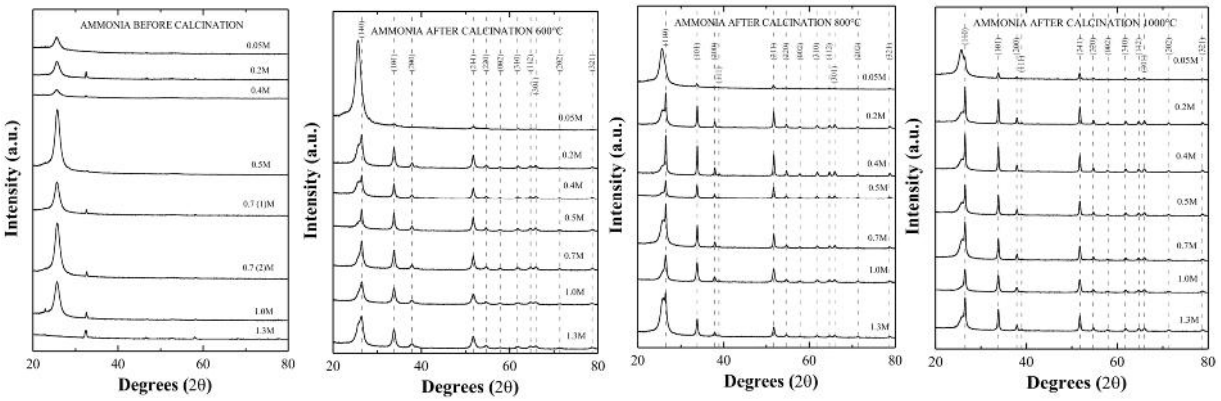

Fig. 4.2 XRD analysis of SnO_2 powders synthesized by route R2; (a) as-synthesized, and calcined at (b) 600 ^{0}C, (c) 800 ^{0}C, and (d) 1000 ^{0}C.

Many authors observed that a subsequent calcination up to 1000 ^{0}C of SnO_2 powders causes a phase transformation from orthorhombic to tetragonal phase [5, 6], which is exactly proved by us from the X-ray results (see Fig. 4.1 and Fig. 4.2). The XRD peaks in spectra of powders synthesized by both routes at 800 ^{0}C (Figs. 4.1c and 4.2c), and 1000 ^{0}C (Fig. 4.1d and Fig. 4.2d) are very similar compared to the peaks presented in samples calcined at 800 ^{0}C (Fig. 4.1 b and Fig. 4.2b) because of a phase transformation of tin oxide starts at 300 ^{0}C and is completed at 700^{0}C [6]. Thus, all XRD's of SnO_2 powders calcined above 700 ^{0}C show similar results. The above mentioned agglomeration of particles presented at high calcination temperatures was evidenced in the respective SEM images. From Figs. 4.3d and 4.4d, corresponding to powders calcined at 1000 ^{0}C by routes R1 and R2 with different agglomerate

sizes around 20-100 nm and 45 – 200 nm, respectively. Further optimization of the calcination temperature and time may increase the surface area of the particles or else a ball milling of the calcined powders could also lead to a decrease of the particle size, and consequently to induce an increase in the surface area [7].

4.1.2. SEM analysis

Figs. 4.3 and 4.4 show the SEM images of calcined SnO_2 powders prepared by R1 and R2, respectively.

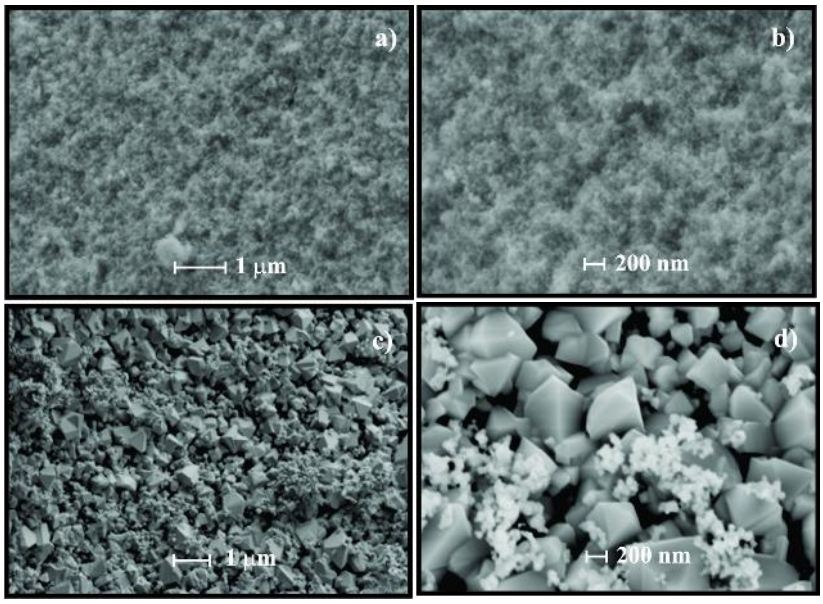

Fig. 4.3 SEM images at different magnifications of SnO_2 powders synthesized by route 1(urea) of molarity 0.4M. (a), (b) calcined at 800 ^{0}C; and (c), (d) calcined at 1000 ^{0}C.

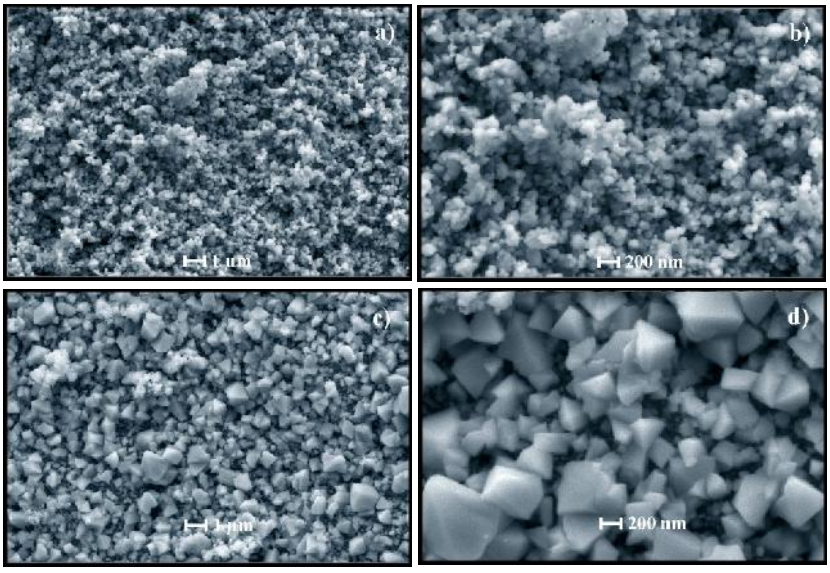

Fig. 4.4 SEM images at different magnifications of SnO_2 powders synthesized by route 2 (ammonia) of molarity 0.4M. (a), (b) calcined at 800 ^{0}C; and (c), (d) calcined at 1000 ^{0}C.

4.1.2.1. Effect of precipitation agent

As it has been stated, Urea and Ammonia were the two precipitation agents used for synthesizing the SnO_2 powders in R1 and R2, respectively. XRD patterns (Figs.4.1 and 4.2) do not show noticeable changes in the X-ray spectra. Therefore, the precipitant agents not influence the structural properties at this stage, even if it could affect the performance of the powders in gas sensing applications [1].

From SEM results (Figs. 4.3 and 4.4) we can observe that large quantities of relatively uniform particles are formed. Powders synthesized by R1 present a formation of randomly arranged crystals at high calcination temperature (see Figs. 4.3c and 4.3d), and irregular sized sponge like structures at low temperature (see Figs. 4.3a and 4.3b), similar to results obtained from powders prepared by R2 (see Fig. 4.4). In both routes, at higher calcination temperatures the sponge like structures are observed and some deep pits are also observed. Detailed morphology was not possible due to low magnification of SEM. Powders synthesized by R1 or R2 and calcined at 800 ^{0}C are more porous and uniform as compared with powders calcined at 1000 ^{0}C. Many authors reported that, the increase in calcination temperature results not only increase in particle size but also the agglomeration of the precipitated powders [4, 8].µ

At first glance, SEM show a formation of crystals for the powders synthesized by R1 and R2 at higher temperatures (1000 ^{0}C). Therefore, we can consider that, for gas sensing applications, SnO_2 powders synthesized by R1 and R2, and calcined at low temperatures are more adequate. Agglomerate size can be decreased by optimizing calcination temperature or by using ball milling. Further optimization of the calcination temperature is not possible because the minimum temperature required to obtain SnO_2 phase is700 ^{0}C, which can be observed form the XRD analysis.

4.1.2.1 Effect of ball milling on the powders morphology

As we mentioned in chapter 2, the main aim for employing ball milling is for reducing the particle size and also to obtain a narrow particle size distribution. Figs 4.5a and 4.5b corresponds to the SEM images of the ball milled powders synthesized by R1 and R2 respectively. Both the powders were ball milled for 6 h at 400 rpm.

By comparing the Figs. 4.3 and 4.4 with Fig. 4.5, the average particle size has been reduced and also the particle size distribution is very narrow. The particle sizes obtained are around 20 and 25 nm for R1 and R2 cases, respectively. It can also be observed from Fig 4.5 that the particles formed are more agglomerated. This agglomeration would have occurred due to the heat produced in the jar during the milling process. By combining XRD and SEM analysis, we can conclude that,

- Calcination is a compulsory process in order to obtain SnO_2 phase for all the powders synthesized by routes R1 and R2.
- Optimized calcination temperature is 800 ^{0}C, because, at 600 ^{0}C all the SnO_2 phases are not obtained. Whereas at 1000 ^{0}C, the particles size obtained are very high.
- Optimal initial molar concentration in both the routes is 0.4M. In case of R1, after 0.4M, no precipitate is formed. In case of R2, no structural changes were obtained with respect with the change in initial molar concentration.
- Narrow particle size distribution is achieved by employing ball milling technique. The particle size reduced from 150 to 20 nm approximately for the powders synthesized in both routes.

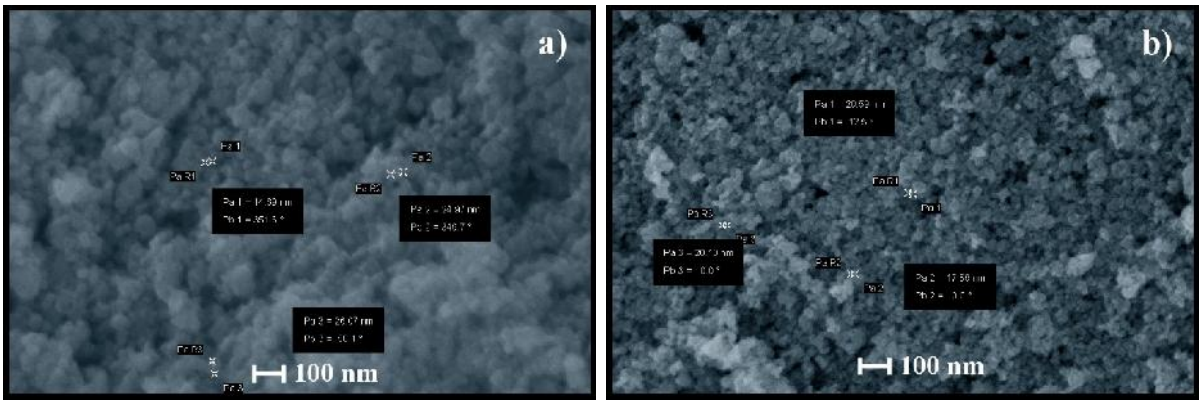

Fig. 4.5 SEM images of ball milled SnO_2 powders synthesized by (a) R1 and (b) R2 with initial molar concentration of 0.4M, calcined at 800^{0}C.

In order to have more detailed analysis of the particles synthesized and also to optimize the ball milling parameters like milling time and milling speed, HRTEM analysis of the milled powders are carried out.

4.1.3. HRTEM analysis

In order to obtain the more detailed structural and morphological information of SnO_2 crystals, HRTEM analysis was performed. Fig. 4.6a shows a HRTEM image of the ball milled, R1 prepared SnO_2 powders for 6 h at 400 rpm. In this figure we observe the fringes, which correspond to the crystal planes of the SnO_2. By using the Digital Micrograph 3.7.0 software, designed by Gatan Team we have estimated a lattice spacing of d = 3.35 Å, corresponding to the (110) main plane of SnO_2. This can also be estimated from the XRD spectrum and the Bragg´s law, and it is also reported in the datasheet of SnO_2 in JCPDS card (77-0450). Fig. 4.6b shows the reconstructed IFFT image of the Fig. 4.6a. In this image we can clearly observe the lattice fringes and the edge or boundary region between the two crystals, which is marked in

blue line. The discrepancies in the fringes were observed where the two crystals contact. The two main planes of SnO_2 are (110) and (101). The dual valence of tin allows the formation of surfaces with a Sn^{2+} or a Sn^{4+} termination. The conversion from one Sn charge state to the other is particularly easily accomplished on the (101) surface because of the atomic stacking in this crystallographic direction [9]. For the (110) surface the sample cannot easily convert from one Sn valency to another and this is one reason for the complex surface reconstructions observed and also (110) is the most stable plane compared to (101) because it has the lowest density of dangling bonds [10], therefore the complex surface reconstructions are easily possible. In our case we measure the surface resistivity change with respect to gas concentration. Therefore (110) plane is the preferential orientation for gas sensing applications. The SnO_2 (110), (101) surfaces are mentioned in chapter 2, Figs 2.2 and 2.3.

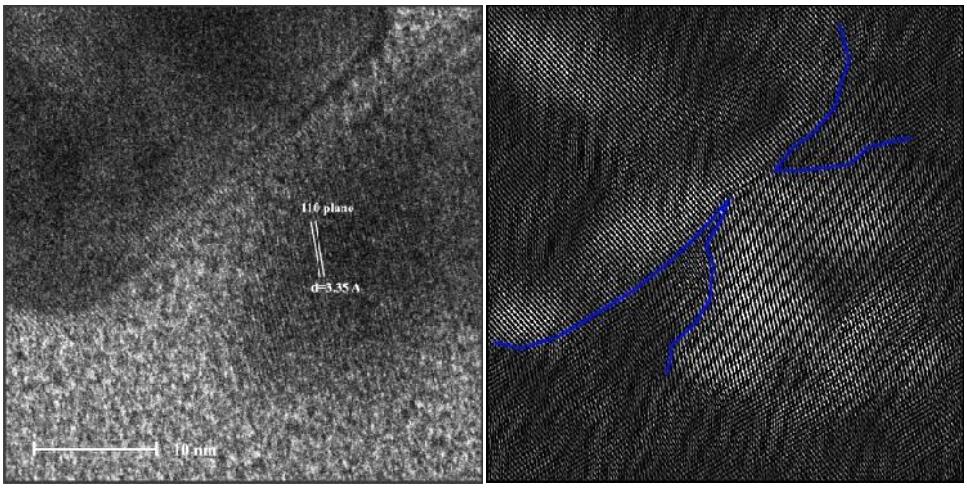

Fig. 4.6. (a) HRTEM image indicating the lattice spacing and the corresponding orientation plane. (b) Reconstructed IFFT image of (a).

4.1.3.1. Optimization of ball milling parameters

Figs. 4.7a-c show the TEM images of R1 prepared SnO_2 powders, milled at 300 rpm for 4, 6 and 8 h, respectively. All powders milled at 300 rpm show a similar particle size, around 50-70 nm, irrespective of the milling time, but powders milled for 6 h are less agglomerated. From Figs. 4.7a and 4.7c some clusters formed by agglomeration of tetragonal shaped SnO_2 particles can be observed and also the particles are not uniformly distributed; which might lead to a smooth surface and consequently to less sensitive pellets. In case of ball milled powders for 6 h at 300 rpm (Fig. 4.7b) the agglomeration of the particles is less and a uniform distribution of particle size is observed as compared with the ball milled powders for 4 and 8 h. A similar behavior is observed in R2 prepared SnO_2 powders, milled at 300 rpm with different milling times.

Since all SnO_2 powders were calcined at 800 ^{0}C, it can believed that, the high calcination temperature caused the agglomeration of the particles. Therefore milling time for 4 h is not enough to separate or distribute the particles. The agglomeration at milling time 8 h could be due to the heat produced in the ball milling jar. Therefore, the optimum milling time is chosen as 6 h and varied the milling speed. Agglomeration of the particles at a milling time of 6 h can be reduced by increasing the ultra-sonication time while preparing the samples for the HRTEM analysis.

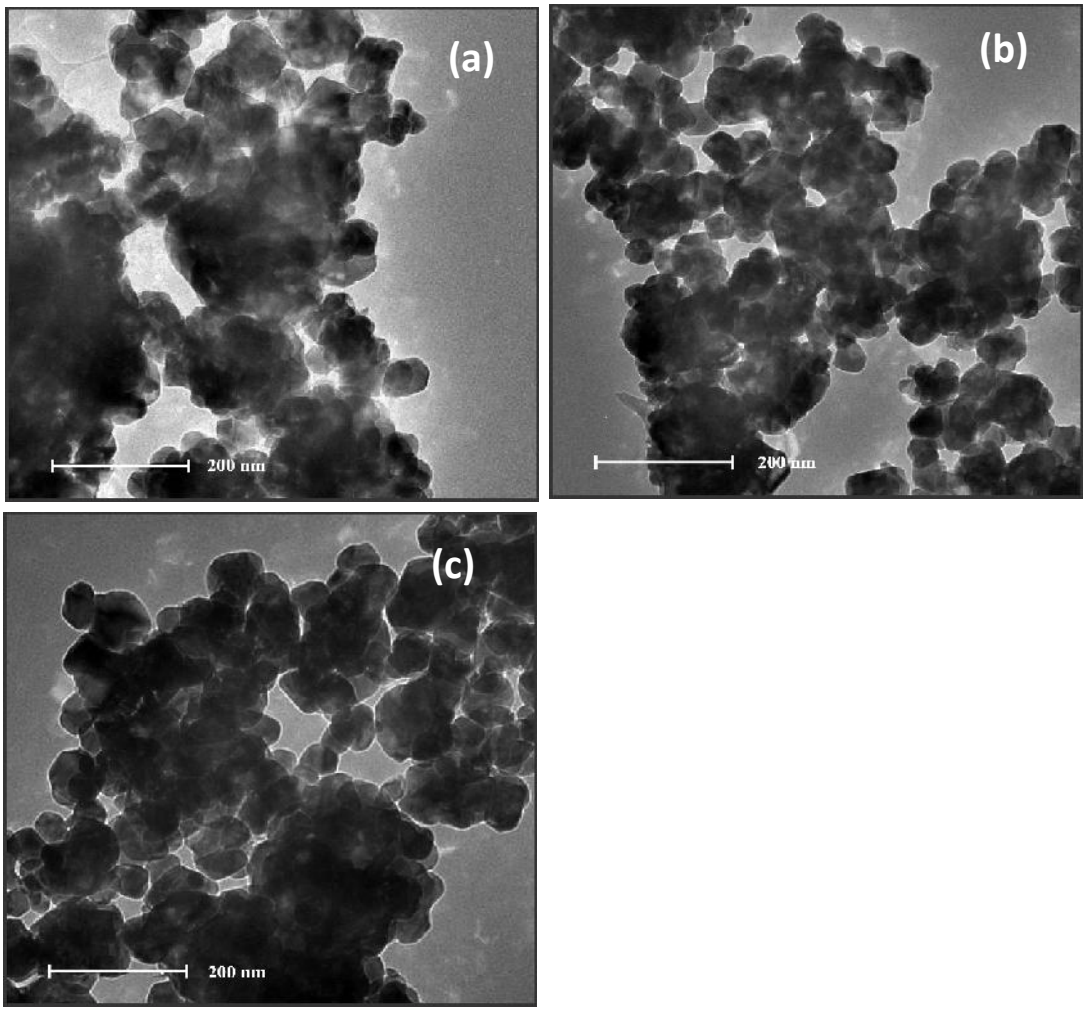

Fig. 4.7 TEM images of the powders ball milled at 300 rpm for (a) 4, (b) 6, and (c) 8 h.

Both Figs. 4.8a and 4.8b show the TEM images of the R1 prepared SnO_2 powders milled at 400 rpm for 6 h with identical magnification. The average particle size obtained for these powders is around 30-40 nm (Fig. 4.8b), which is little less particle size compared with powders milled at 300 rpm. From the Fig. 4.8a it can also be observed that the particles are clearly tetragonal. Additionally, the agglomeration is much less compared to the powders ball milled at

300 rpm. A smaller amount of agglomerates were observed as a result of having a higher milling speed.

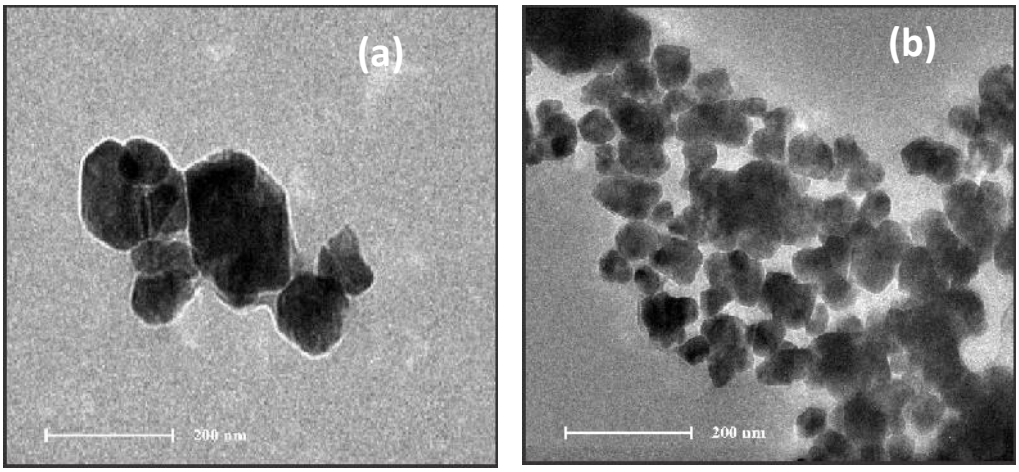

Fig. 4.8. TEM images of the ball milled powders at 400 rpm for 6 h. (a) shape confirmation, and (b) distribution of particles.

Therefore until now, from the structural and morphological analysis, we can conclude that, powders synthesized by routes R1 and R2 with 0.4 M of initial concentration, calcined at 800 ^{0}C and ball milled at 400 rpm for 6 h are better for gas sensing applications than those synthesized at different conditions. Samples obtained with above optimized conditions were considered for sensitivity measurements in both CO, and C_3H_8 atmospheres.

4.1.4. Sensitivity measurements

The sensitivity of the pure SnO_2 pellets prepared by R1 and R2 is measured in carbon monoxide (CO) atmosphere, and the corresponding sensitivities are shown in Figs. 4.9a and 4.9b respectively. From these plots, it can be observed that, sensitivity increases with the increase in the gas concentration. Since as the gas concentration increases, the number of atoms or molecules that are adsorbed on the surface increases as well, therefore both electrical conductance and the sensitivity magnitudes increase.

Sensitivity also increases with the operation temperature. In general at low temperatures (<100 ^{0}C), reaction kinetics between surface adsorbed oxygen species and the test gas is too low to show a conductance change; and at high temperatures (>400 ^{0}C), two effects are considered, firstly almost all oxygen species adsorbed have been desorbed, and secondly, the surface is covered by residual compounds coming from the combustion of the testing gas, resulting a saturation or decreasing of the sensitivity. In our case, since we measured only up to 300 ^{0}C; these phenomena cannot be observed [11]. The maximum sensitivities achieved, when pellets were measured at 300 ^{0}C and 300 ppm of R1 and R2, were 548 and 262, respectively.

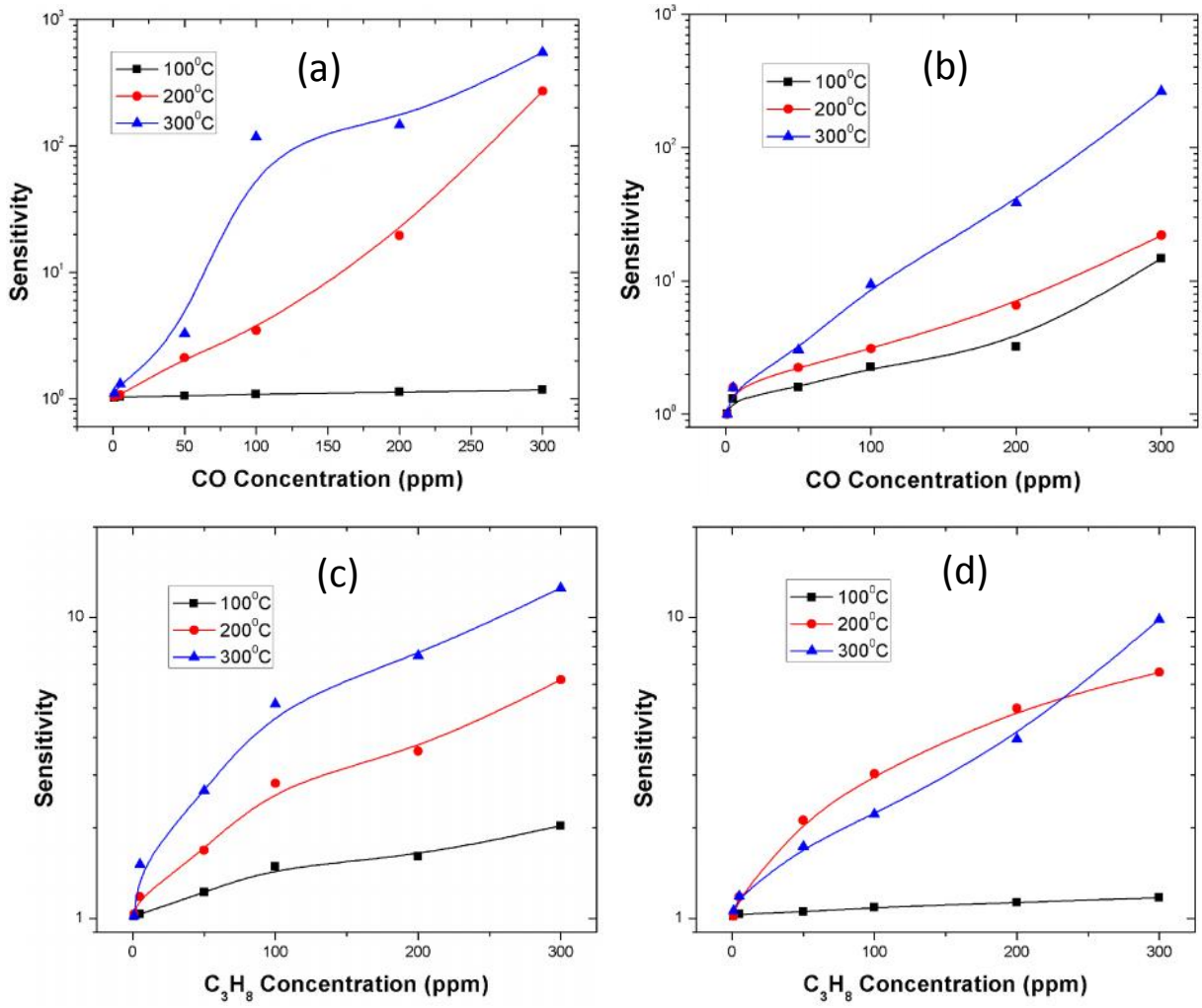

Fig. 4.9. Sensitivity of SnO_2 pellets for different CO concentrations prepared by routes, (a) R1, and (b) R2, and for different C_3H_8 concentrations prepared by routes, (c) R1, and (d) R2.

The sensitivity of the pure SnO_2 pellets prepared by R1 and R2 is measured in propane (C_3H_8) atmosphere, and the corresponding sensitivities are shown in Figs. 4.9c and 4.9d respectively. From Fig. 4.9, it can be observed that, the sensitivity shows similar behavior as in case of CO measurements. Sensitivity increases with respect to gas concentration and temperature. The maximum sensitivities achieved, when pellets were measured at 300 ^{0}C and 300 ppm of R1 and R2, were 10 and 12, respectively. In section 2.2, we have explained in detail, the gas sensing mechanism of the CO and C_3H_8 gases, in the absence and presence of O_2. From that discussion, it is evident that the CO reaction with the surface needs only adsorbed oxygen to result in conductivity. Whereas in case of propane, in order to increase conductivity the C-H bond separation should happened which need around 443 kJ/mol energy. Therefore it is apparent that the possibility of CO sensitivity is much higher compared to Propane. We believe that

increase in the operation temperature or gas concentration may result higher sensitivities in the case of propane detection.

Also from Figs. 4.9 a-d, it is important to note that, irrespective of gas, SnO_2 pellets prepared by R1 were more sensitive than R2 at 300 ^{0}C, but less sensitive when they are measured at 100 ^{0}C. Temperatures should be selected carefully depending on the testing gas, because the gas sensors vary their response depending on the testing gas and operation temperature due to the adsorption-desorption kinetics. On the other hand, the sensitivity of a SnO_2 pellet sensor depends on the stoichiometry, carrier concentration, mobility and oxygen partial pressure at a particular measuring temperature [12].

In order to further increase the sensitivity of the SnO_2 pellets, doping has been performed by using different methods. The reasons for doping and the corresponding criteria's were explained in chapters 1 and 2. The doping methods and their experimental conditions were listed in chapter 3. The following sections gives the detailed properties and corresponding sensing analysis of the doped SnO_2 powders. Since the C_3H_8 sensitivity of the undoped pellets were very less, we have continued all the remaining doped pellets sensing measurements in CO atmosphere.

4.2. Cu, Pt and Pd-SnO_2 Powders by using D1 and D2

In this section, the structural, optical and morphological properties of the Cu, Pt and Pd-SnO_2 powders synthesized by routes R1 (urea as precipitation agent) and R2 (ammonia as precipitation agent), doped by D1 (bulk doping) and D2 (surface doping). Also the gas sensing in CO atmosphere were reported and analysed by comparing with the base theory for all the doped SnO_2 pellets.

4.2.1. X-ray diffraction analysis

SnO_2 nano crystals were synthesized under different synthesis and doping conditions. Fig. 4.10 depicts the XRD patterns obtained for the Cu doped SnO_2 powders. The precipitation agent, dopants and the doping method played an important role in growth of SnO_2 crystal. In order to observe all the above parameters, all the XRD and Raman analysis graphs were plotted in 3-dimensional view. Irrespective of the synthesis route and doping method, it is evident that undoped and doped-SnO_2 powders exhibit the pure tetragonal rutile phase of SnO_2, according to the JCPDS Card 77-0450 card [13].

Due to the low amount of metallic ions doping, no other metal oxide diffraction peaks were observed in the patterns. Neither synthesis routes nor the doping methods affected the SnO_2 patterns. Besides the SnO_2 phases, the remaining peaks in the patterns came from the tape used as sample holder (the XRD pattern of glass substrate with tape, sample base, is represented in Fig. 4.11). Additionally, it is important to note that, the XRD peaks intensity is influenced by the quantity of powder utilized during the analysis.

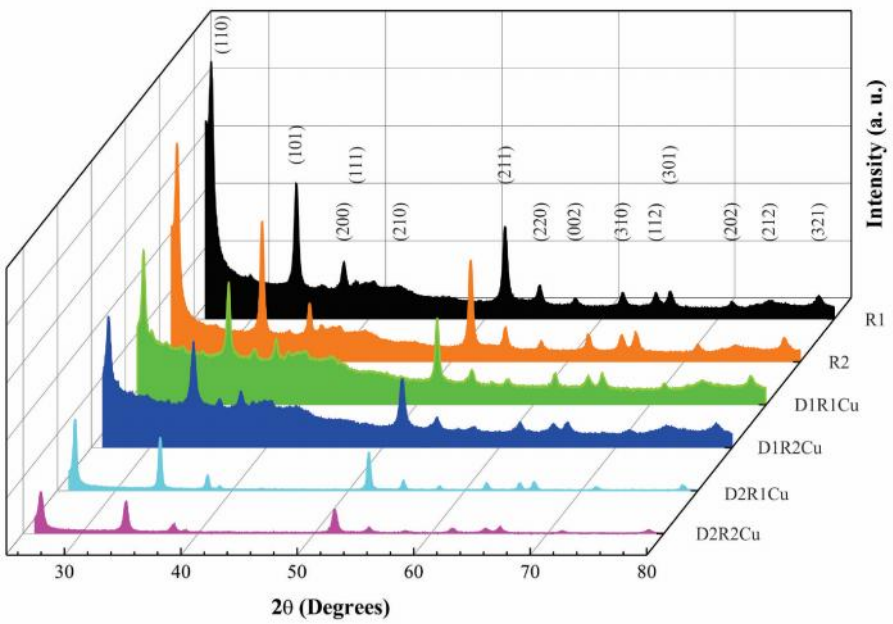

Fig. 4.10. XRD patterns of Cu doped SnO_2 powders with different synthesis and doping methods.

From Fig. 4.10, it can also be observed that, the doped powders show an upper shift in the peak positions compared to those undoped, irrespective of the doping method. Similar behavior was observed for Pt and Pd doped SnO_2 powders too. The XRD patterns obtained for Pt and Pd doped samples were shown in Fig. 4.12 and Fig. 4.13 respectively. This upper shift indicates a compressive strain in the lattice due to the ball milling process [14]. Also the upper shift observed is greater in the powders doped by method D1 than in D2, because, in case of D1, powders were ball milled in the final stage, but in D2 the additional heat treatment after the ball milling would have made the crystal to relax its strain, which in turn reduces the upper shift. There was no effect of synthesis route (R1 or R2) observed in the structural characteristics of the doped powders.

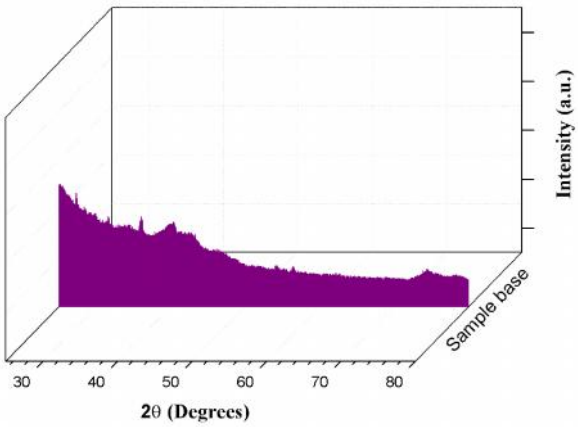

Fig. 4.11. XRD pattern of glass substrate with tape.

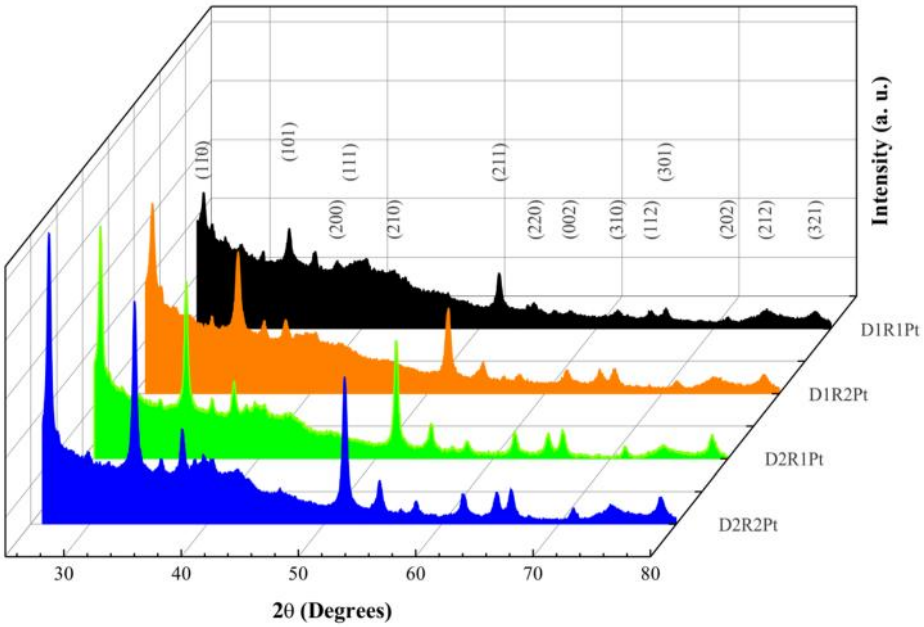

Fig. 4.12. XRD patterns of Pt doped SnO_2 powders with different synthesis and doping methods.

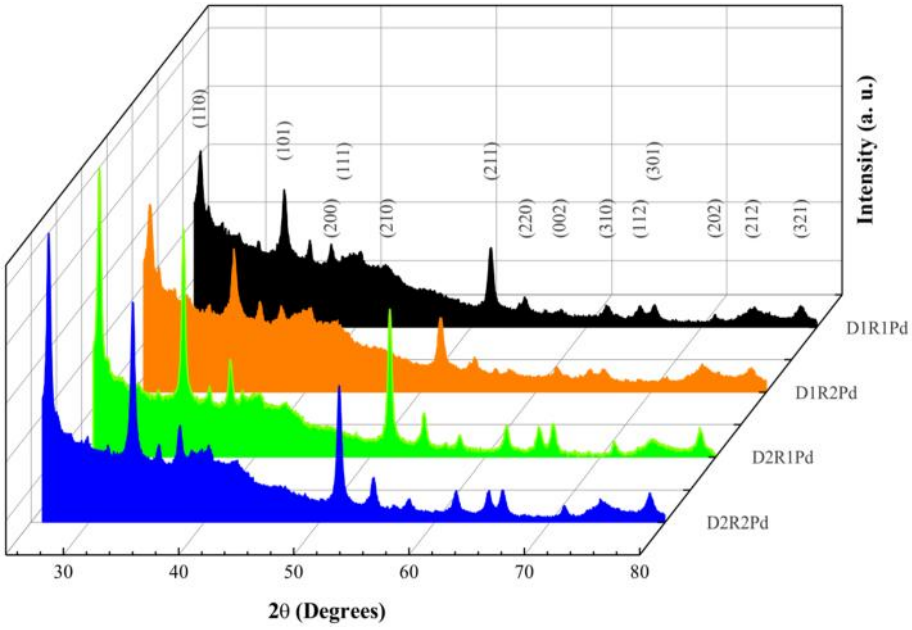

Fig. 4.13. XRD patterns of Pd doped SnO_2 powders with different synthesis and doping methods.

In order to ascertain the effect of dopants (Cu, Pt and Pd) on the structural characteristics, crystallite size (D) [15], crystal volume (V) [16] and porosity (P) [17] were calculated by using equations (4.4-4.8) and reported in Table. 4.1.

$$D = \frac{0.89\lambda}{\beta \mathrm{Cos}\theta} \tag{4.4}$$

$$V = a^2 c \tag{4.5}$$

$$P = (1 - \frac{\rho_a}{\rho_x}) \times 100\% \tag{4.6}$$

$$\rho_a = \frac{m}{v} \tag{4.7}$$

$$\rho_x = \frac{n}{\mathrm{N_A} V} \tag{4.8}$$

Where λ is the wavelength of incident X-ray (λ = 0.15418 nm), β is full width at half maximum (FWHM) intensity, θ is the Bragg's diffraction angle in radians, *a* and *c* are lattice parameters, m and v are mass and volume of the samples, n is number of molecules per unit cell, M is molecular weight and N_A is Avogadro's number.

Sample ID	D (nm)	V (10^{-24} cm^3)	P (%)
R1	26.2751	71.4083	32.30277
R2	30.028	71.643	32.42236
D1R1Cu	26.2758	71.6685	58.35864
D1R2Cu	30.0292	71.7153	58.46007
D2R1Cu	30.0357	71.724	58.46007
D2R2Cu	35.0255	71.7536	58.68875
D1R1Pt	35.0255	71.7671	64.62565
D1R2Pt	35.0267	71.7869	64.72664
D2R1Pt	35.0283	71.8223	64.75372
D2R2Pt	35.0284	71.8509	64.80217
D1R1Pd	40.0286	72.0279	73.01781
D1R2Pd	40.0291	72.0396	73.03034
D2R1Pd	42.0347	72.0396	73.04474
D2R2Pd	42.0377	72.2155	73.16012

Table. 4.1. Crystallite size (D), Volume of the crystal (V) and Porosity (P) of the Cu, Pt and Pd-SnO_2 nanocrystals.

From Figs. 4.10-4.13 and Table. 4.1, the following details can be observed:

- Cu, Pt and Pd doped SnO_2 powders crystallite size and porosity was increased respectively compared to the undoped powders. This increase is due to the increase in the ionic radii of the dopants. The ionic radii of the Sn^{+2}, Cu^{+2}, Pt^{+2} and Pd^{+2} are 0.69, 0.73, 0.80 and 0.86 Å respectively [18]. In case of Pd, as it replaces a Sn atom, due to its higher ionic radius, the crystal distance increases which in turn increases the crystallite size and porosity.
- Pd: SnO_2 pellets have higher porosity compared to Cu and Pt doped powders. Increase in the porosity increases the sensitivity. Besides porosity, sensitivity also depends on other factors like crystallite size, surface morphology and measuring temperature too. Effect of dopant on the gas sensitivity is discussed in detail later in gas sensing mechanism section.
- A linear relation is noticed between the crystallite size and volume of unit cell and is apparent because doping with an atom with higher ionic radius increases the lattice parameters of the unit cell.
- The crystallite size of the powders doped by method D1 were lesser than D2, which implies that the strain produced due to doping is lesser in case of D1. In case of D1, the later ball milling caused powders allows them to relax their stress and decreases the crystal size.
- Crystallite size of Cu: SnO_2 was lesser than the Pt and Pd: SnO_2, therefore the surface to volume ratio will be higher in the Cu: SnO_2 powders which enhances the sensitivity of the Cu: SnO_2 powders compared to the rest. Effect of synthesis route and doping method on sensitivity is discussed in detail later in gas sensing mechanism section.

4.2.2. Raman analysis

In order to confirm the effect of doping method and to understand the effect of nanoparticles on their vibrational properties, Raman spectroscopy measurements were carried out. It is well known that SnO_2 has a tetragonal structure having 6 atoms (2 Sn and 4 O) per unit cell [19]. The 6 unit cell atoms give a total of 18 branches for the vibrational modes in the first Brillouin zone. The mechanical representation of the normal vibration modes, all the vibrational modes of SnO_2 with corresponding Raman shift peaks were also widely known and reported by various authors [20-22]. Table. 4.2 resumes different frequencies of the optical modes of SnO_2, with corresponding vibrational directions.

Modes	Notation	Direction of vibration with respect to c-axis	Raman shift (cm-1)
Raman active	A_{1g}	Perpendicular	638
	B_{1g}	Perpendicular	100
	B_{2g}	Perpendicular	782
	E_g	Parallel	476
IR active	A_{2u}	Parallel	705
	E_u	Perpendicular	244
Silent	A_{2g}	Perpendicular	398
	B_{1u}	Parallel	140

Table. 4.2. Raman, IR and other vibrational modes of SnO_2.

The Raman spectra of Cu: SnO_2 with different synthesis routes and doping methods are shown in Fig. 4.14. One IR active and three raman active modes were observed at 255.2, 482.8, 637.6 and 779.2 cm^{-1}, corresponding to the E_u, E_g, A_{1g}, and B_{2g} vibration modes of SnO_2, respectively. All the modes observed corresponds to the rutile bulk SnO_2 [23]. It is interesting to note that Cu doping decreases the intensities of Raman peaks. The intensity of the Raman peaks denotes the amount of extraction and compression of Sn-O bonds inside the lattice [44]. Cu doping could be the reason to create local disorder of the bonds inside the lattice which in turn decreases the intensity of the Raman peaks.

The rate of intensity decrease is more significant in powders doped by method D1 (bulk doping) than D2 (surface doping) and is apparent because bulk doping causes more lattice disorders than the surface doping. There were no peak shifts observed from the Raman spectra because, peak shifts depends on the change in the crystallite size, and 1 wt% of doping didn't induce any significant changes in the crystallite size. It was reported by several authors [21-23] that, the minimum amount of doping percentage required to observe a peak shift in Raman spectra was around 3 wt%. From Fig. 4.14, it can also be observed that, for all pure and doped powders, the intensities of A_{1g} raman peak were less for powders synthesized by method R2 (ammonia) compared to R1 (urea). Powders synthesized by route R1 utilizes a temperature around 80^0C, for the decomposition of the urea, which causes precipitation more homogenous than R2 [25]. This homogeneity makes the powders prepared by R1 comprise of less lattice disorders than R2 which in turn decreases the intensity of the powders prepared by R2 than R1.

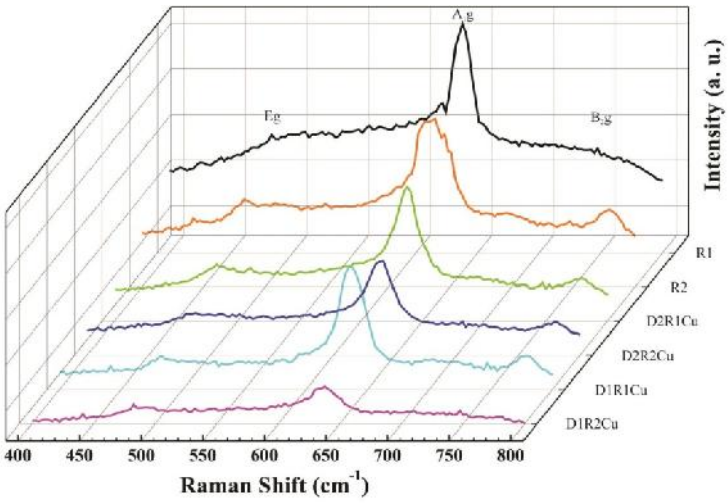

Fig. 4.14. Raman spectra of the Cu-SnO_2 with different methods D1R1, D1R2, D2R1 and D2R2.

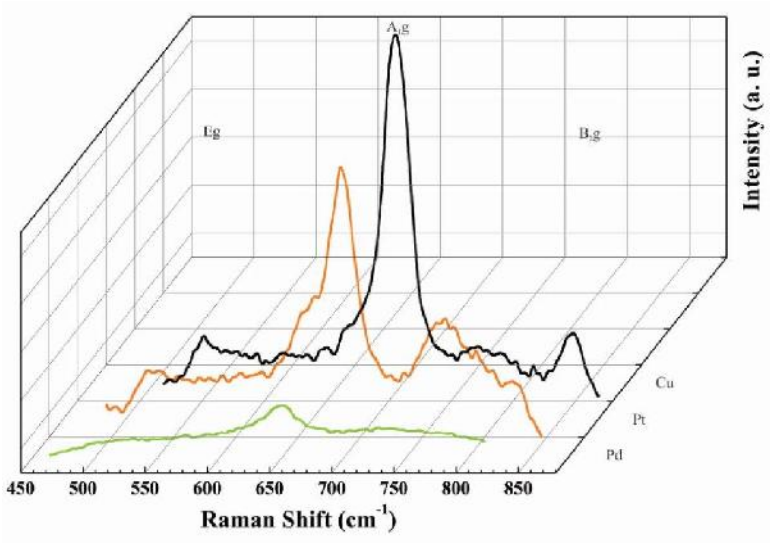

Fig. 4.15. Raman spectra of the Cu, Pt and Pd doped SnO_2 with synthesis route R1 and doping method D1.

Fig. 4.15 shows a comparison of the Raman spectra of Cu, Pt and Pd: SnO_2 synthesized by R1 and doped by using method D1. Apart from the bulk SnO_2 vibrational modes no extra modes of Cu, Pt and Pd were observed. Cu doped powders present higher intensities and Pd doped powders present the lowest intensities. This can be correlated with the ionic radii of the dopant ions. Since the Pd has higher ionic radius compared to Pt and Cu, it causes more disorders inside the lattice which makes the intensities of Pd: SnO_2 powders to diminish.

4.2.3 SEM analysis

SEM was employed to further examine and interpret the morphologies and structures of the powders with respect to the synthesized routes (R1 and R2) and doped methods (D1 and D2). The morphology of the doped powders is found to be slightly different depending on the synthesis routes and doping methods employed. Fig. 4.16a–d shows the representative SEM images of Cu: SnO_2 powders obtained by D1-R1, D1-R2, D2-R1 and D2-R2 respectively. The average diameters of Cu: SnO_2 nano particles observed are in the range 25-35 nm, which is consistent with XRD results.

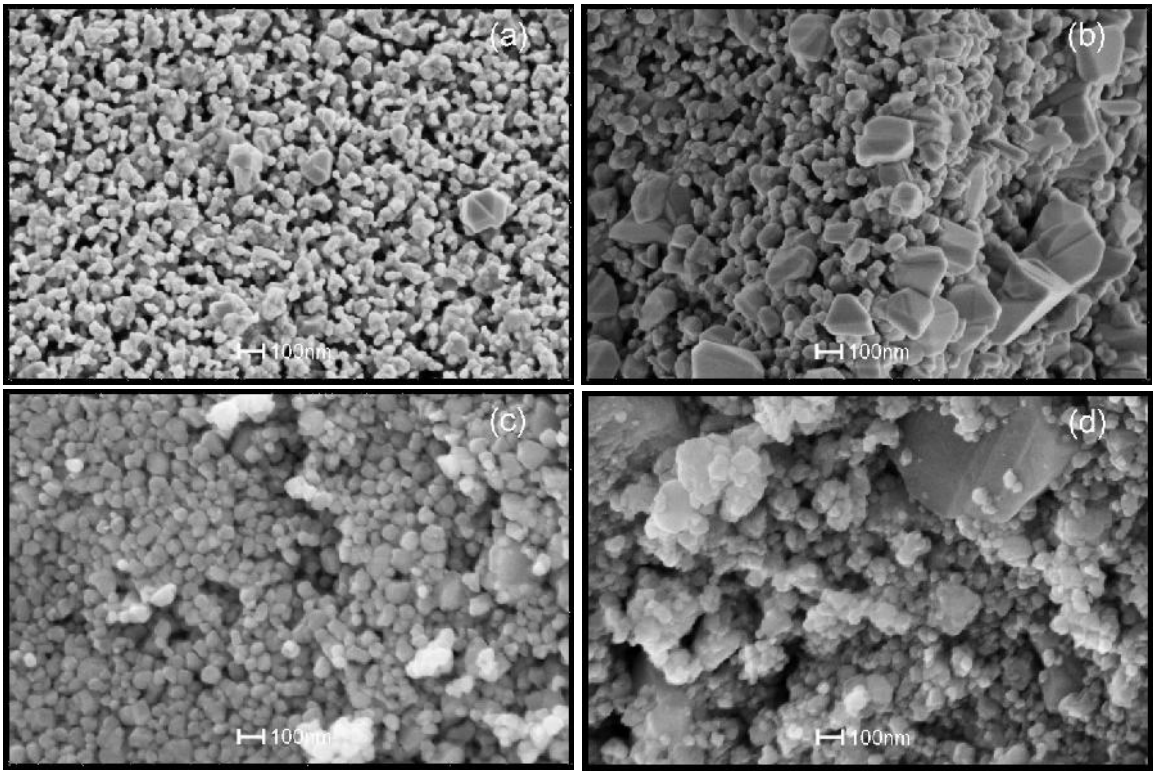

Fig. 4.16. SEM images of Cu: SnO_2 powders obtained by (a) D1-R1, (b) D1-R2, (c) D2-R1 and (d) D2-R2 respectively.

As can be seen from Fig. 4.16, powders doped by method D1 (Figures 4.16a and 4.16b) shows a contact area between particles, which is, the necks between grains. On the other hand, powders doped by method D2 (Figures 4.16c and 4.16d) shows only an agglomeration between the particles. In case of D1 (which employs bulk doping), the additives which are added during the synthesis process are incorporated in the lattice of metal oxide, which further inhibits the grain size [26] and promotes coalescence during the heat treatment. This later coalescence leads to the formation of necks between the grains [27], which in turn influence the bulk conductivity and the thickness of the space charge region. But in case of D2 (employs surface doping), the

additives which are impregnated on the thermally treated SnO_2 powders which doesn't promote the coalescence.

From Figures 4.16b and 4.16d, it is also evident that, apart from the SnO_2 nano particles, additional larger crystals around 200-600nm were observed for the powders synthesized by route R2 (Ammonia as precipitation agent) for the powders doped by both methods. The formation of larger crystals is due to the rapid precipitation at room temperature unlike in synthesis route R1. In case of powders precipitated by route R1 (Figures 4.16a and 4.16c), the elevated temperature around 90 ^{0}C utilized, had not only decomposed the urea but also assisted the precipitation to occur homogeneously [28]. This resulted in a uniform particle size and similar behavior was noticed for the Pt and Pd doped SnO_2 powders (Fig. 4.17).

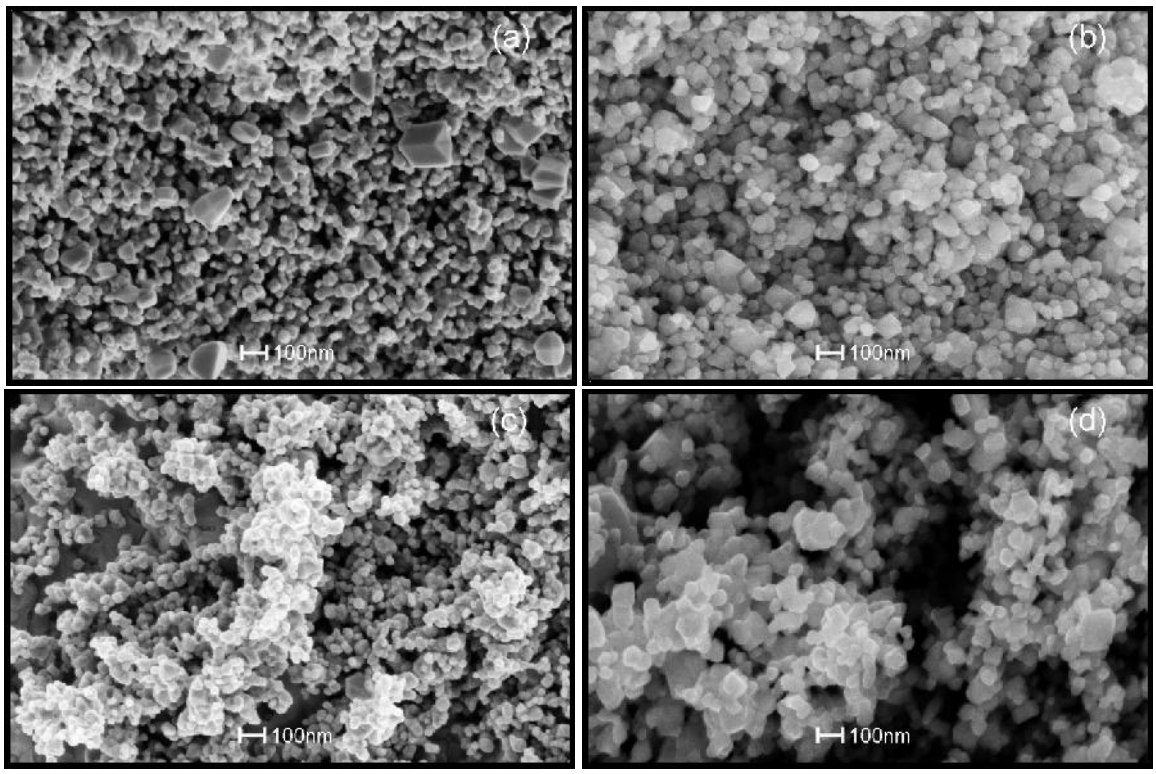

Fig. 4.17. SEM images of Pt: SnO_2 powders obtained by (a) D1-R1, (b) D2-R1 and Pd: SnO_2 powders obtained by (c) D1-R1, (d) D2-R1.

Fig. 4.17a-d shows the representative SEM images of Pt: SnO_2 powders obtained by D1-R1, D2-R1 and Pd: SnO_2 powders obtained by D1-R1, D2-R1 respectively. As similar to Cu: SnO_2 powders, Pt and Pd: SnO_2 powders also shows necks between the grains, only for the powders doped by method D1 (Figures 4.17a and 4.17c). The average diameters of Pt and Pd: SnO_2 nano particles observed are around 35 and 45 nm respectively, which is also consistent with the XRD results. The particles size increased very slightly around 10 nm for Pt and Pd compared to Cu doped powders.

From Figs. 4.16 and 4.17, we can conclude that the powders doped by method D1 are favorable to promote gas sensing because the conductivity increases due to the formation of necks between the grains [29]. Also, irrespective of the dopants used, particles with uniform size were obtained for the powders synthesized by R1. Therefore, the precipitation by using urea is more homogeneous than the ammonia. It is a fact that the homogenous structures are more favorable to gas sensing and is evident that the Cu: SnO_2 powders obtained by D1-R1 improve the sensitivity than the other methods. No noticeable effect of ball milling was observed in both the doping methods.

Porosity is another important factor that affect the sensitivity [30]. It has already been reported [31, 32] that, the SnO_2 sensitivity increases with respect to the porosity with different additives. An increment in the surface porosity will increase the active surface area which allows the sensing gas to diffuse into the bulk [33]. In order to observe the porosity of the powders obtained by D1R1, SEM images at lower magnification were acquired and reported in Fig. 4.18. We observed that the surface is porous and appears similar to a mesh, which is a consequence of having both less particle size and formation of necks between the particles.

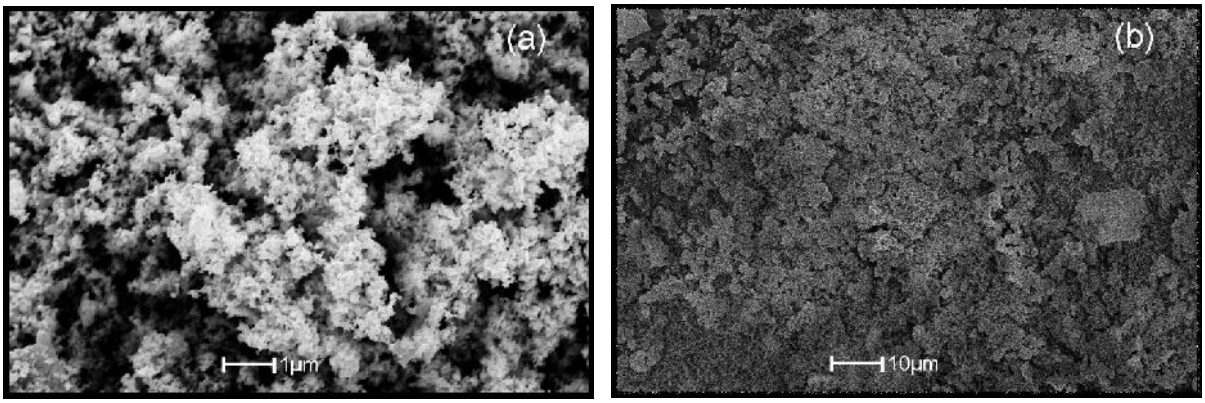

Fig. 4.18. SEM images of Cu: SnO_2 prepared by method D1R1 at magnification of (a) 1µm and (b) 10µm.

4.2.4. HRTEM analysis

It was evident from the SEM analysis that the powders synthesized by route R1 are more uniform than R2. Therefore, to obtain more-detailed information about the crystal structure of Cu, Pt and Pd doped SnO_2 particles synthesized by R1 were analyzed by HRTEM. Figs. 4.19a and 4.19b shows the TEM images of Cu: SnO_2 particles doped by method D1 and D2 respectively. All powders are composed of agglomerated nanometric crystals around 25-30 nm, which is in good agreement with the XRD and SEM results.

HRTEM images of Cu: SnO_2 particles doped by method D1 and D2 are shown in Figs. 4.19c and 4.19d respectively. The insets in Figs. 4.19e and 4.19f are the corresponding selected-

area electron diffraction (SAED) patterns. Figs. 4.19c and 4.19d HRTEM micrographs validates the difference in the doping method. Fig. 4.19c shows that, all the atomic planes were well defined and corresponds to SnO_2 crystal and its surface doesn't contain any dopants unlike in Fig. 4.19d. The *d*-spacing's measured from SAED are in good agreement with those of the (110) plane of cassiterite SnO_2 (JCPDS Card 77-0450 card) [13], corresponding to the tetragonal crystal structure (space group =*P42/mnm*).

Cu doping localized on the surface of the SnO_2 particle due to the impregnation is observed from Fig. 4.19d. The inter-plane distance measured for the copper particle corresponds (111) plane of cubic Cu (JCPDS Card 00-004-0836) [34], which confirms the cluster formation of dopants are on the surface of the SnO_2, when doped by method D2. Contrarily for the powders doped by method D1, no clusters were observed on the surface but defects produced due to the doping were observed and were marked in Fig. 4.19c.

Moreover, the (110) inter-plane distance estimated to be 3.37 and 3.35 Å for the powders doped by method D1 and D2, respectively. This increase in the lattice parameter suggests an increase of the unit cell volume for the doped powder, which can be considered as a proof of Cu insertion in the host (SnO_2) matrix. The precise position of Cu presence is SAED patterns of powders doped by method D1 and D2 were indicated in the Fig. 4.19e and 4.19f insets of SAED patterns. The estimated lattice spacing values from the HRTEM were consistent with the calculated XRD data.

A comparison of calculated d-spacing values for all the dopants and doping methods are tabulated in Table. 4.3. It is evident that no changes in the d-spacing were observed for the powders doped by method D2. Therefore, it can be stated from the HRTEM and XRD analysis that, dopants doesn't induced into the SnO_2 matrix in case of D2 and in case of D1 the dopants have created defects like stacking faults in the SnO_2 lattice. Figs. 4.19e and 4.19f, are the reconstructed images after filtering FFT pattern of their insets respectively. From Fig. 4.19e, we can observe the Cu undulations on the SnO_2 crystal, which are highlights in blue regions. Thus it can be concluded that, by using the bulk method the dopants are incorporated into the SnO_2 lattice.

From Fig. 4.19f, we can observe the copper particle on the SnO_2 surface which are highlighted with blue regions. Also no defects were noticed in the SnO_2 crystal. Therefore it can be concluded that, by using the impregnation method the dopants aren’t incorporated into the SnO_2 lattice, instead they are located on the surface in the form of clusters, which assures the possibility of spillover mechanism of gas sensing. Fig. 4.20 shows various stacking faults observed on the surface of the Cu: SnO_2 crystal with their corresponding reconstructed patterns. From Figs. 4.20d and 4.20c, the stacking faults in the lattice fringes are clearly evident. These stacking faults are attributed to the doping. These undulations were consistently observed on all surfaces of SnO_2 doped with Cu, Pt and Pd by method D1. The number of defects produced were more in case of Pt and Pd than in Cu, which is due to the higher ionic radii for Pt and Pd.

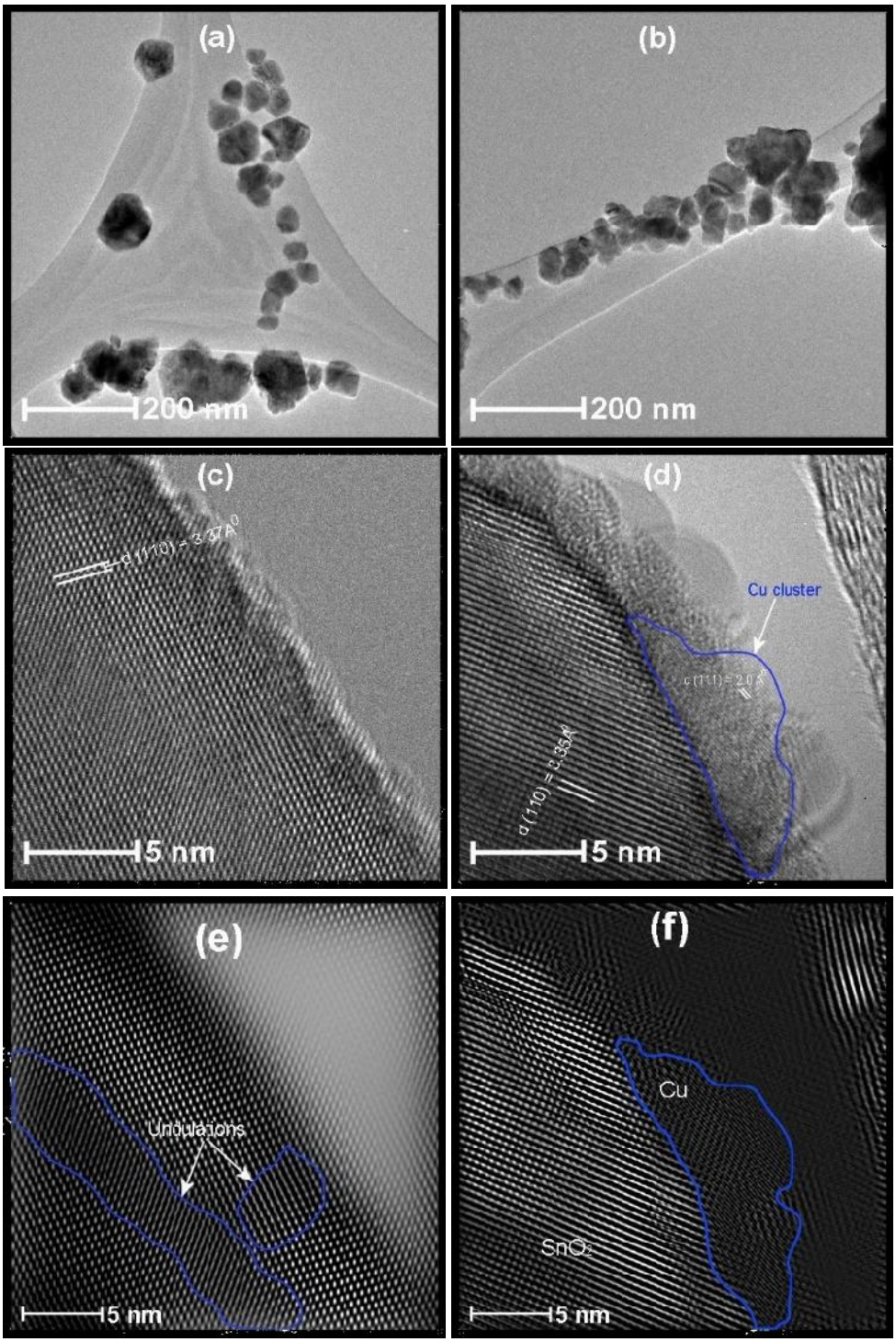

Fig. 4.19. TEM images of Cu: SnO_2 prepared by method (a) D1R1, (b) D2R1. HRTEM images of Cu: SnO_2 crystal surface prepared by method (c) D1R1, (d) D2R1, (e) reconstructed HRTEM after masking of (c); inset: the corresponding SAED pattern, and (f) reconstructed HRTEM image after masking of (d); inset: the corresponding SAED pattern.

Dopant	SnO_2 - d (110) in Å				
	Undoped	Doping method D1		Doping method D2	
		R1 (Urea)	R2 (Ammonia)	R1 (Urea)	R2 (Ammonia)
R1	3.35853	--	--	--	--
R2	3.35492	--	--	--	--
Cu	--	3.3732	3.36927	3.35382	3.35927
Pt	--	3.39422	3.38839	3.3501	3.35427
Pd	--	3.41855	3.40501	3.35697	3.35706

Table. 4.3. A Comparison of estimated d-spacing values for all the dopants and doping methods.

Figs. 4.21a and 4.21c shows the defects produced for the SnO_2 pellets doped with Pt and Pd by D1 respectively. The corresponding insets shows their FFT patterns. An overlap of different diffraction spots were observed in the FFT pattern insets which is due to the stacking faults. Reconstructed images of the Figs. 4.21a and 4.21c are shown in the Figs. 4.21b and 4.21d respectively. For Pt doped SnO_2 powders the stacking faults obtained are in the (110) plane surface, which are marked with red arrows in Fig. 4.21b. But in case of Pd doped crystals, as shown in the Fig.4.21d, the stacking faults or defects obtained on the {221} facets of SnO_2 projected from (110) plane. The {221} is one of the general facets formed for SnO_2 and can be described as combination of (001) and (110) steps [35].

According to the authors Xiguang Han, et.el [35], {221} facets are also favorable for gas sensing properties. Further detailed analysis regarding the growth mechanism of doped SnO_2 crystals is required to explain the reasons for the formation of (221) facets for the Pd doped SnO_2 crystals. The (110) inter-plane distance estimated to be 3.39 and 3.41 Å for the powders doped by method Pt and Pd, respectively.

Comparing the results of Raman and HRTEM analysis, the Raman bands of the Pt and Pd doped SnO_2 powders show an asymmetric broadening than the Cu doped SnO_2 powders (Refer Fig. 4.15). This can be attributed to the presence of dislocations and stacking faults with internal strain in the bulk of the SnO_2 crystal [36], which leads to a downshift and broadening of the A_{1g} Raman peak.

Additionally, due to the stacking faults, the crystals obtained will be with Sn enriched stoichiometry in addition to Sn-interstitials and oxygen vacancies [37]. Therefore, due to an increased [Sn]/ [O] ratio at the stacking fault will cause electronic effects. These electronic effects and oxygen vacancies may enhance the bulk conductivity, adsorption of oxygen and the test gas (CO) reaction with the pellet, which further increases the gas sensitivity.

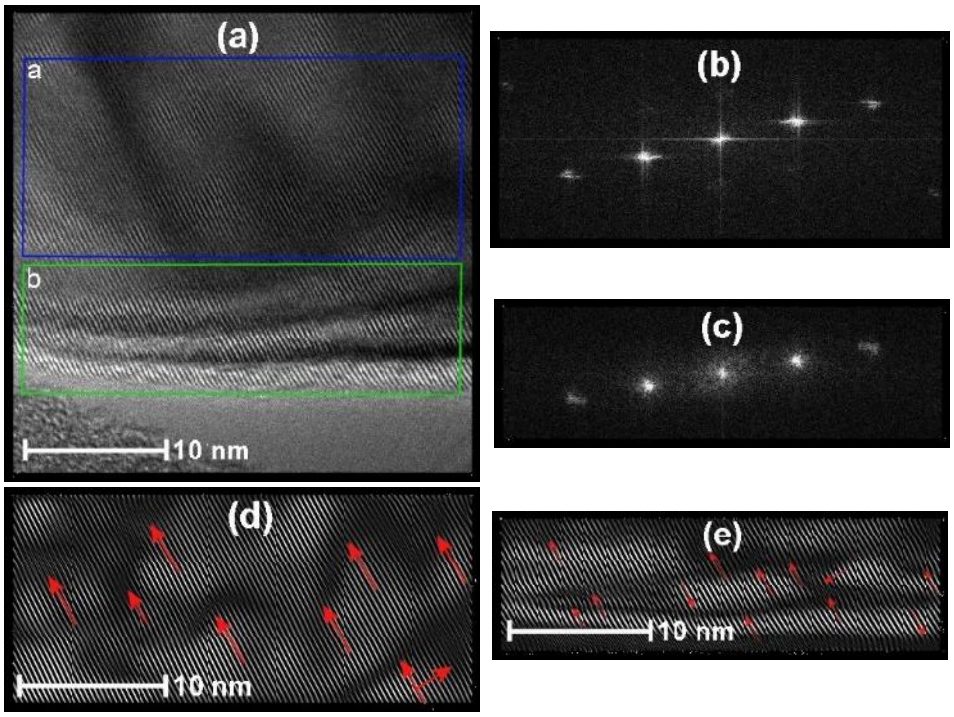

Fig. 4.20. HRTEM images of Cu: SnO_2 prepared by method D1R1 (a) surface of the SnO_2 crystal with stacking faults, (b) FFT pattern that is outlined by a blue rectangle region a in (a), (c) FFT pattern that is outlined by a green rectangle region b in (a), (d) reconstructed HRTEM after filtering the FFT spot patterns of (b), and (e) reconstructed HRTEM image after filtering the FFT spot patterns of (c).

4.2.4.1. Cu, Pt and Pd behavior on SnO_2

In order to explicate the possibilities of residing metallic copper on SnO_2 semiconductor oxide as shown in Fig. 4.19d, we have utilized the thermodynamic properties of the substances. Enthalpy, H is the thermodynamic function that accounts for heat flow in processes occurring at constant pressure when no forms of work are performed other than P-V work. At constant pressure, a change in enthalpy equals the change in internal energy plus the product of the constant pressure times the change in volume. When ΔH is positive, the system has gained heat from the surroundings – endothermic, whereas, when ΔH is negative, the system has lost heat to the surroundings - exothermic. Enthalpy changes associated with the formation of a compound from its constituent elements is known as enthalpy of formation, (or heat of formation), ΔH_f. To compare enthalpies of different reactions, a set of conditions must be defined at which the enthalpies will be tabulated. These conditions are called the standard state: a pure substance at 1 atmosphere of pressure (1 atm) and at 298 K (25 ^oC). When the temperature increases, the amount of molecular interactions also increases. When the number of interactions increase, then the internal energy of the system rises. Therefore, ΔH increases as temperature rises and vice versa [38].

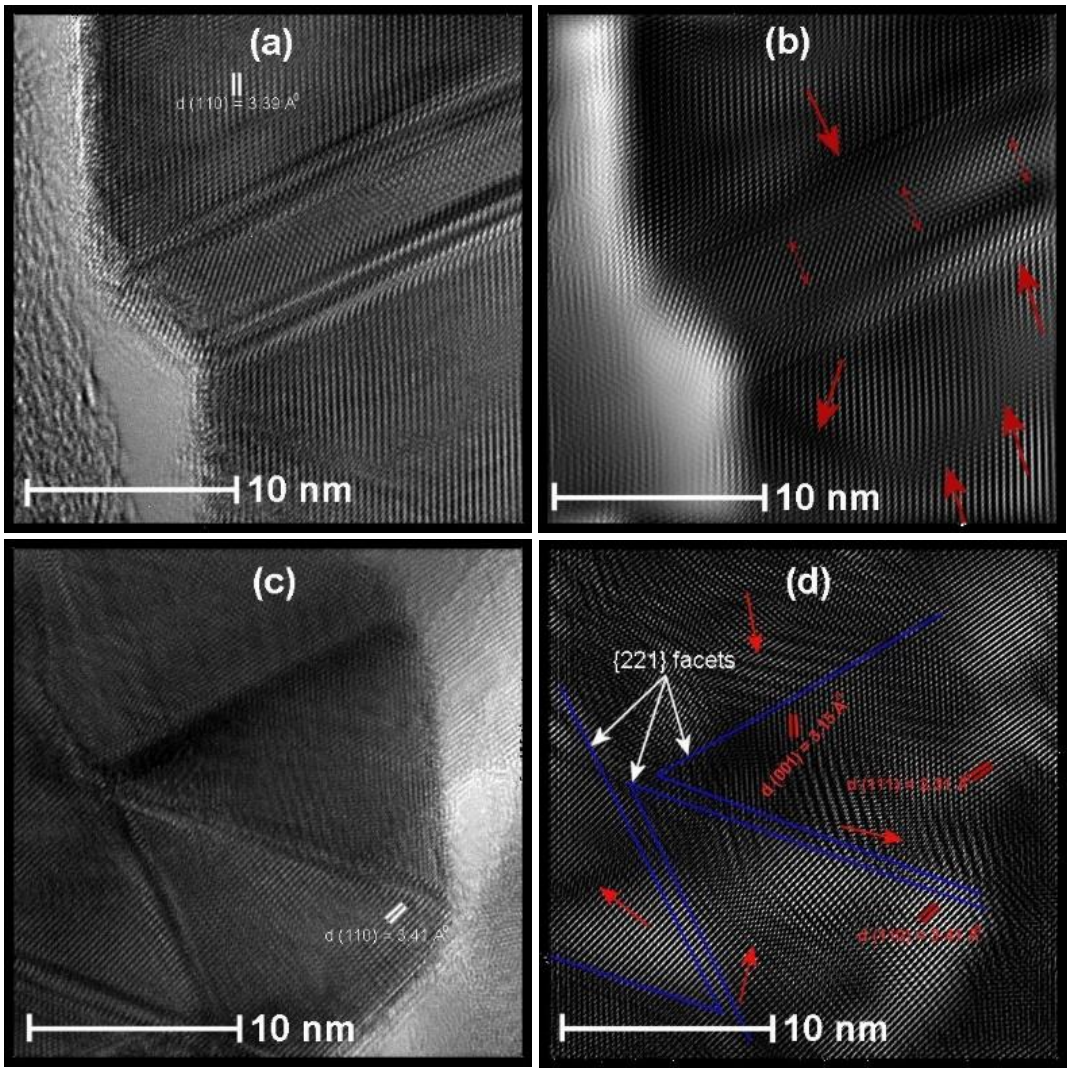

Fig. 4.21. HRTEM images of D1R1 prepared SnO_2 doped by (a) Pt; inset: the corresponding SAED pattern, (b) reconstructed HRTEM after masking of (a), (c) Pd; inset: the corresponding SAED pattern, and (d) reconstructed HRTEM after masking of (c).

When Cu reacts with SnO_2, the possible compounds formed in crystal phase are CuO, Cu_2O, SnO, and Cu_3Sn [39]. Similarly, for Pt and Pd when reacted with SnO_2, the possible compounds formed in crystal phase are PtO_2 [40], Pt_3O_4 and PdO respectively [39]. All the compounds with their corresponding standard enthalpy of formation are tabulated in Table. 4.4 [39].

From the Table. 4.4, it is evident that the highest enthalpy was observed for the formation of SnO_2, which means that the formation of SnO_2 loses more heat than the remaining compounds. Also, another important information observed is that, the enthalpy of formation of oxides of PtO_2 and PdO were in the order of around 80 kJ/mol, whereas in case of oxides of Cu are around 155-170 kJ/mol. Therefore for a given temperature the heat produced for formation

of oxides of Cu is more compared to that of the Pt and Pd. It has been reported by Thorbjorn M. Pedersen [41] that, PtO_2 phase was observed after 352^{o}C. Also it has been reported recently by Yongfu zhu [42], that the CuO phase starts after 400^{o}C and the Cu_2O phase was observed after 600^{o}C in the Arrhenius plots reported [42].

Therefore by comparing the enthalpies tabulated in Table 4.4 with the above reported results, there is a possibility of existence of metallic Cu on the surface of the SnO_2 (refer Fig. 4.19d), since we have operated the sensor at 300^{o}C. But the interface between the Cu and SnO_2 can also result in formation of Cu_3Sn because, the enthalpy of the formation of the Cu_3Sn is as low as 32kJ/mol. Therefore, we believe that the dark black region in Fig. 4.19d highlighted at the surface of the SnO_2 is Cu_3Sn compound. Further more detailed analysis and characterizations are necessary to confirm the effect of metals on the metal oxide surfaces.

Substance	**Standard Enthalpy of formation ΔH_f (kJ/mol)**
SnO_2	-580.7
SnO	-285.8
CuO	-157.3
Cu_2O	-168.6
Cu_3Sn	-31.8
PtO_2	-80
Pt_3O_4	-163
PdO	-85.4

Table 4.4. Various compounds of Sn, Cu, Pt and Pd with their corresponding Standard enthalpy of formation.

A distinction between additives that are present at the surface of SnO_2 in form of clusters or ad-layers and additives that are atomically dispersed within a SnO_2 host matrix can be made. Unfortunately, in many cases the distinction between bulk and surface dopants is not that clear cut. Cu growth on SnO_2 and TiO_2 have been reported previously [43-44], which demonstrates a three-dimensional crystalline growth of Cu islands (Volmer-Weber growth mode). The island growth mode is common for metals growing on oxide surfaces [45] due to their surface energies with respect to metal surfaces [46]. The Cu atoms form clusters on the SnO_2 (110) surface. From another previous study we know the size of the Cu clusters to be in the range of 1.5-10nm [46]. These Cu islands are quite active and play key roles in catalysis on metal-oxide surfaces.

With the increase of copper thickness on the SnO_2 surface, the substrate 1×1 LEED pattern is gradually attenuated and the characteristic Cu (111) over layer LEED pattern [45] appears. We also obtained similar kind of SAED pattern in our work (Refer Figs. 4.19e and f). From the surface-energy knowledge we know that the surface free energy of most metal oxides are very low as compared to the transition metal deposits under consideration (such as Cu, Fe

and Cr) [47]. In our case, we predict that the cluster observed of a metallic Cu due to the coincidence of the behavior of Cu on the SnO_2 surface.

Various studies of noble metal additives like Pt and Pd behavior on SnO_2 (110) surface [48] reveals that, low coverage (0.1-0.7 wt %) of additive leads to the formation of additive oxides due to the reaction of additives with the chemisorbed oxygen. Whereas, high coverage (1-5 wt %) of additives leads to the formation of metal clusters on the SnO_2 surfaces. High resolution TEM studies on the epitaxy of Pd clusters on the {110} facets of SnO_2 nano sticks are reported [47]. Semispherical Pd clusters were observed and an epitaxial relationship of [110] $(111)_{Pd}$ || [001] $(110)_{SnO_2}$ was established.

The surface adsorption energies of Pd atoms on different (defect) sites on the SnO_2 (110) surface was calculated by density functional theory [48]. In these calculations it was found that Pd clusters on stoichiometric surfaces. On reduced surfaces Pd may substitute the surface Sn atoms. Pd adsorption was found to be strongest at in-plane oxygen vacancy sites. It was also found that the Pd on SnO_2 (110) surfaces increase the gas sensitivity towards hydrogen in an order of 16 [49]. This increase was attributed to spillover of atomic hydrogen from the Pd clusters onto SnO_2. Pd cluster formation was observed for SnO_2 nano sticks impregnated with Pd upon reduction by heating in an Ar atmosphere with 5% H_2 [49]. Before reduction the Pd was either within the bulk or ultra-dispersed on the surface.

The quantity of dopant used is more compared to the literature. Therefore, we attribute that the noble metal additives like Pt and Pd in our present work have promoted gas sensing for the powders doped by method D1 and D2 by entering into host matrix and forming cluster respectively.

4.2.5. CO sensing properties

Owing to the unique doping methods and porous surfaces, CO gas sensing measurements were performed for the manufactured Cu, Pt and Pd doped SnO_2 pellets to demonstrate the potential applications in chemical sensors. The top and cross sectional view of the gas sensor employed are shown in Fig. 4.22a and 4.22b respectively. To verify the crucial role of dopants and doping methods played in the improved gas-sensing performances, pellet based sensors on SnO_2 nanostructures are employed.

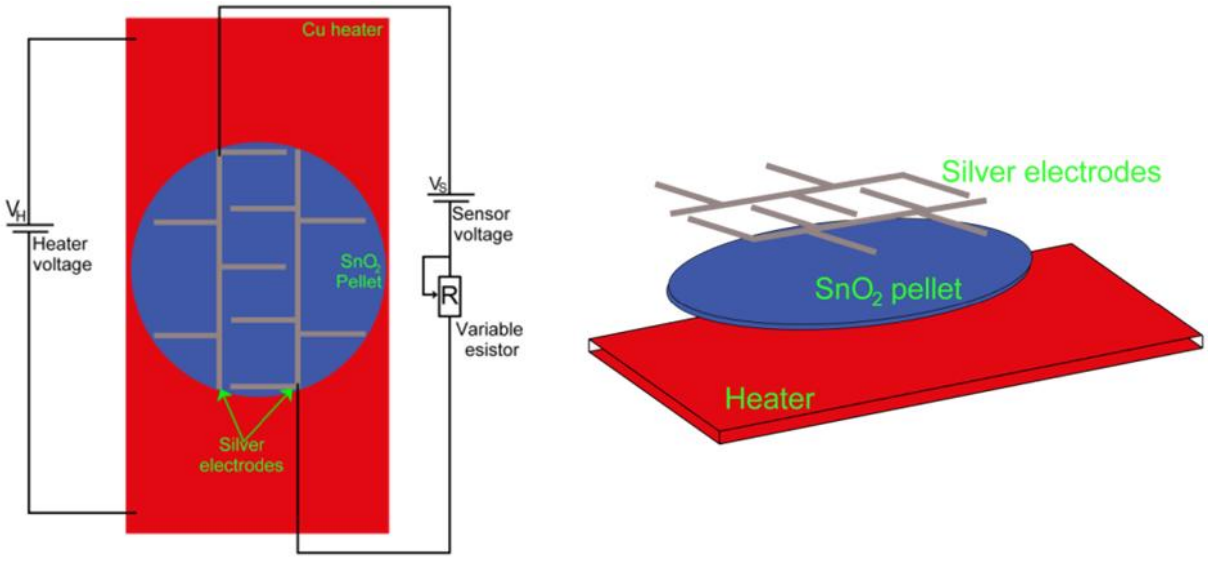

(a) (b)

Fig.4.22. (a) Top view and (b) cross sectional view of SnO_2 sensor.

In order to analyze the effect of synthesis route and doping method on the measuring temperature and CO gas concentration of our SnO_2 samples, the sensors response have been tested as a function of CO gas in the range of 1–300 ppm at 100, 200 and 300 ^{0}C temperatures. Figs. 4.23a-d corresponds to the CO sensing properties of Cu-SnO_2 prepared by methods D1R1, D1R2, D2R1 and D2R2 respectively. Table. 4.5 resumes the sensitivities obtained at 300 ^{0}C for 300ppm of CO gas concentration, for different dopants used, synthesis routes and doping methods. The undoped sensitivities are reported in our previous work [51].

From Figs. 4.23a-d and Table. 4.5, it can be observed that, irrespective of synthesis route and doping method employed, all the pellets sensitivity increases with an increment in the gas concentration and measuring temperature. Also pellets prepared by D1R1, D1R2, D2R1 and D2R2 exhibits a rapid increase of response to reach the maximum value of 1782, 1625, 975 and 1666 respectively at the measuring temperature of 300 ^{0}C.

Pellets doped by method D1 shows very less increase in sensing response when measured at 100 and 200 ^{0}C (refer insets of Figs. 4.23a and 4.23b), whereas the pellets doped by method D2 shows an effective sensing response at the measuring temperature of 200 ^{0}C too (refer Figs. 4.23c and 4.23d). Finally, irrespective of doping method, pellets manufactured from the powders synthesized by R1 show high sensitivity than R2 (refer Table. 4.5).

With the objective of identifying the effect of dopant on the CO sensitivities, the sensor response of the Pt and Pd doped SnO_2 pellets were tested for different doping methods and reported in Fig. 4.24. We can observe that, Pt and Pd doped pellets also show similar results as of the Cu doped pellets.

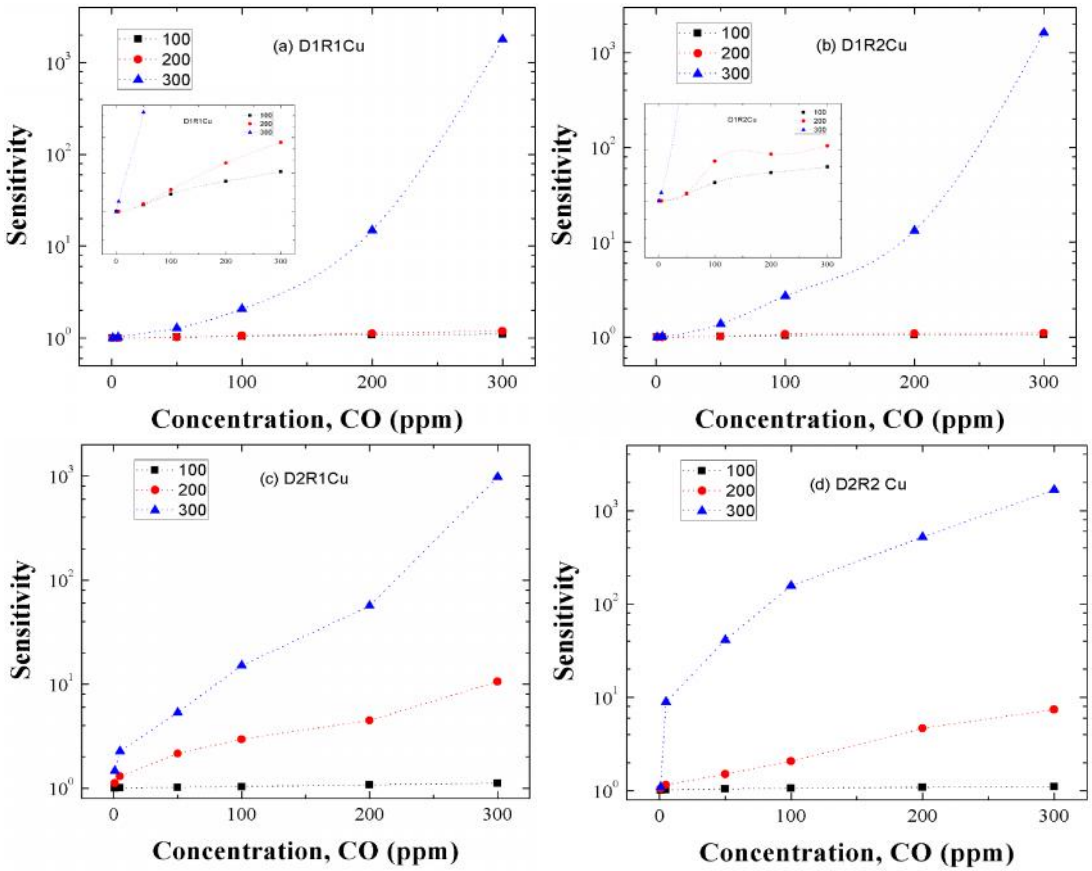

Fig. 4.23. Sensitivity of Cu: SnO_2 pellets prepared by (a) D1R1, (b) D1R2, (c) D2R1, and (d) D2R2.

	Undoped	Cu	Pt	Pd
R1	548	-	-	-
R2	262	-	-	-
D1R1		1782.609	1200	502.5
D1R2		1625	721.519	287.6405
D2R1		1666.667	428.7234	245.4546
D2R2		975.7412	387.3333	224.1485

Table. 4.5. Sensitivities at 300 ^{0}C for 300 ppm of CO of the Cu, Pt and Pd doped SnO_2 pellets prepared by different methods.

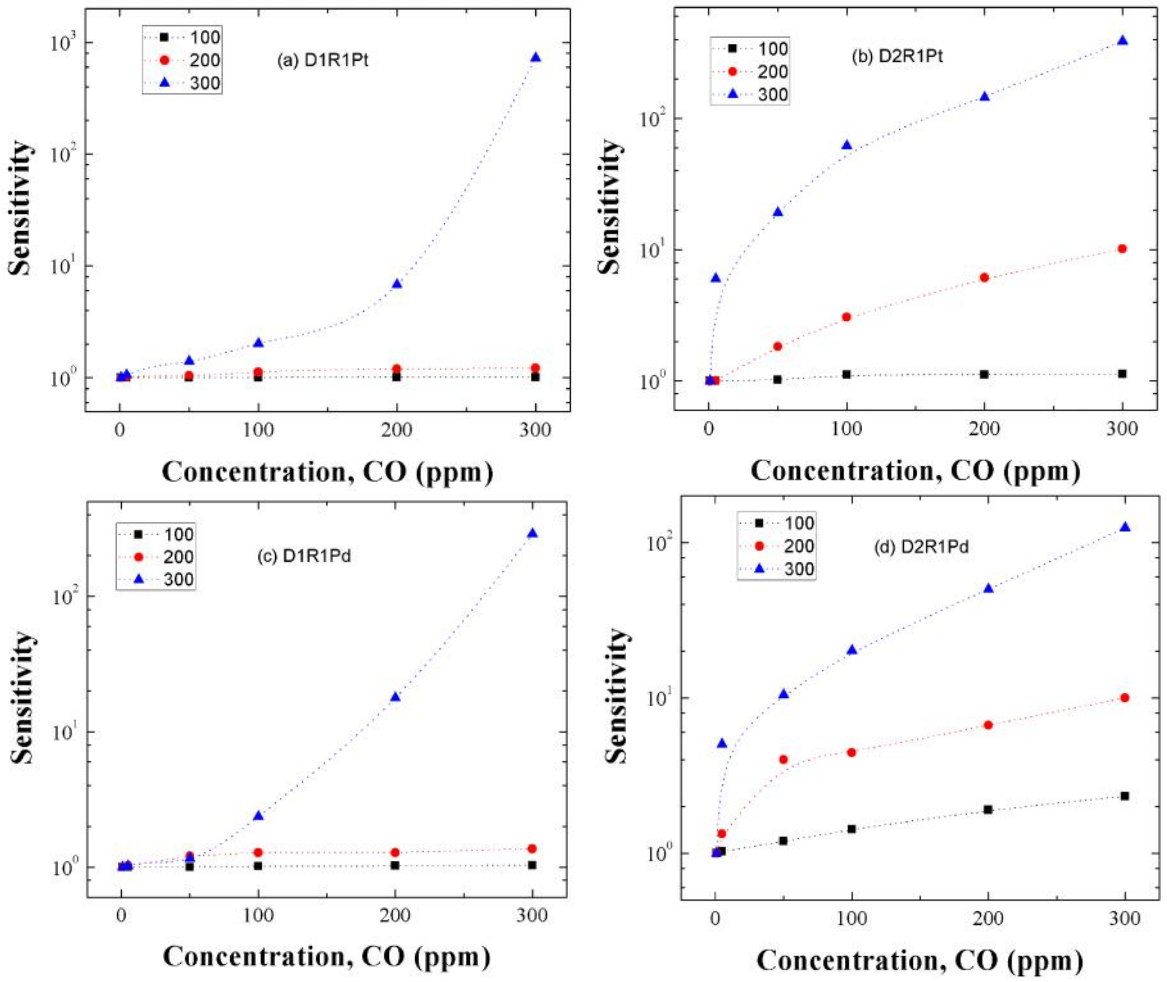

Fig. 4.24. Sensitivity of Pt: SnO_2 pellets doped by method (a) D1, (b) D2 and Pd- SnO_2 pellets doped by method (c) D1, (d) D2.

Primarily, sensitivities increases with respect to temperature and gas concentration for both Pt and Pd doped samples. Secondarily, the pellet doped by method D2 showed sensitivities at lower temperatures around 200 ^{0}C unlike for D1. Finally, the sensitivities of Pt doped samples is higher than Pd doped but is less compared to Cu doped samples. Also the sensitivities of Cu, Pt and Pd -SnO_2 samples doped by method D1 is higher than D2 (refer Table. 4.5).

Fig. 4.25 resumes out the sensitivities of the Cu, Pt and Pd: SnO_2 pellets prepared by different doping methods (D1 and D2) and synthesis routes (R1 and R2). All the sensitivities plotted in Fig. 4.25 are measured at 300°C for 300ppm of CO gas concentration. Irrespective of dopants used, doping methods and synthesis routes employed, the sensitivities of doped SnO_2 pellets are higher than undoped SnO_2 (refer Table 4.5). From Fig. 4.25 we can observe that the Cu (green bar) shows higher sensitivities that Pt (blue bar) and Pd (red bar) in all cases. Sensitivities of the pellets doped by method D1 is higher than D2. Also the sensitivities of the

pellets synthesized by route R1 is higher than R2. Even under low concentrations (1–50 ppm) and high concentrations (100–300 ppm), the response increases linearly with the CO concentration for all the measuring temperatures. Sensitivity increases with respect to the measuring temperature and gas concentration. The detailed explanation of the above obtained results and their corresponding reasons were explained in the upcoming section, Gas sensing mechanism.

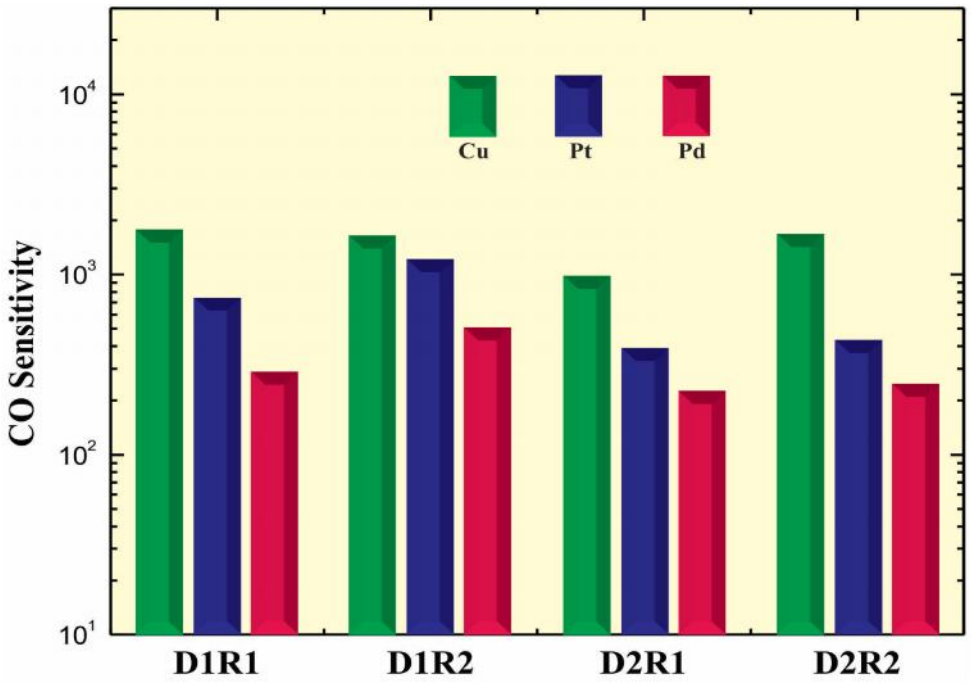

Fig. 4.25. Synthesis routes (R1 and R2) and doping methods (D1 and D2) comparison of Cu, Pt and Pd: SnO_2 CO gas sensitivities.

4.2.5.1 Gas sensing mechanism discussion

Generally, the n-type conductivity in SnO2 is due to the oxygen vacancies derived from the typical stoichiometric defects of the material [52]. With increase in temperature, atmospheric oxygen leads to its adsorption by accepting electrons from the surface of SnO_2. Oxygen will adsorb in the form of molecular (O^-_2) below 150 ^{0}C and atomic (O^- and O^{2-}) ions more than 150 ^{0}C which are more reactive than the molecular species. This adsorption leads to the formation of an electron depleted region near the surface of the SnO_2 particle. The electron depleted region which is an area of less conductance, also called the space-charge layer [52], when exposed to a reducing gas like CO, surface reactions like equations (4.9) and (4.10), release electrons back to the SnO_2 and lead to an increase in the conductance of the space charge layer.

$$CO + O^-_{ads} \rightarrow CO_2 + e^- \quad (4.9)$$

$$2CO + O^-_{2,\,ads} \rightarrow 2CO_2 + e^- \quad (4.10)$$

As the CO gas concentration increases, the number of reactions with the pellet surface will also increase, which in turn increases the magnitudes of conductance and sensitivity. Also, the oxygen species adsorbed at higher temperatures 300 ^{0}C, are atomic and more reactive, the sensitivity will be higher at 300 ^{0}C than 100 and 200 ^{0}C temperatures. Therefore, sensitivity increases with increase in the gas concentration and temperature which is in consistent with our results reported in Figs. 4.23 and 4.24. From the SEM and HRTEM results obtained, it is evident that the structure obtained are non-spherical and porous, which provides an additional active sites to adsorb more oxygen species for the sensitive reaction [54]. Fig. 4.26 below shows the difference between the contact area for spherical and the non-spherical contacts. For illustration purpose, considering the non-spherical structures formed are tetragonal, results in a different contacting form with different contact area.

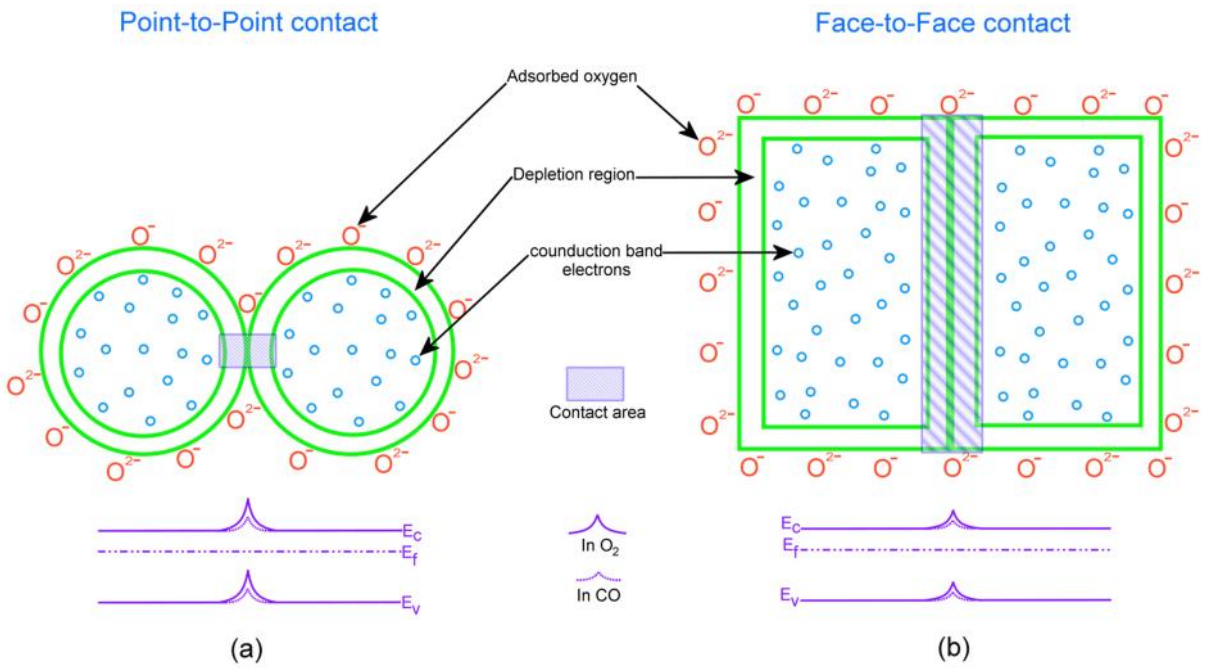

Fig.4.26. Illustration of the contact area for (a) spherical grains and (b) tetragonal grains.

As shown in Fig. 4.26a, for spherical structures with point-to-point contacting, the contact area is less compared to the tetragonal structures with the face-to-face contacting as shown in Fig. 4.26b. Contact area is one of the key parameter to determine the gas-sensing performances. When different tetragonal particles are exposed to air, oxygen adsorption between the face-to-face contacts is difficult compared to the point-to-point contact, resulting

in a less resistive depletion region between the adjacent particles obtained from the face-to- face contacting form. The face-to-face contacting form of tetragonal particles enhances the surface-depletion control rather than grain boundary barrier control, which results in a high sensitivity. Compared state of art of the SnO_2 based sensors [30, 37, 54, 55, 56, 57, 58], the CO sensitivity obtained in this work are improved.

The doping method D1 comprise of primary bulk doping and later ball milling of the bulk doped powders. It was established that introduction of special doping micro-additives of various impurities into metal oxides during their synthesis could sufficiently decrease the particle size and improve both sensor response and thermal stability of the grain size [59, 60].

In case of bulk doping, due to incorporation of additives in the lattice of metal oxide can change the charge carries concentration with corresponding influence on the bulk conductivity and the thickness of the space charge region. This effect is clearly observed from our SEM results. From Figs. 4.16a, 4.16b, 4.17a and 4.17c, we observe the grains formed are connected with their necks which increases the conductivity of the pellets doped by method D1 than D2. Also in case of method D1, the post-annealing of powders and heat produce during the ball milling would have resulted in the grain growth. This grain growth gives rise to two important factors, one is *coalescence* and the other is the *modification of crystal structure* [60, 29].

Due to *coalescence*, we can observe the increase of the contact area between crystallites and the forming of necks between grains. This will lead to formation of a sensor matrix network [61, 62] which was obtained in our results too when the powders were doped by D1 (refer Fig. 4.16a).

Modification of crystallographic structure of material, leads to increase in concentration of crystal defects and also the crystallographic faceting can be changed. From the reported works [63, 64], it was proposed that, these changes would enhance the conductivity of SnO_2 matrix. It is evident from the HRTEM results Figs. 4.19-4.21, that the stacking faults and {221} facets were observed in Cu, Pt and Pd doped SnO_2 crystals. The SnO_2 -based gas sensors are really very sensitive to crystal morphology and depend on the grain faceting the sensitivity varies. It has recently shown by Han et.el [35], that {221} facets show higher sensitivities compared to others.

The necks formation and the structural modifications produced due to bulk doping have enhanced the sensitivity of the SnO_2 pellets doped by method D1. Also the sensitivity of the pellets doped by R1 is higher than R2 because the temperature required to decompose the urea made the resulted particles more uniform than the powders formed by synthesis route R2 [65]. In R2 the precipitation is performed at room temperature which resulted in much larger grains around 500nm (refer Figs. 4.16b and 4.16d), the increase in the grain sizes will decreases the surface to volume ratio and further the sensitivity. Therefore the powders synthesized by route R1 showed higher sensitivities than R2, irrespective of doping method and dopants.

In case of pellets doped by method D2, the powders were pre-annealed and impregnated by dopants and post annealed too, later ball milled the surface doped powders. The pre annealing treatment did not allow the dopants to diffuse into the crystal lattice because, the SnO_2 powders were stabilized during the pre-annealing treatment. This is proved from the SEM and HRTEM results because no necks between the grains (refer Fig. 4.16c) and neither defects in the crystal were observed. The sensitivity in the pellets doped by method D2 is due the formation of clusters on the surface of the SnO_2 crystals (refer Figs. 4.19d and 4.19f). Until now, two types of sensitization mechanisms, chemical and electronic, are considered for assuring the effect of clusters on the sensitivity. The detailed explanation of the both mechanisms have been discussed by many authors in detailed previously [66-68].

In the electronic mechanism, there is only electronic interaction between the semiconductor and cluster and these interactions change depending on the form of cluster. It has been evidenced that the metal clusters like Cu, Pt and Pd in oxide from can only interact electronically with the SnO_2 and these interactions vanishes if the clusters are metallic [68]. Since no oxides were observed from our HRTEM results, electronic mechanism can be ruled out. To the best of our knowledge, until now the previous reports [67,68] suggests that the spillover effect (chemical mechanism) lowers the measuring temperature, which could be the possible reason for the increased sensitivity in method D2 at 200 ^{0}C also (refer Fig. 4.23 and 4.24). Therefore it can be concluded that the sensitivity for the pellets doped by method D2 is due to the spillover effect.

From Fig. 4.25 and Table. 4.5, it is clearly evident that that irrespective of the doping methods and synthesis routes, dopant, Cu showed higher sensitivities than Pt and Pd. This a very interesting and a novel result. One of the most important factor that influence the sensitivity is concentration of the additives. In this work we have utilized 1wt% of concentration in all the cases and for all the dopants. In case of bulk doped pellets, the defects produced in the crystal lattice of SnO_2 by noble metals like Pt and Pd were more compared to Cu. These increase in defect have changed the structure of the crystals and the facets. Due to many changes occurred in the structure of gas sensor matrix, the sensitivity would have decreased compared to Cu doped pellets. In case of impregnated pellets, the 1wt% of Pt and Pd is usually high because it has been established that the response of SnO_2 -based sensors lies in the range of 0.1-0.6% for the noble metals and for the transition metals it is in the range of 1-4% [69-72].

However, as we observed form all the results obtained in this work, we can conclude that the sensitivity depends on many factors like measuring temperature, microstructure, crystallite size, shape, dopants and on the interaction between the sensing matrix and gas molecules. Further work is necessary to find the exact role of transition and noble metal dopants on the CO sensitivity. A comparison of doping methods and synthesis routes used with their corresponding advantages and sensitivities for the Cu-SnO_2 pellets were represented graphically in Fig. 4.27.

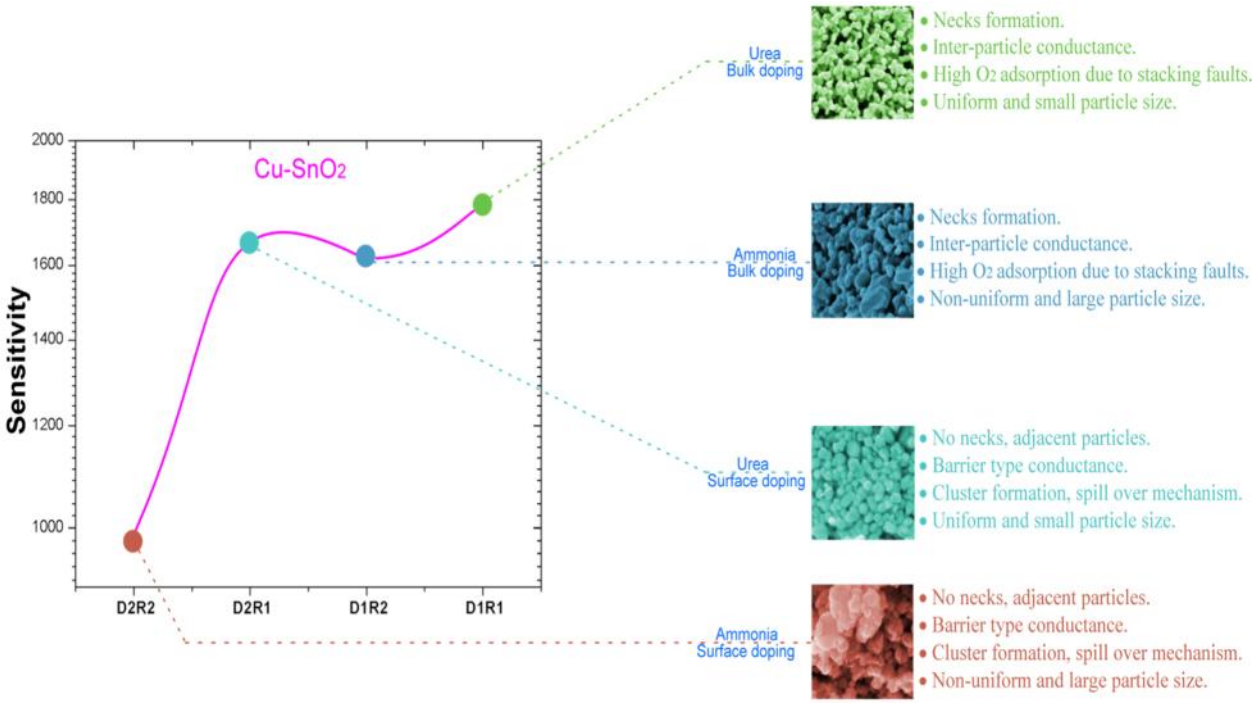

Fig. 4.27. Graphical comparison of doing methods and synthesis routs of Cu-SnO_2 pellets with corresponding intellects for achieving the high sensitivities.

Therefore, Cu, being a transition metal, its doping have produced better magnitudes of sensitivities in this work than noble metal dopants like Pt and Pd, which were the most effective dopants until now. From this result, it can be concluded that, cost effective SnO_2 sensor design is possible with the usage of Cu as a dopant than the Pt and Pd, while having a higher magnitude of CO sensitivity.

4.3. Complementary works

In this section we are going to explain some additional works performed. The main reason for doing these additional works is to improve the sensors sensitivity. First sections explains about the mixing of alumina with tin oxide powders and their sensing properties. The second and third section focuses on the thick films utilizing thermally evaporated silver contacts and fabricated transducer with gold contacts, respectively.

4.3.1. Al_2O_3 mixed SnO_2 pellets

The preparation of Al_2O_3 mixed SnO_2 pellets was explained in section 3.1.4. The main idea for implementing the mixing of alumina is, for creating the porosity in the pellet while saving the main sensor material. Since alumina is a ceramic material, it will not participate

directly in sensing mechanism. The effect of change in alumina ratio on the CO gas sensitivities were plotted in the Fig. 4.28.

For alumina mixed SnO_2 pellets, doesn't show significant changes in the sensitivities when measured at 100 and 200 ^{0}C. As we explained before in section 4.1, at lower temperatures since the adsorbed oxygen species were less reactive, the sensitivity is very low. In Fig. 4.28, the sensitivities plotted were obtained at temperature 300 ^{0}C and for 300 ppm of CO concentration. From this figure, we can observe that, the sensitivities decrease after mixing alumina compared to pure SnO_2 pellets. The maximum sensitivities achieved were around 48 and 34 for pellets prepared by R1 and R2, respectively, and when mixed with ratio 2:1. Sensitivity depends not only on porosity but also on the amount of sensing material.

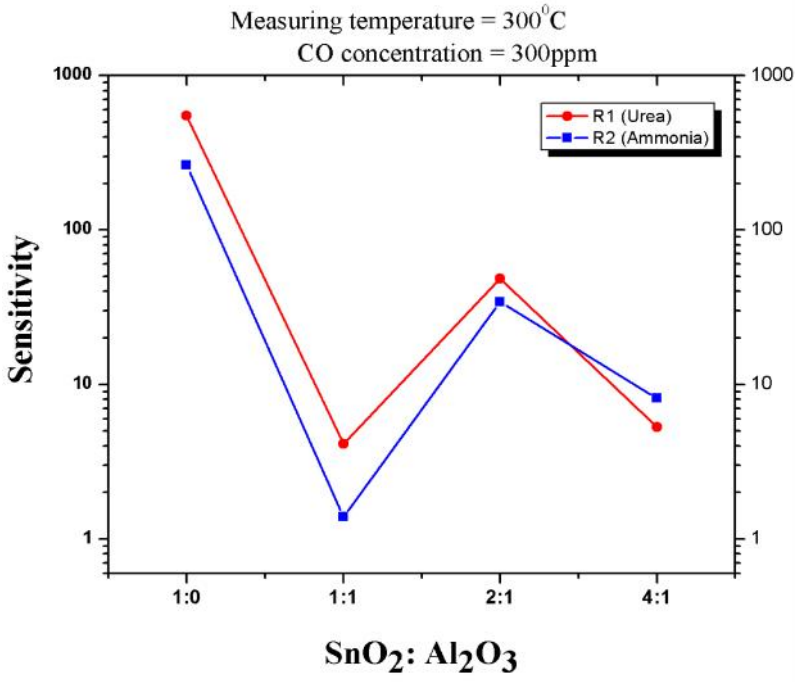

Fig. 4.28. Comparison of sensitivities of SnO_2: Al_2O_3 pellets for different mixing ratios.

SnO_2:Al_2O_3	Quantity of SnO_2 (%)	Porosity (%)
1:0	100	32.30277
1:1	33.33	54.35864
2:1	66.66	74.62565
4:1	83.33	60.01781

Table. 4.6. Porosity and quantity of sensing material in all alumina mixing ratios for powders prepared by R1.

By considering both porosity and quantity of sensing material, we explain the sensitivity changes after mixing with alumina. Calculated %SnO_2 (sensing material) and porosity (for porosity calculation refer section 4.2.1) theoretically in each alumina mixing case and reported in Table. 4.6. Similar results were obtained for powders prepared by R2. Thus form the above observations, theoretical calculations and the sensitivity graphs, a hypothesis arrangement model of SnO_2 and Al_2O_3 atoms on the surface is depicted and shown in Fig. 4.29.
Therefore from Figs. 4.28 and 4.29 and Table. 4.6, the following details can be observed:

- In case of 1:1, sensing material is very less and porosity is less compared to case of 2:1 which may reduce the sensitivity.
- In case of 4:1, porosity is less compared to case of 2:1, thus the oxygen trapping is lesser in 4:1 than 2:1, which would decrease the sensitivity.
- 2:1 is the best case compared to 1:1 and 4:1, where the sensitivity is very high because, availability of enough sensing material and also high porosity compared to all remaining all case, including pure. Oxygen trapping increases due to high porosity.

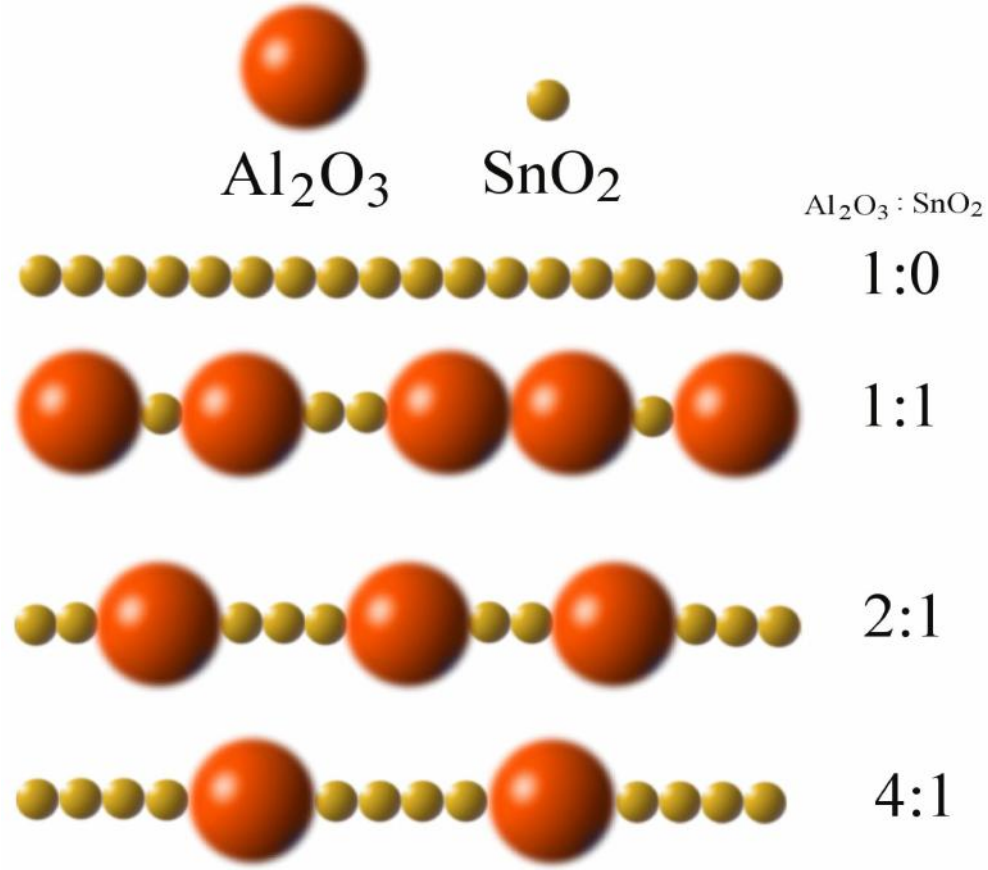

Fig. 4.29. A hypothesis model for an arrangement of SnO_2 and Al_2O_3 particles on the pellets surface for different mixing ratios.

In order to cross check our hypothesis model, we have performed the SEM analysis of the 2:1 mixed pellets surface. Fig.4.30 shows the surface of the alumina mixed tin oxide pellets surface prepared by R1 at different magnifications. From Fig. 4.30a, it can be observed that the SnO_2 particles with particles size around 20nm were homogeneously distributed all over the surface. In Fig. 4.30b, it is observed both the alumina and tin oxide grains, in which, the alumina particles were surrounded by the SnO_2 particles. The size of alumina particles is around 5µm, which is much larger than a SnO_2 particle. From Figs. 4.30c and 4.30d, it is clearly evident that the alumina and tin oxide particles were agglomerated separately. They are not mixed according to our hypothesis. We assume that, this would have resulted due to the pressure applied to manufacture the pellets made all the bigger grains to come closer and together.

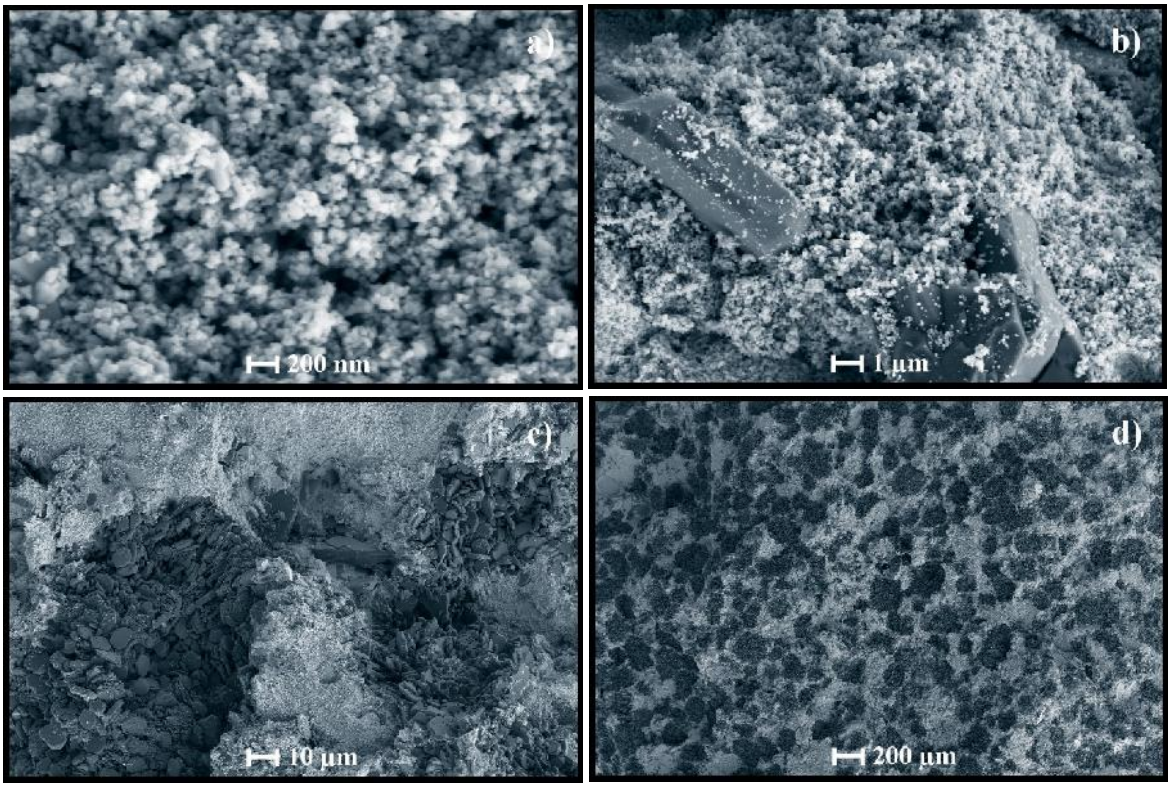

Fig. 4.30. SEM images of SnO_2 and Al_2O_3 mixed pellets surface at magnification of (a) 200nm, (b) 1µm, (c) 10 µm, and (d) 200µm.

Alumina, as a ceramic material, doesn't participate in sensing mechanism, the amount of sensing material in all the alumina mixed tin oxide pellets were decreased, which in turn reduces the sensitivity of the alumina mixed tin oxide pellets sensitivity compared to the pure tin oxide pellets. Hence the adverse effect of the Al_2O_3 mixed SnO_2 pellet sensitivities was a consequence of pellet manufacturing method. Further optimization of manufacturing pressure and pressing time, is necessary to improve the performance of the alumina on the sensor

response. Moreover, the composition of alumina and tin oxide inside the pellets should be analyzed and studied.

4.3.2. SnO_2 thick films utilizing thermally evaporated silver contacts

In this section only a part of the results are discussed. Some more future study and future work is needed to conclude all the results regarding the sensitivity of thick films. In chapter 3, we have explained the method for preparing the thick films. By considering our previous results, the powders prepared by route R1 (urea) showed better sensing results. Therefore, we have considered the powders prepared by R1 to prepare thick films. All the films were deposited on glass substrate and annealed at 250, 350, and 450 ^{0}C to remove the residual components, especially carbon which arises due to the usage if terpineol and ethyl cellulose. In order to find the effect of annealing temperature on the residual components thickness measurements, XRD and SEM analysis were performed.

4.3.2.1. Thickness measurements

The film thicknesses were measured for all the films deposited, by using a P15 KLA TENCOR Profilometer. The equipment details were given in chapter 3. Fig. 4.31 shows the thickness variation of the SnO_2 thick films as a function of the annealing temperature. The film thickness decreased with increase in the annealing temperature, which is due to the removal of residual components in the annealing process. The thicknesses of the 250, 350, 450 ^{0}C annealed samples were around 1319, 824.6, and 538.5 nm, respectively.

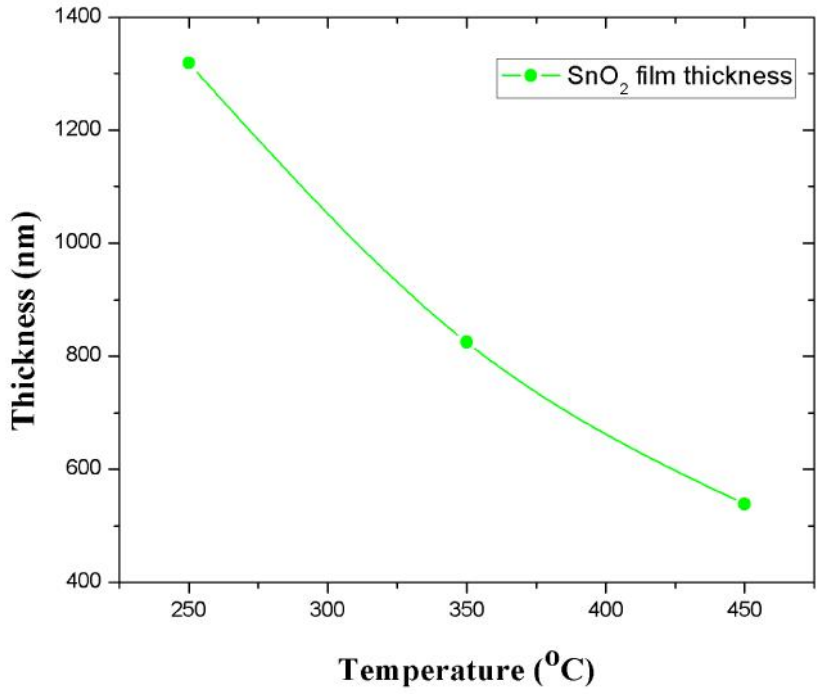

Fig. 4.31. Thickness variation of SnO_2 thick films as a function of the annealing temperature.

4.3.2.2. XRD analysis

Fig. 4.32 shows the XRD patterns of SnO_2 thick films annealed at different temperatures. All the peaks showed in the XRD patterns are indexed to the tetragonal rutile structure of SnO_2 according to the reported data in the JCPDS card (77-0450). Apart from tin oxide, no other additional peaks are available.

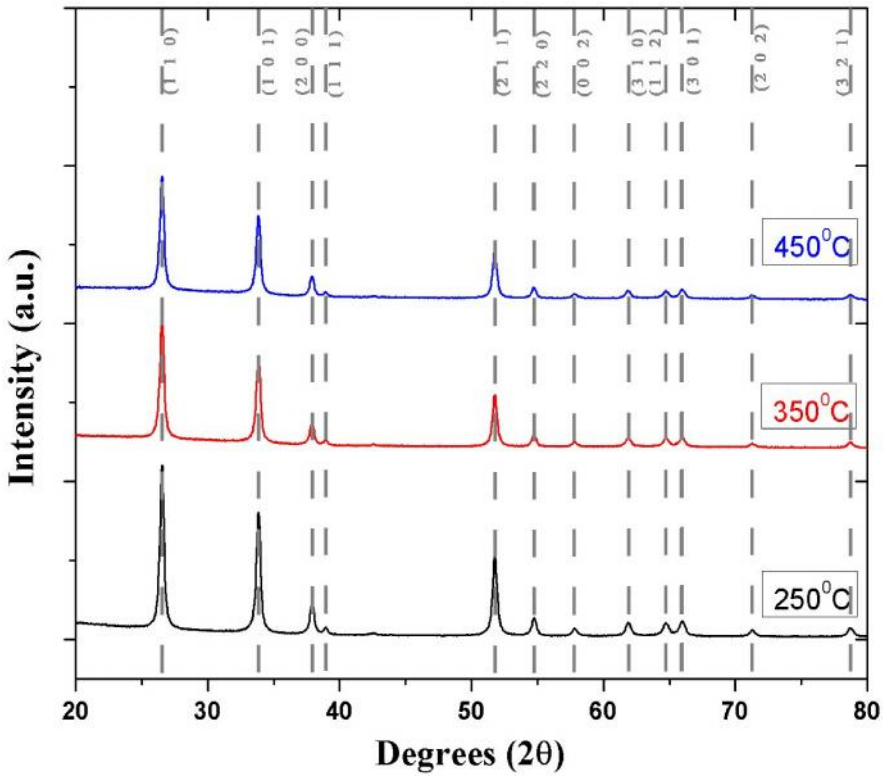

Fig. 4.32. XRD analysis of SnO_2 thick films for different annealing temperatures.

In order to obtain structural information in detail, the patterns are plotted in amplified mode and shown in Fig. 4.33. From Fig. 4.33, it can be observed that intensity of the peaks decreases with increase in the annealing temperature. The XRD peak intensity depends on the quantity of material. As the annealing temperature increases, the amount of residual solvents used will evaporate, which decreases the quantity of material and also decreases the peak intensity. From this it can be reasoned out that, the solvents used to prepare the SnO_2 thick films did not affect any structural properties of the films.

Since the thick films will be used for CO gas sensing, it is important to observe the surface morphology of the films. SEM and EDAX analysis were performed to observe the surface morphology and composition of the films.

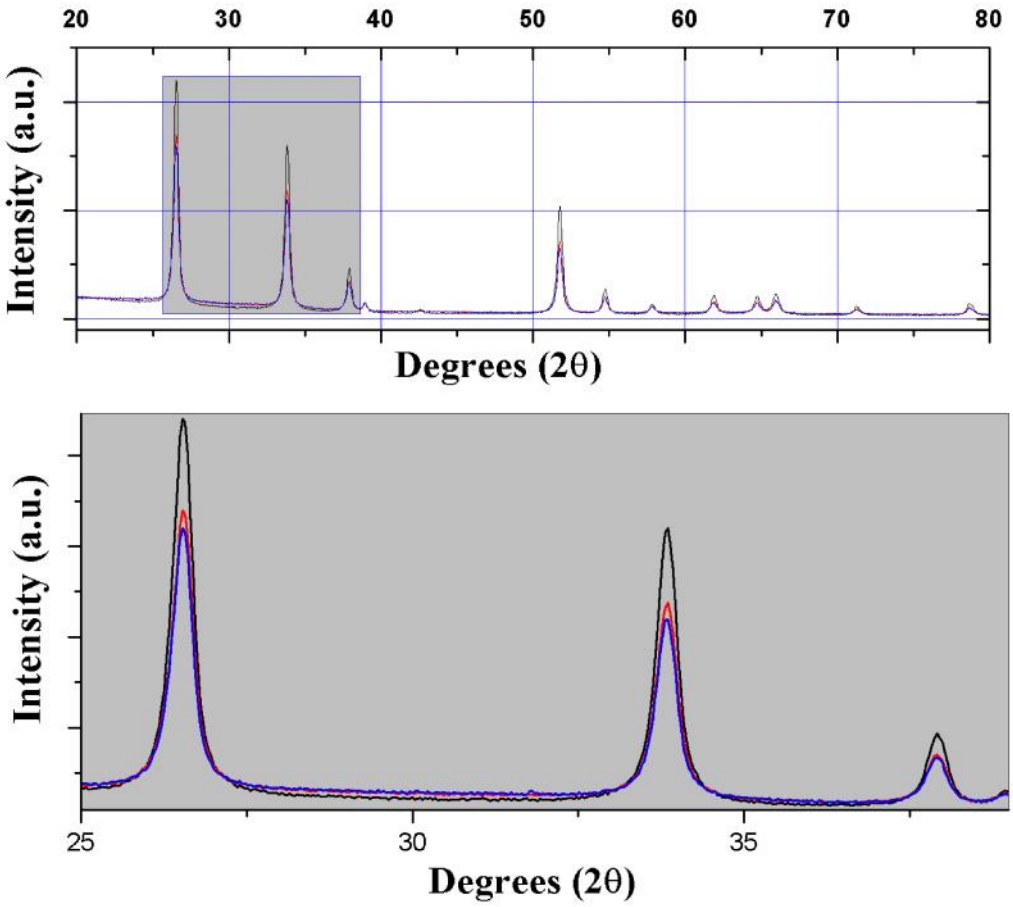

Fig. 4.33. XRD analysis of SnO_2 thick films for different annealing temperatures plotted in zoom mode.

4.3.2.3. SEM and EDAX analysis

Fig. 4.34 shows the SEM images and the corresponding composition analysis of annealed SnO_2 thick films. From Figs. 4.34a, c and e, it is evident that the film porosity increases with increase in the annealing temperature due to the evaporation of carbon content. The evaporation of carbon content is confirmed by the composition analysis as shown in Figs. 4.34b, d, and f. We can observe distinctly both the carbon peak decrement and tin peak increment with increase in the annealing temperature.

Also it can be observed from the SEM images that the morphology has many significant changes. Agglomeration and some pin holes have been observed on the surface with increased in the annealing temperature.

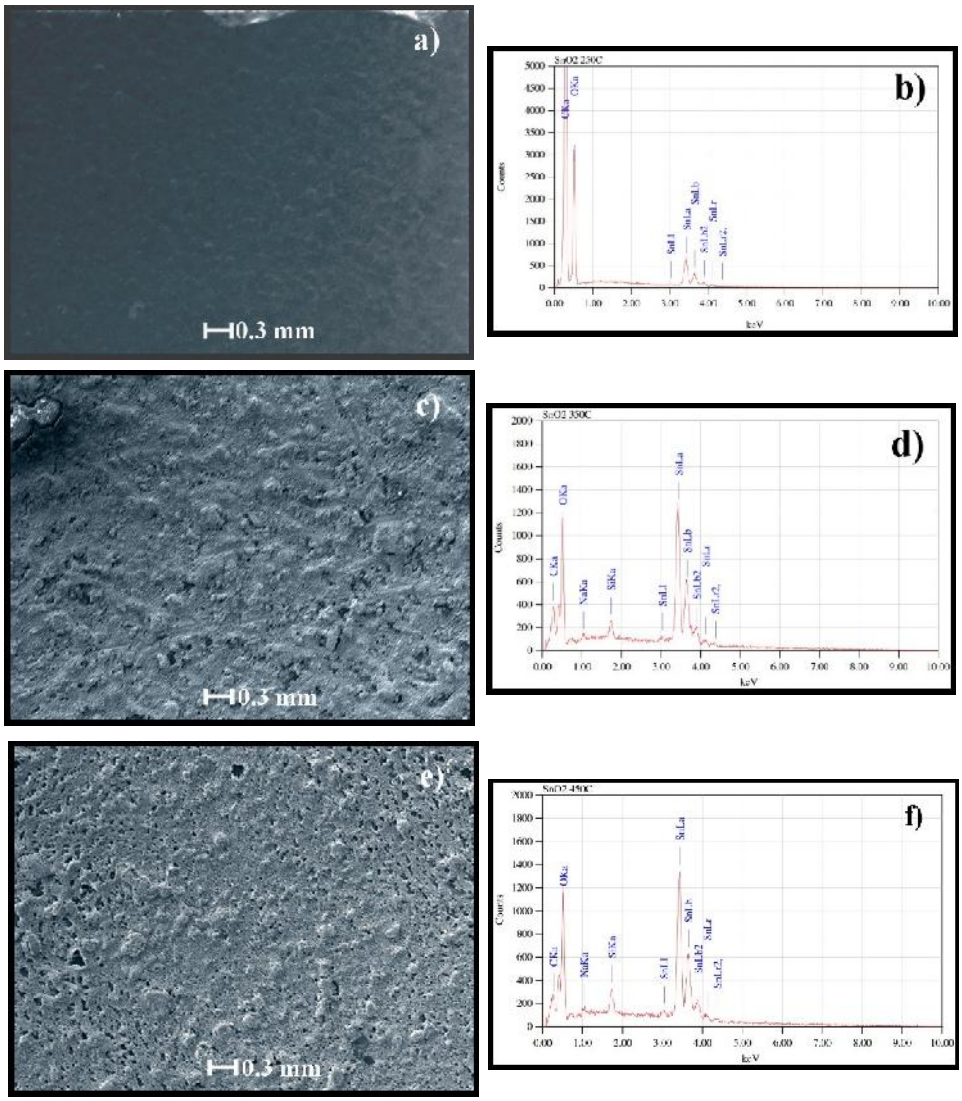

Fig. 4.34. SEM and corresponding EDAX images of SnO_2 films annealed at (a) and (b) 250 ^{0}C, (a) and (b) 350 ^{0}C, and (a) and (b) 450 ^{0}C.

By comparing, thickness measurements, XRD, SEM and compositional analysis, it's apparent that the films deposited at 450 ^{0}C are more suitable for gas sensing because they are more porous, less carbon content and thinner compared to other films. Therefore the sensitivity measurements were performed for the films annealed at 450 ^{0}C.

4.3.2.4. Sensing measurements

Fig. 4.35 shows the sensitivity with respect to the CO gas concentration of the SnO_2 thick films prepared by R1 and annealed at 450 ^{0}C. Similar to the previous results, the sensitivity increases with increase in both gas concentration and the measuring temperature. As the gas

concentration increases the number molecules available for reaction increases which in turn increases sensitivity [73]. As the temperature increases the form oxygen adsorbed are more reactive [73], which results in high sensitivities at higher temperatures. The maximum sensitivity obtained is around 30, when measured at 300 ^{0}C and at 300 ppm. The sensitivity of the films is very less compared to the pellets, which may be due to less sensing material and less porosity compared to the pellets. Further optimization of annealing temperature, annealing time, and utilization of improved deposition techniques, is necessary to improve the performance of the thick films on the sensor response. Further work includes, obtaining additional results regarding the different annealing times (higher and lower than 1 h), doping the films (Cu, Pt and Pd) and their CO gas sensing performance.

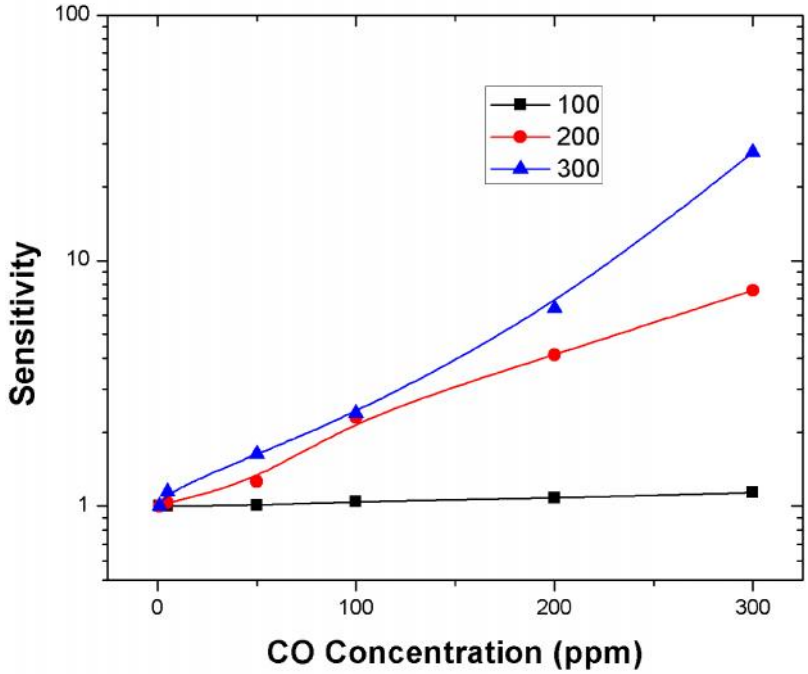

Fig. 4.35. Sensitivity of SnO_2 thick films prepared by R1, and annealed at 450 ^{0}C.

4.3.3. SnO_2 thick films utilizing fabricated transducer with gold contacts

All the undoped, doped, alumina mixed SnO_2 pellets, and SnO_2 thick films prepared in this work until now contains silver contacts deposited by thermal evaporation technique. In order to test the sensing efficiency of our material with globally available transducers, we have utilized a transducer with gold (Au) contacts fabricated at School of Electrical and Computer

Engineering, RMIT University, Australia [74]. The transducer schematic model is shown in Fig. 4.36.

SnO_2 thick film has been deposited on the gold electrodes by using Doctor-Blade method and annealed at 450 ^{0}C to remove the residual components. The thickness of the film measured by using profilometer was around 450nm. Figs. 4.37 and 4.38 shows the SEM and corresponding EDAX analysis respectively of the SnO_2 thick film deposited on the gold electrodes.

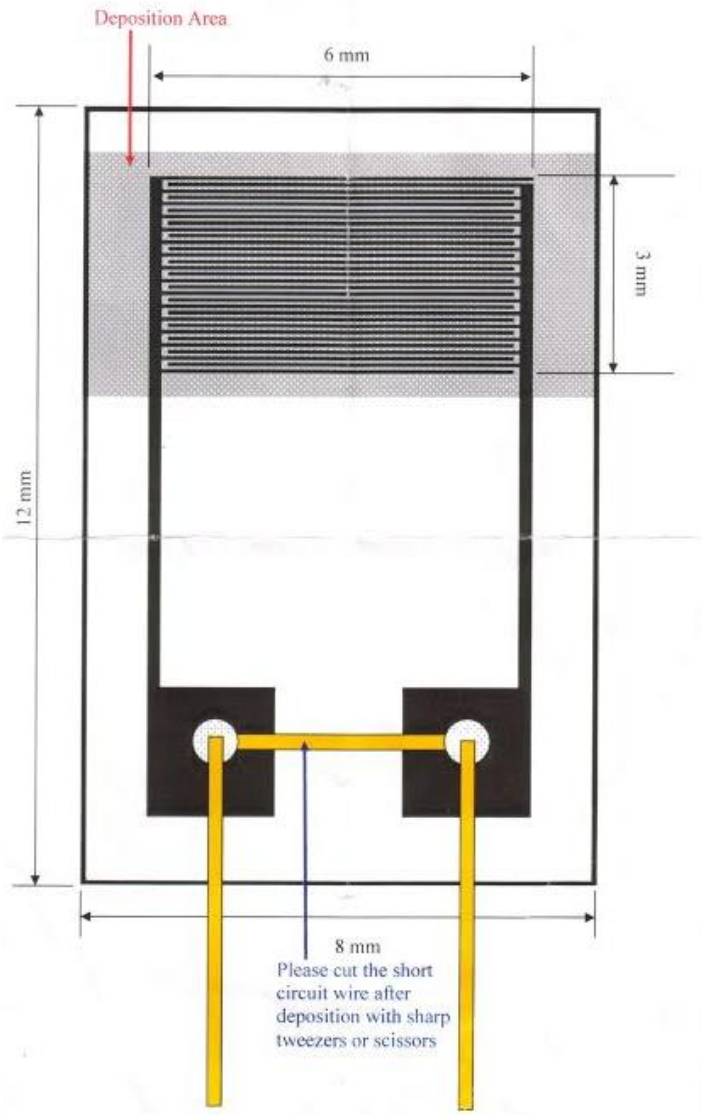

Fig. 4.36. Schematic model of the transducer with the gold contacts.

Fig. 4.37 shows the surface of the thick films deposited on gold contacts at different magnifications. From Fig. 4.37a, it is evident, the particle size distribution was around 25-62 nm. The particle size distribution is homogeneous all around the sample which is confirmed by Figs. 4.37b ad 4.37c. Also from these figures we can say that the films surface is porous, which is favorable for gas sensing. Fig. 4.37d, shows the SnO_2 film and the gold contacts too. From Fig. 4.37d, we observe the agglomeration of the particles and forms bigger clusters. The compositional analysis of the film surface is shown in Fig. 4.38a-d.

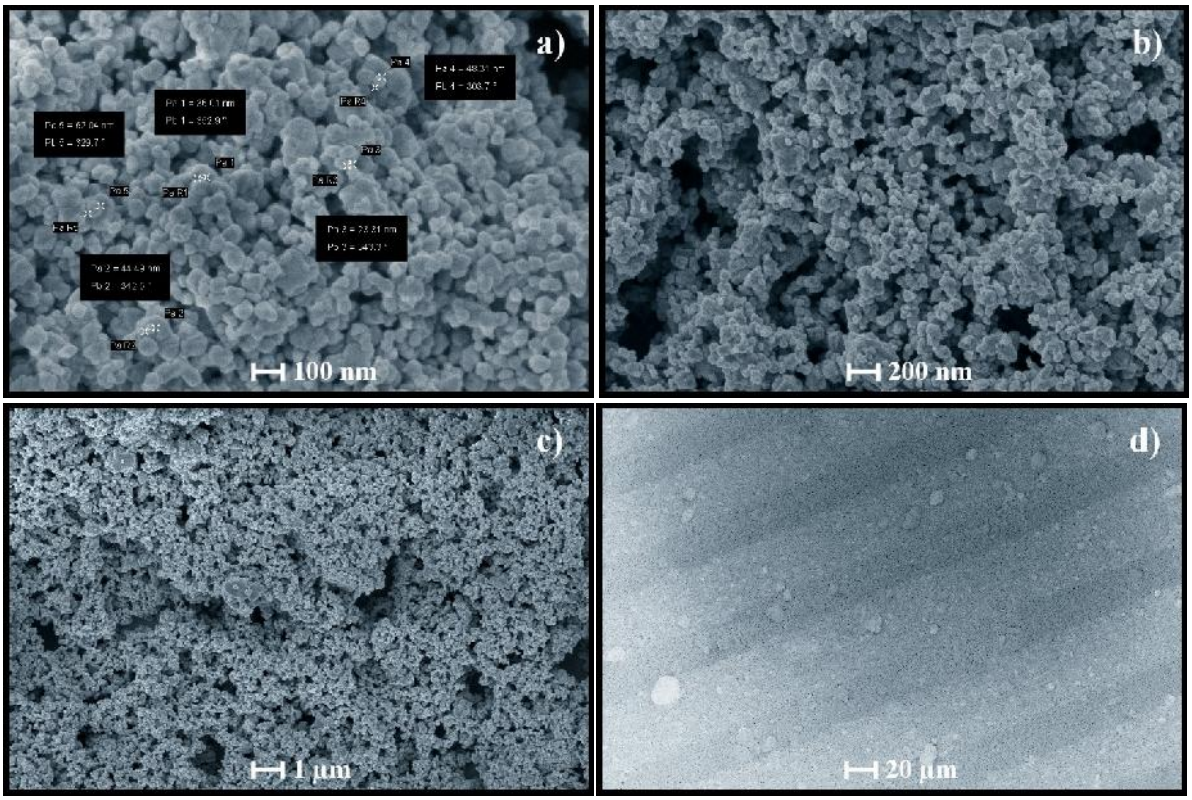

Fig. 4.37. SEM images of SnO_2 thick film on the gold contacts at magnification of (a) 100 nm, (b) 200 nm, (c) 1 µm, and (b) 20 µm.

It is evident the presence of Au, Sn, O from Fig. 4.38. The silicon and carbon peaks in Fig. 4.38d, arises from the glass substrate. From Fig. 4.38b, it can be observed that, the Sn and O were homogenously distributed all over the film. From SEM and EDAX analysis, we can conclude that, homogeneous films with nano particles were successfully deposited by cost effective technique. Nano metric particle size and slight porosity exhibited by the films are very favorable conditions for gas sensing. The sensitivity of the films deposited on Au contacts in CO atmosphere is shown in Fig. 4.39. From the Fig. 4.39, it is observed that the sensitivity increases with respect to CO gas concentration and measuring temperature, which coincides with the general sensor theory [75]. The reasons were already explained in section 4.1.4.

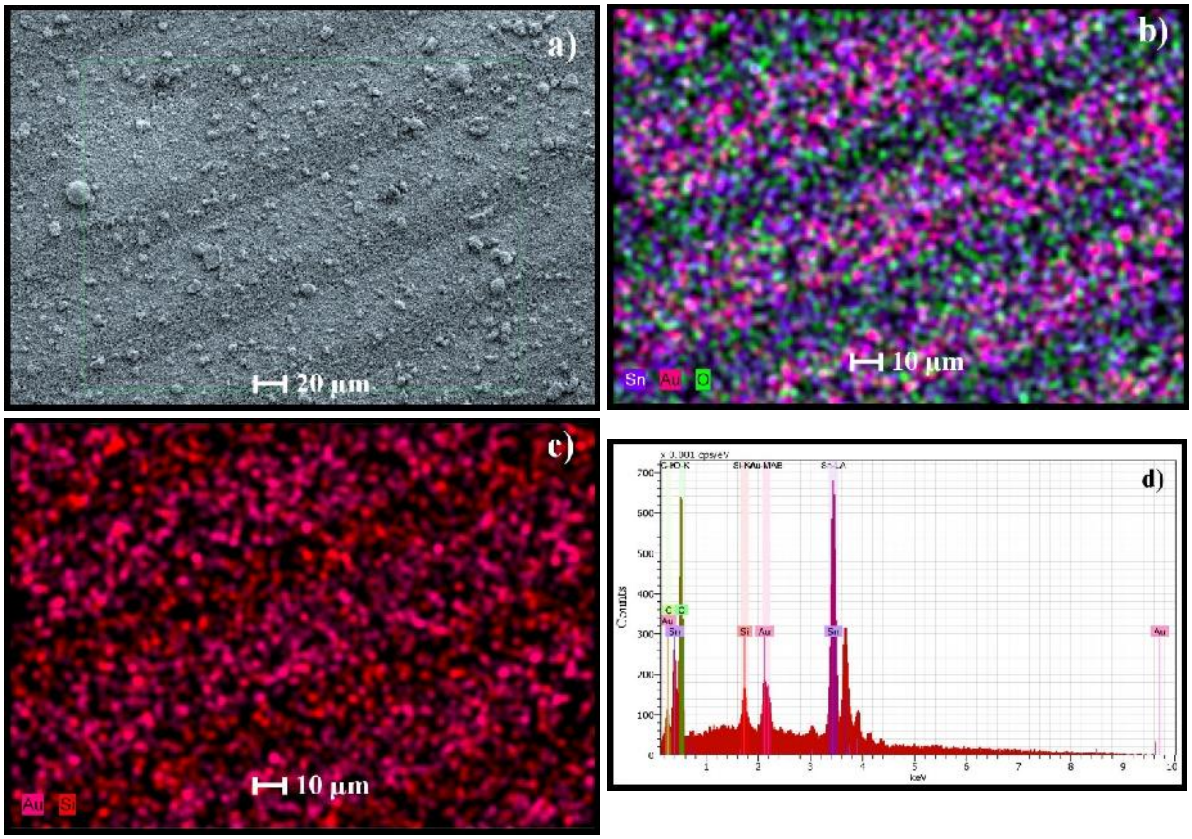

Fig. 4.38. EDAX analysis of (a) SnO_2 films surface with clusters deposited on gold contacts (b) Sn, Au and O, (c) Au and Si compositions, and (d) composition plot.

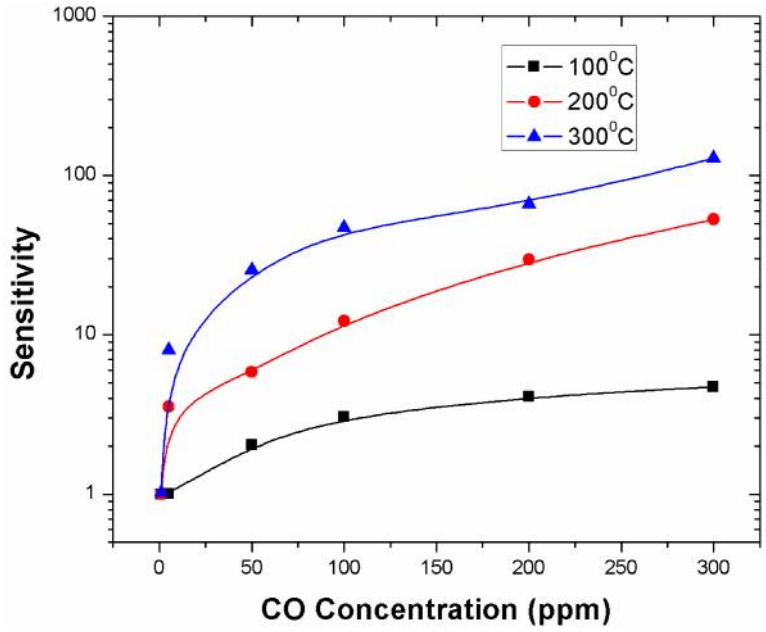

Fig. 4.39. Sensitivity of SnO_2 thick films deposited on gold contacts, and annealed at 450 ^{0}C.

The maximum sensitivity obtained was around 100 when measured at 300 ^{0}C and at 300ppm. Interesting result about this film is, there is a sensitivity at lower temperatures, 100 ^{0}C, too. The sensitivities when measured at 300 ppm at 100 and 200 ^{0}C were around 4.7 and 52. When compared to thick films deposited with silver contacts there was notable sensitivities at lower temperatures. There reduction of sensors operation temperature was achieved for the films with gold contacts. On the other hand the maximum sensitivity obtained is less compared to pellets, which may be due to availability of less sensing material in films.

In future, the reason for the reduction of sensor operation temperature in this case should be studied more by depositing films with different conditions like deposition temperature and time, and also with doped SnO_2 materials. Until now, from the results obtained in our work, the highest sensitivities were achieved for pellets are at higher temperatures but the thick films show sensor response at lower operating temperatures too. The next section resumes out all the sensitivities values in each case.

4.4. A comparison of all SnO_2 sensors prepared in this work

Table. 4.7 below shows a comparison of CO sensitivities with corresponding reasons for sensitivity for undoped, Cu, Pt and Pd doped, Alumina mixed SnO_2 pellets, and the thick films with silver and gold contacts. The reasons explained in the below table are determined by the results obtained in this work. From this table we observe that, pellets show higher sensitivities than films due to the presence of high quantity of sensing material. Cu doped SnO_2 pellets show highest sensitivities than remaining all, due to its comparable ionic radius with tin and the wt% used for doping employed. This makes the sensors manufacturing cost effective. Films deposited on gold contacts show high sensitivities than other films. Also decrease in the sensors optimum measuring temperature was obtained for these films.

	SnO_2 type		CO sensitivity	Reasons	
Pellets	Undoped -R1		548	Homogeneous and small particle size	
	Undoped -R2		262	Non homogenous and large particle size	
	D1R1	Cu: SnO_2	1782	• Comparable ionic radius to Sn	• Necks formation. • Inter-particle conductance. • High O_2 adsorption due to stacking faults. • Uniform and small particle size.
		Pt: SnO_2	1200	• Higher ionic radius than Sn	
		Pd: SnO_2	502	• Very high ionic radius comparable to Sn, Cu and Pt	
	D1	Cu: SnO_2	1625	• Comparable ionic radius to Sn	• Necks formation.

		Pt: SnO_2	721	• Higher ionic radius than Sn	• Inter-particle conductance. • High O_2 adsorption due to stacking faults. • Non-uniform and large particle size.
		Pd: SnO_2	287	• Very high ionic radius comparable to Sn, Cu and Pt	
	D2R1	Cu: SnO_2	1666	• Comparable ionic radius to Sn	• No necks, adjacent particles. • Barrier type conductance. • Cluster formation, spill over mechanism. • Uniform and small particle size.
		Pt: SnO_2	428	• Higher ionic radius than Sn	
		Pd: SnO_2	245	• Very high ionic radius comparable to Sn, Cu and Pt	
	D2R2	Cu: SnO_2	975	• Comparable ionic radius to Sn	• No necks, adjacent particles. • Barrier type conductance. • Cluster formation, spill over mechanism. • Non-uniform and large particle size.
		Pt: SnO_2	387	• Higher ionic radius than Sn	
		Pd: SnO_2	224	• Very high ionic radius comparable to Sn, Cu and Pt	
	SnO_2: Al_2O_3 -R1		48	• Uniform particle size • Agglomeration alumina and SnO_2	
	SnO_2: Al_2O_3 -R2		34	• Non uniform particle size • Agglomeration alumina and SnO_2	
Thick films	Thermally evaporated silver contacts		30	• Less sensing material • Thermally evaporated silver contacts	
	Deposited on fabricated gold contacts		100	• Less sensing material • Clean room fabricated Gold contacts	
R1 and R2 - Urea and ammonia as precipitation agents D1 and D2 – Bulk and surface doping methods					

Table. 4.7. A comparison of CO sensitivities for all the pellets and thick films with their corresponding reasons for sensitivity.

References

[1] Ki Chang Song and Yong Kang, “Preparation of high surface area tin oxide powders by a homogeneous precipitation method”, Materials Letters, vol.42, pp.283–289, Jan.2000.

[2] H.H. Willard and N.K. Tang, “A Study of the Precipitation of Aluminum Basic Sulfate by Urea”, J. Am. Chem. Soc., vol.59, no.7, pp.1190–1196, Jul.1937.

[3] Dae-Wook Kim, Seong-Geun Oh and Jong-Dae Lee, “Preparation of ultrafine Monodispersed Indium-Tin Oxide Particles in AOT-Based Reverse Microemulsions as Nanoreactors”, Langmui, vol.15, pp.1599-1603, Jan.1999.

[4] Ozge Acarbas, Ender Suvaci and Aydın Dogan, “Preparation of nanosized tin oxide (SnO_2) powder by homogeneous precipitation”, Ceramics International, vol.33, no.4, pp.537–542, May 2007.

[5] Pan X.Q. and Fu L, “Oxidation and phase transitions of epitaxial tin oxide thin films on (012)(1̄012) sapphire”, J. Appl. Phys., vol.89,no.11, pp.6048 – 6055, Jun.2001.

[6] Shek C.H.; Lai J.K.; Lin G.M. and Zheng Y.F, “Nanomicrostructure, chemical stability and abnormal transformation in ultrafine particles of oxidized tin”, J. Phys. Chem. Solids, vol.58, no.1, pp.13 – 17, Jan.1997.

[7] J Z Jiangy, R Liny, W Linz, K Nielsenx, S Mørupy, K Dam-Johansenz and R Clasenk, “Gas-sensitive properties and structure of nanostructured materials prepared by mechanical alloying”, J. Phys. D: Appl. Phys., vol.30, no.10, pp.1459–1467, May 1997.

[8] H. Taib and C.C. Sorrell, “Synthesis of Tin Oxide (SnO_2) by Precipitation”, Materials Science Forum, vols. 561-565, pp.969-972, Oct.2007.

[9] Matthias Batzill, Sensors. 6, 1345 (2006).

[10] J. Oviedo, M.J. Gillan, Surface Science. 463, 93 (2000).

[11] Imtiaz Sirajuddin Mulla, Niranjan Suryakant Ramgir, Young Kyu Hwang, and Jong-San Chang, “Semiconductor Tin Oxide Gas Sensors: From Bulk to Thin Films”, J. Ind. Eng. Chern., Vol. 10, No.7, (2004) 1242-1256.

[12] N. Yamazoe, J. Fujigami, M. Kishikawa, and T.Seiyama, Surf Sci., 335, 86 (1979).

[13] Haines, J. and Léger, J. M.. X-ray diffraction study of the phase transitions and structural evolution of tin dioxide at high pressure:ffRelationships between structure types and implications for other rutile-type dioxides. Phys. Rev. B. 55, 11144 (1997).

[14] Giri, P. K. et al. Correlation between microstructure and optical properties of ZnO nanoparticles synthesized by ball milling. J. Appl. Phys. 102, (2007).

[15] Patterson, A. L., The Diffraction of X-Rays by Small Crystalline Particles. Phys. Rev. 56, 972 (1939).

[16] Bernard Dennis Cullity, Elements of X-ray diffraction. 2nd edition Addison-Wesley Publishing Company. (2015).

[17] Dar, M. A., Batoo, K. M., Verma, V., Siddiqui, W. A. & Kotnala, R. K. Synthesis and characterization of nano-sized pure and Al-doped lithium ferrite having high value of dielectric constant. J. Alloy. Compd. 493, 553–560 (2010).

[18] Shannon, R. D. Revised effective ionic radii and systematic studies of interatomic distances in halides and chalcogenides. Acta Crystallogr. Sect. A: Cryst. Physics, Diffraction, Theor. Gen. Crystallogr. 32, 751–767 (1976).

[19] Jarzebski, Z. M. & Marton, J. P. Physical Properties of SnO2 Materials: I . Preparation and Defect Structure. J. Electrochem. Soc. 123, 199–205 (1976).

[20] Traylor, J. G., Smith, H. G., Nicklow, R. M., and Wilkinson, M. K. Lattice Dynamics of Rutile. Phys. Rev. B. 3, 3457 (1971).

[21] Srinivas, K., Vithal, M., Sreedhar, B., Raja, M. M. & Reddy, P. V. Structural, Optical, and Magnetic Properties of Nanocrystalline Co Doped SnO2 Based Diluted Magnetic Semiconductors. J. Phys. Chem. C 113, 3543–3552 (2009).

[22] Katiyar, R. S. Dynamics of the rutile structure. I. Space group representations and the normal mode analysis. J. Phys. C: Solid State Phys. 3, (1970).

[23] Wang, W., Xu, C., Wang, G., Liu, Y. & Zheng, C. Synthesis and Raman scattering study of rutile SnO2 nanowires. J. Appl. Phys. 92, 2740–2742 (2002).

[24] Azam, A., Ahmed, A. S., Habib, S. S. & Naqvi, A. H. Effect of Mn doping on the structural and optical properties of SnO2 nanoparticles. J. Alloy. Compd. 523, 83–87 (2012).

[25] Karthik, T. V. K. ;Maldonado, A. ;de la L. Olvera, M. ;. S Manufacturing of tin oxide pellets and their application

for CO and C_3H_8 gas sensors. in CCE 402–406 (2013).
[26] Fliegel, W., Behr, G., Werner, J. & Krabbes, G. Preparation, development of microstructure, electrical and gas-sensitive properties of pure and doped SnO2 powders. 19, 474–477 (1994).
[27] Matsuura, Y. & Takahata, K. Stabilization of SnO2 sintered gas sensors. Sensors Actuators B: Chem. 5, 205–209 (1991).
[28] Lifshitz, I. M. & Slyozov, V. V. The kinetics of precipitation from supersaturated solid solutions. J. Phys. Chem. Solids 19, 35–50 (1961).
[29] Korotcenkov, G. et al. Faceting characterization of tin dioxide nanocrystals deposited by spray pyrolysis from stannic chloride water solution. Thin Solid Films 471, 310–319 (2005).
[30] Liu, Y., Dong, J. & Liu, M. Well-Aligned "Nano-Box-Beams" of SnO2. Adv. Mater. 16, 353–356 (2004).
[31] Zhong, Z., Yin, Y., Gates, B. & Xia, Y. Preparation of Mesoscale Hollow Spheres of TiO2 and SnO2 by Templating Against Crystalline Arrays of Polystyrene Beads. Adv. Mater. 12, 206–209 (2000).
[32] McAleer, J. F., Moseley, P. T., Norris, J. O. W. & Williams, D. E. Tin dioxide gas sensors. Part 1.—Aspects of the surface chemistry revealed by electrical conductance variations. J. Chem. Soc., Faraday Trans. 1 83, 1323–1346 (1987).
[33] Martinez, C. J., Hockey, B., Montgomery, C. B. & Semancik, S. Porous tin oxide nanostructured microspheres for sensor applications. Langmuir : ACS J. surfaces colloids 21, 7937–7944 (2005).
[34] Batzill, M., Katsiev, K. & Diebold, U. Surface morphologies of SnO2(1 1 0). Surf. Sci. 529, 295–311 (2003).
[35] Han, X. et al. Synthesis of Tin Dioxide Octahedral Nanoparticles with Exposed High-Energy {221} Facets and Enhanced Gas-Sensing Properties. Angew. Chem. 121, 9344–9347 (2009).
[36] Alim, K. A., Fonoberov, V. A., Shamsa, M. & Balandin, A. A. Micro-Raman investigation of optical phonons in ZnO nanocrystals. J. Appl. Phys. 97, (2005).
[37] Zheng, J. G. Dislocations in nanocrystalline SnO_2 thin films. Philos. Mag. Lett. 73, 93–100 (1996).
[38] http://crescentok.com/staff/jaskew/isr/chemistry/class18.htm
[39] Donald D. Wagman, William H. Evans, Vivian B. Parker, Richard H. Schumm, Iva Halow, Sylvia M. Bailey, Kenneth L. Churney, and Ralph L. Nuttall, J. Phvs. Chem. Ref. Data. Vol. 11. Suaal. 2. 1982.
[40] J. c. Chaston, Platinum Metals Rev., 1964, 8, 2, 50-54.
[41] Thorbjorn M. Pedersen, Wei Xue Li and Bjørk Hammer, Phys.Chem.Chem.Phys., 2006, 8, 1566–1574.
[42] Yongfu zhu, Kouji mimura, Jae-won lim, Minoru isshiki, and Qing jiang, Metallurgical and materials transactions A, Volume 37A, April 2006, 1231-1237.
[43] P. J. Moller, M. -C. Wu: Surf. Sci. 250, 265 (1989).
[44] U. Diebold, J. -M. Pan, T. E. Madey: Surf. Sci. 287/288, 896 (1993).
[45] P. J. Moller: Science of Ceramic Interfaces II, J. Nowotny (ed.), pp. 473-526. Amsterdam: Elsevier 1994.
[46] C. R. Henry, C. Chapon, C. Duriez, S. Giorgio: Surf. Sci. 253, 177 (1991).
[47] S. H. Overbury, P. A. Bertrand, G. A. Somorjai: Chem. Rev. 75, 547 (1975).
[48] G.E. Poirier, R.E. Cavicchi, S. Semancik, Particle growth of palladium on epitaxial tin oxide thin films, J. Vac. Sci. Technol. A 12 (1994) 2149.
[49] J. Arbiol, A. Cirera, F. Peiro , A. Cornet, J.R. Morante, J.J. Delgado, J.J. Calvino, Optimization of tin dioxide nano sticks faceting for the improvement of palladium nanocluster epitaxy, Appl. Phys. Lett. 80 (2002) 329.
[50] T.B. Freyberger, J.W. Erickson, S. Semancik, Chemical and electronic properties of Pd/SnO_2 (1 10) model gas sensors, Surf. Interf. Anal. 14 (1989) 83.
[51] Tangirala, V. K. K., Maldonado-Alvarez, A. & de la Luz Olvera, M. Synthesis of tin oxide powders by homogeneous precipitation. Structural and morphological characterization. In CCE 1–7 (2012).
[52] J. Arbiol, R. Diaz, A. Ciera, F. Peiro, A. Cornet, J.R. Morante, F. Sanz, C. Mira, J.J. Delgado, G. Blanco, J.J. Calvino, Effects of in-situ and ex-situ reduction of Pd/SnO2 studied by HRTEM, Inst. Phys. Conf. Ser. 169 (2001) 73.
[53] Nicolae Barsan and Udo Weimar. Journal of Electroceramics. 7, 143-167 (2001).
[54] Lee, J.-H. Gas sensors using hierarchical and hollow oxide nanostructures: Overview. Sensors Actuators B: Chem. 140, 319–336 (2009).

[55] Camargo, P. H. C., Satyanarayana, K. G. & Wypych, F. Nanocomposites: synthesis, structure, properties and new application opportunities. Mater. Res. 12, 1–39 (3AD).
[56] Vasu, V. & Subrahmanyan, A. Physical properties of sprayed SnO2 films. Thin Solid Films 202, 283–288 (1991).
[57] Fang, G. et al. Preparation of SnO2-CuO nanocrystalline powders in two different ways by the sol-gel method. Phys. Status solidi 156, 15–22 (1996).
[58] Song, K. C. & Kang, Y. Preparation of high surface area tin oxide powders by a homogeneous precipitation method. Mater. Lett. 42, 283–289 (2000).
[59] Smatko, V., Golovanov, V., Liu, C. C., Kiv, A., Fuks, Donchev,D., Ivanovskaya, I. M. Structural stability of In_2O_3 films as sensor materials. J MATER SCI-MATER ELECTRON. 21, 360-363 (2010).
[60] Korotcenkov, G. Gas response control through structural and chemical modification of metal oxide films: state of the art and approaches. Sensors Actuators B: Chem. 107, 209–232 (2005).
[61] Korotcenkov, G. Metal oxides for solid-state gas sensors: What determines our choice? Mater. Sci. Eng. B 139, 1–23 (2007).
[62] Korotcenkov, G. Practical aspects in design of one-electrode semiconductor gas sensors: Status report. Sensors Actuators B: Chem. 121, 664–678 (2007).
[63] Wang, N., Cai, Y. & Zhang, R. Q. Growth of nanowires. Mater. Sci. Eng. R: Reports 60, 1–51 (2008).
[64] Gryaznov, V. G. & Trusov, L. I. Size effects in micromechanics of nanocrystals. Prog. Mater. Sci. 37, 289–401 (1993).
[65] Mulla, I. S., Ramgir, N. S., Hwang, Y. K. & Chang, J.-S. Semiconductor Tin Oxide Gas Sensors: From Bulk to Thin Films. J. Ind. Eng. Chem. 10, 1242–1256 (2004).
[66] Brinzari, V., Korotcenkov, G., Schwanka, J., Boris, Y. CHEMISORPTIONAL APPROACH TO KINETIC ANALYSIS OF SnO_2:Pd-BASED THIN FILM GAS SENSORS. Journal of Optoelectronics and Advanced Materials. 4, 147-150 (2002).
[67] Kolmakov, Andrei., Chen, Xihong., Moskovits, Martin Functionalizing Nanowires with Catalytic Nanoparticles for Gas Sensing Application. Journal of Nanoscience and Nanotechnology. 8, 111-121 (2008).
[68] Matsushima, S., Maekawa, T., Tamaki, J., Miura, N. & Yamazoe, N. New methods for supporting palladium on a tin oxide gas sensor. Sensors Actuators B: Chem. 9, 71–78 (1992).
[69] Carreño, N. L. V. et al. The influence of cation segregation on the methanol decomposition on nanostructured SnO2. Sensors Actuators B: Chem. 86, 185–192 (2002).
[70] Tong, M. S., Dai, G. R., Wu, Y. D. & Gao, D. S. High sensitivity and switching-like response behavior of SnO2-Ag-SnO2 element to H2S at room temperature. 11, (2000).
[71] Aragón, F. H. et al. Structural and hyperfine properties of Cr-doped SnO_2 nanoparticles. J. Physics: Conf. Ser. 217, (2010).
[72] Azam, A., Ahmed, A. S., Chaman, M. & Naqvi, A. H. Investigation of electrical properties of Mn doped tin oxide nanoparticles using impedance spectroscopy. J. Appl. Phys. 108, (2010).
[73] Madou, M. J., Roy Morrison, S. Chemical Sensing with Solid State Devices. Elseiver publishers. Chapter 12, (2012).
[74] Provided by Professor Wojciech Wlodarski, Adjunct Professor, Electrical and Computer Eng, RMIT University, Australia.
[75] Ciureanu, P. and Middelhoek, S. Thin Film Resistive Sensors. Institute of Physics, Bristol Peter Rhodes Books. (1992).

CHAPTER -5

CONCLUSIONS

Determinations and endings

General conclusions

- In this work, pure SnO_2, Cu, Pt and Pd doped SnO_2 nanoparticles were successfully synthesized and subsequent pellets were successfully manufactured with all the synthesized powders.
- Alumina mixed SnO_2 pellets, thick films with silver and gold contacts were also prepared in a productive manner.
- The gas sensing properties of all the pellets and thick films in a controlled carbon monoxide (CO) and propane (C_3H_8) atmospheres were successfully obtained.

5.1. Particular conclusions

- The structural, morphological, optical and sensing properties of SnO_2 pellets, as well as thick films, were studied in detail, giving particular attention to the interaction mechanisms between the material and gases.
- Powders prepared using the precipitation agent, urea, were more homogeneous and uniform because it employs temperature controlled synthesis.
- Ball milling is an effective process to reduce the particle size and also promotes coalescence between the particles, which are used as conductive necks between the particles.
- Bulk doping is more effective method for gas sensing applications because the dopants either can enter into the crystal lattice, which promotes the sensing due to defects produced, or also sit on the surface to promote spill over gas sensing mechanism.
- Doping percentage plays an important role according to the dopant metal type. For transition metals like Cu, 1wt% shows high sensitivities, whereas, for noble metals like pt and Pd, 1wt% will worsen the sensitivities.
- Sensors with silver contacts shows higher sensitivities compared to gold contacted sensors, which is due to the higher conductivity of silver at higher temperatures. But is preferable to use gold contacts because of higher corrosive resistance of gold makes the sensor to use for long time.
- Thick films sensitivities are low compared to pellets due to the decrement in the porosity, but low sensor operation temperatures can be achieved by using thick films sensors.

We expect our assertion in this work can demonstrate a viable way for understanding the effect of synthesis routes, doping methods, dopants and other parameters on the SnO_2 sensors.

Generally sensitivity depends on many factors, most of them have been considered in this work during the analysis. But some other factors, which we did not consider are:

1. Change in the amount of oxygen vacancies with respect to temperature,

2. Response and recover times of the sensor,

3. Effect of change in band gap due to different doping elements on the sensitivity,

4. Different surface species formed during and after the sensing processes.

Though this is not an exhaustive list, the study has been systematic in approaching the gas sensor behavior of pure and doped SnO_2 by considering maximum of the material parameters that would actually have an impact on its gas detection abilities. In this way, the best material from this material system, in this study is 1wt% Cu: SnO_2, bulk doped with urea as precipitation agent, was identified to be the best sample for the application chosen in this work. The broader impact of this research is that these principles can viably be applied to other MOS systems too, in order to engineer the nanomaterials to gas sensing applications.

The main idea of this work is to design a pellet based sensor, where having more material in nonmetric form cold deliver higher range of sensitivities in shorter time. However, like many sensing technologies, we also still have a big challenge for the design of the signal acquisition and conditioning circuits (read-out electronics, op amps, data converters, etc.). Therefore, the program's analog and mixed signal design experts work closely with the sensor developers, as well as with DSP and power experts from other programs. The goal is to combine sensor, actuators, and electronics onto a single chip by developing and integrating advanced processes.

We believe by achieving this challenge, it will bridge the worlds of academia and industry together. It features people with a wide range of expertise, from nanoscience, material science, quantum physics and chemistry to IC design and manufacturing processes.

APPENDIX

Future and scientific works, and calculations

APPENDIX A: FUTURE WORK

Some parts of the sensing mechanism could not be fully cleared up in this entire work. Therefore, still it is necessary for some further research to improve the knowledge about the metal oxide gas sensors and their basic working principles. Further experiments include the following:

- Primarily the response and recovery time measurements which are also the important parameters after sensitivity.
- Varying (higher and lower than 1wt %) the doping weight percentage for the doped pellets and observe the sensitivity.
- Also XPS analysis of the doped pellets, in order to confirm the form of dopant present in the SnO_2 matrix. This can reveal the difference between bulk and surface doping methods in more clear way.
- Preparing the pure and doped thick films by other deposition methods and verify their sensitivities.
- Designing of a pellet based SnO_2 sensor with the electrical interface in order to compare with the commercially available sensors.

APPENDIX B: PUBLICATIONS

PAPERS PUBLISHED

- Published a paper on "**Sensing properties of undoped and Pt-doped SnO2 Thin Films Deposited by Chemical Spray**" in Material science and semiconductor processing, SI: Functional semiconductors, May 2014.
- Published a paper on "**Sensors Based on Tin Oxide Pellets**" in Sensor Letters, Volume 12, Number 10, October 2014, pp. 1513-1518(6).
- Published a paper on "**Low-Temperature Synthesis and Gas Sensitivity of Perovskite-Type LaCoO3 Nanoparticles**" Journal of Nanomaterials Volume 2014 (2014), Article ID 164380, 8 pages.

CONFERENCE PUBLICATIONS

- Published a paper on "**Surface modified tin oxide pellets for CO Gas sensing**" in IEEE proceedings conducted on September 2014.
- Published a paper on "**Manufacturing of Tin Oxide Pellets and their application for CO and C_3H_8 Gas Sensors**" in IEEE proceedings conducted on September 2013.
- Published a paper on "**Synthesis and characterization of Tin oxide Powders by homogeneous precipitation**" in IEEE proceedings conducted on September 2012.

PAPERS UNDER COMMUNICATION

- A paper on "**Cu, Pt and Pd doped Tin Oxide as CO sensors**" communicated to journal "**Sensors and Actuators B chemical**".
- A paper on "**Pure and Cu doped SnO_2 Thick film gas sensors**" communicated to "**Sensors and Actuators B chemical**".
- A paper on "**Sputtered transparent ZnO thin films as Propane gas sensors**" communicated to journal "**Sensors and Actuators B chemical**".

APPENDIX C: CALCULATION PROCEDURE DETAILS

C.1. Undoped feed stock solution calculation

Formula

Molarity (M) = no. of moles/Volume (L)

No. of moles = Mass in grams/ Molecular Weight.

Mass of the Solute in grams = Molarity (M) * Volume of Solvent (L) * Molecular weight of the Solute.

Calculation

Solute: $SnCl_4.5H_2O$

Solvent: Ethanol

Concentration: 0.2M

Volume: 500ml (Assume)

Molecular Weight of Solute is:

Sn→ 118.71

Cl → 35.453

H→ 1

O→ 16

$SnCl_4.5H_2O$→ 118.71 + 4(35.453) + 5((2*1) + 16) → 350.522

Mass (g) = 0.2 * 500m * 350.522 = 35.0522.

Therefore **35.0522** grams of Solute ($SnCl_4.5H_2O$) is mixed with **500ml** of Solvent (Ethanol) to prepare the feed stock solution for precipitating tin oxide powders.

C.2. Doped feed stock solution calculation

Formula

If solution A with element X is mixed with solution B with element Y, then the wt% of X in Y is calculated as follows

Wt% of X/Y = (% of X in solution A) / [(%of X in solution A) + (%of Y in solution B)] * 100

Calculation

Pt doped

Solution A: $SnCl_4.5H_2O$

Solution B: $PtCl_2$

Molecular weight of Solution A is:

Sn→ 118.71, Cl → 35.453, H→ 1, O→ 16

$SnCl_4.5H_2O$→ 118.71 + 4(35.453) + 5((2*1) + 16) → 350.522

% of Sn in $SnCl_4.5H_2O$ → (118.71/350.522)*100→ 33.86

Molecular weight of Solution B is:

Pt→ 195.01, Cl → 35.453

$PtCl_2$→ 195.01+ 2(35.453) → 265.916

% of Pt in $PtCl_2$→ (195.01/265.916)*100→ 73.33

Wt% of Pt/Sn→ (73.33/ (73.33+33.86))*100→ 68.41

Therefore 68.41%of Pt is present compared to Sn. This calculation is for the mixed solution with a volume of 1L with a molarity 1M. In our work we have utilized 0.4M for 100ml of solution and for 1wt% of Pt. Therefore the quantity of $PtCl_2$in grams is given as

$PtCl_2$ (g) = $(1*0.4*100*10^{-3}*265.916)/68.41$ = 0.1554g

Therefore 0.1554g of $PtCl_2$ is added to the 0.4M $SnCl_4.5H_2O$ solution to get 1wt% of doping. Similar procedure is followed for Cu and Pd calculations too.

C.3. Schematic diagram of the Die utilized to manufacture the pellets

In this work all the pellets manufactured by utilizing a die. The die model has been designed by our group. It is designed in a way that it can sustain a pressure around 35tons. The material used for preparing the die is a hard steel D2. By using the D2 rods, the shape of the die has been cut and annealed at higher temperatures in order to avoid the expansion of the material during the pellet manufacturing. During the annealing process, the hard ness of the die can be set too. The die's top and base hardness were set to 54-56 kgf (Kilogram-force), piston hardness was set to 56-57 kgf. Finally the small pieces which goes inside the die and hold the material were also annealed and their hardness were set to 57-58 kgf.

The schematic diagram of the die with all its components is shown in Fig.C.1.

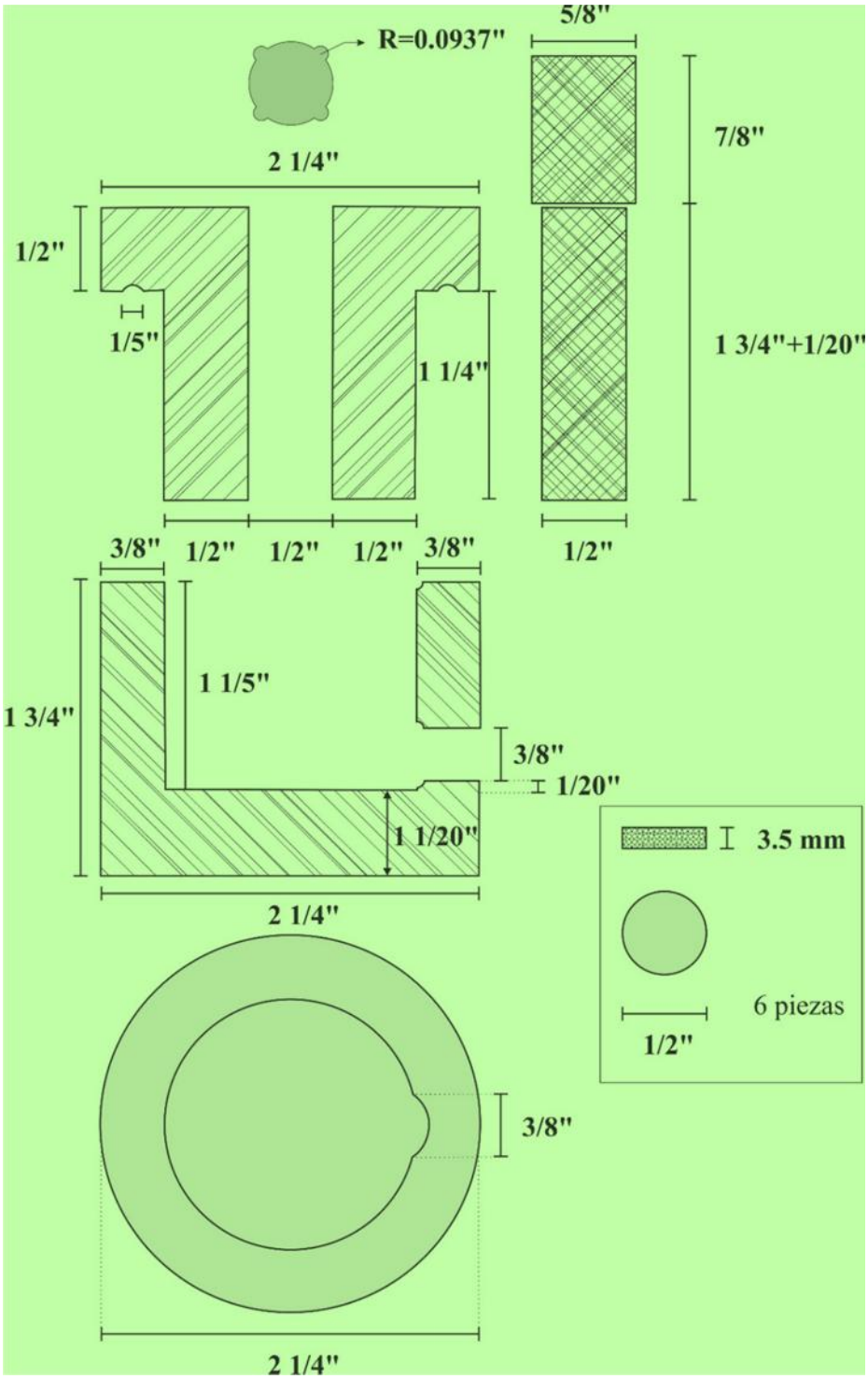

Fig. C.1. Schematic diagram of the die with all its components, utilized in our work for manufacturing the pellets.